# Functionalization of Carbon Nanotubes with Molecular Switches

Im Fachbereich Physik der
Freien Universität Berlin
eingereichte

Dissertation

von

Pascal Blümmel

Berlin, im Juli 2013

**1. Gutachter:** Prof. Dr. Stephanie Reich
**2. Gutachter:** Prof. Dr. Rainer Haag

Tag der Einreichung: 25. Juli 2013
Tag der Disputation: 20. September 2013

# Eidesstattliche Erklärung

Hiermit versichere ich, dass ich alle verwendeten Hilfsmittel und Hilfen angegeben und die vorliegende Arbeit auf dieser Grundlage selbstständig verfasst habe. Diese Arbeit ist nicht schon einmal in einem früheren Promotionsverfahren eingereicht worden.

Pascal Blümmel

# Zusammenfassung

In der vorliegenden Arbeit wurde die Funktionalisierung von Kohlenstoffnanoröhren mit molekularen Konformations- und Dipolschaltern untersucht. Ziel war es, die optoelektronischen Eigenschaften der Nanoröhren durch Änderung des Schaltzustands reversibel zu beeinflussen.

Mittels azobenzolbasierter Konformationsschalter konnte die Wasserlöslichkeit von Nanoröhren reversibel geschaltet werden. Über mehrere Schaltzyklen, bestehend aus UV-Bestrahlung, gefolgt von Bestrahlung mit sichtbarem Licht und anschließender milder Ultraschallbehandlung, war es möglich, die Formation und Auftrennung von Nanoröhrenbündeln in Wasser wiederholt zu schalten. Mit dieser Methode wäre es möglich, durch lokale Bestrahlung mit UV-Licht und die daraus resultierende Ablagerung von Nanoröhren, mikrometergroße Oberflächenstrukturen zu erzeugen.

Kohlenstoffnanoröhren wurden mittels Pyren-Spiropyran-Dipolschaltern unterschiedlicher Länge in THF gelöst. Da die Bindung zwischen Pyren und Nanoröhren nichtkovalent ist, blieben hierbei die eindimensionalen Quanteneigenschaften der Röhren erhalten. Die Variation des Abstands zwischen Nanoröhren und Spiropyran führte zu einer Rotverschiebung der $E_{22}$-Übergangsenergien von bis zu 14 meV - schon in der Spiropyran-Form. Des Weiteren führte ein geringerer Abstand zwischen Röhre und Schalter zu einer Stabilisierung der Merocyanin-Form. Aufgrund der Sensitivität der Schaltermoleküle gegenüber der Bestrahlung mit sichtbarem Licht war es nicht möglich, den Einfluss des Schaltzustands auf die optischen Eigenschaften der Röhren zu messen. Aufbauend auf den Ergebnissen der vorliegenden Arbeit wäre es allerdings möglich, Änderungen der elektronischen Eigenschaften z.B. durch Messung des elektronischen Transports zu ermitteln.

Um den theoretisch vorhergesagten Einfluss des Schaltzustands auf die Nanoröhren zu überprüfen, wurden Nanoröhren mittels SDS (Sodium Dodecyl Sulphate) in

Wasser gelöst. Spiropyran/Merocyanin (SP/MC) wurde anschließend mittels des sogenannten "Micelle Swelling" Verfahrens, bei dem Fremdstoffe in bestehende Mizellen eingeschleust werden, auf die Nanoröhrenoberfläche aufgebracht. In guter Übereinstimmung mit der Theorie wurden Peakverschiebungen von bis zu 13 meV zwischen mit SP und MC funktionalisierten Röhren ermittelt. Es wurde gezeigt, dass diese Verschiebung von der Anzahl der aufgebrachten Schalter abhängt und somit quasikontinuierlich verändert werden kann. Die durchschnittliche Lumineszenz MC funktionalisierter Nanoröhren ist gegenüber der lediglich mit SDS funktionalisierter Röhren stark verringert. Im Gegensatz dazu zeigen die SP funktionalisierten Röhren leicht erhöhte Lumineszenz. Eine mögliche Erklärung hierfür liefert die planare Geometrie des MC-Moleküls, welche Interaktionen zwischen den $\pi$-Orbitalen von Schaltern und Röhren ermöglicht. Nach der Adsorption wird auch das Schaltverhalten der SP- und MC-Isomere unterbunden. Die charakteristischen Absorptionsspektren von Merocyanin können auch in den mit SP funktionalisierten Proben gefunden werden. In den MC funktionalisierten Proben jedoch tritt ein weiteres Band auf, welches auf agglomeriertes MC hinweist (entweder MC-MC oder Röhre-MC). Weitere Forschung ist notwendig, um das genaue Verhalten beider Isomere (SP und MC) nach dem Einschleusen in die Mizellen zu verstehen.

# Summary

In this work, we investigated functionalization of carbon nanotubes using conformational and dipole switches as a way of altering the tubes' optoelectronic properties. Encapsulating nanotubes with the conformational azobenzene switches, we were able to achieve reversible precipitation of carbon nanotubes in water. Over several switching cycles, consisting of UV irradiation, followed by visible irradiation and sonication, we were able to reversibly induce the formation of nanotube bundles. This mechanism could be used to achieve light induced spatial directed deposition of carbon nanotubes as a way of preparing micro-size patterned surface structures. Pyrene-spiropyran derivatives with different separation lengths between anchor and dipole were used to non covalently disperse CNTs in THF while retaining the tubes' pristine 1D properties. The different tube-switch distance in both compounds was found to induce a red shift in the range of up to 14 meV in the $E_{22}$ transitions between the two samples, even in the SP form confirming theoretical expectations. At close distances, the MC form was found to be stabilized. However, as the switch is sensitive to light irradiation, PLE measurements investigating the influence of the switch state on the optical properties could not be conducted. As a natural prosecution of this work, transport measurements could be exploited to confirm the alteration of the nanotubes' electronic properties depending on the switch state. As the tubes are functionalized in solution, they can be readily drop cast onto a given substrate, contacted and measured.

To confirm the different influence of SP and MC on the nanotubes as theoretically predicted, nanotubes were solubilized in water using SDS. SP/MC was then adsorbed onto the tube surface, using micelle swelling. In good agreement with theory, peak shifts of up to 13 meV between SP and MC functionalized samples were found. This shift was shown to depend on the number of switches inserted into the micelles and is, thus, tunable in a continuous fashion. Further, the average luminescence per tube in the MC functionalized samples was significantly quenched, while in the SP functionalized it actually increased. A possible explanation for this is the planar geometry of the MC molecule giving rise to a large de-localized $\pi$-orbital able to interact with the nanotube $\pi$-orbitals. Upon adsorption SP and MC molecules are unable to undergo isomerization. However, the characteristic MC absorption bands can be observed even in the SP samples, while the MC compounds exhibit an additional peak attributed to stacked MC (either MC-MC or MC-tube stacked). To understand the exact behavior of both, SP and MC after infiltrating the micelles, further research is needed.

# Curriculum Vitae

Aus datenschutzrechtlichen Gründen wurde der Lebenslauf aus der elektronischen Version dieser Arbeit entfernt.

# Publikationsliste

## 2012

*1.* P. Bluemmel *et al.*, JPCM 24(39), 394005, *Tuning the Interaction Between Carbon Nanotubes and Dipole Switches: the Influence of the Change of the Nanotube-Spiropyran Distance*

*2.* P. Bluemmel *et al.*, Phys. Status Solidi B 249(12), 2479-2482, *Designing a Spiropyran-Based Molecular Switch for Carbon Nanotube Functionalization: Influence of Anchor Groups and Tube-Switch Separation*

*3.* A. Setaro *et al.*, Adv. Funct. Mater. 22(11), 2425-2431, *Non-Covalent Functionalization of Individual Nanotubes with Spiropyran-Based Molecular Switches*

*4.* C. Popeney *et al.*, ChemPhysChem 13(1), 203-211, *Polyglycerol-Derived Amphiphiles for the Solubilization of Single-Walled Carbon Nanotubes in Water: A Structure-Property Study*

*5.* C. Koerdel *et al.*, Nanoscale 4(10), 3029-3031, *Controlled Reversible Debundling of Single-Walled Carbon Nanotubes by Photo-Switchable Dendritic Surfactants*

*6.* E. Malic *et al.*, JPCM 24(39), 394006, *Carbon Nanotubes as Substrates for Molecular Spiropyran-Based Switches*

## 2011

*7.* P. Bluemmel *et al.*, Phys. Status Solidi B 248(11), 2532-2535, *Amphiphile Replacement on Carbon Nanotube Surfaces: Effect of Aromatic Groups on the Interaction Strength*

## 2010

*8.* P. Bluemmel *et al.*, Phys. Status Solidi B 247(11-12), 2891-2894, *Dispersion of Carbon Nanotubes Using an Azobenzene Derivative*

# Contents

# Motivation

Ever since their discovery in 1991 by Sumio Iijima [1], carbon nanotubes (CNTs) have given rise to a large field of investigations [2–7].

Often described as rolled up sheets of graphene, their diameters are in the nanometer range, while their lengths are typically in the range of $\mu$m [3]. Tube lengths of up to several cm have been reported [8]. Thus, nanotubes have a considerably large aspect ratio, making them ideal one dimensional crystals.

Carbon nanotubes exhibit remarkable physical properties. They are extremely stiff along their axis and show high flexibility perpendicular to it [9]. CNTs show excellent thermal conductivity even surpassing diamond and are able to endure high temperatures, remaining stable up to 4000°C [4]. Depending on the diameter and angle in which the graphene lattice is oriented relative to the tube axis (the chirality), nanotubes develop different properties, making them for example semiconducting or metallic. Thus, carbon nanotubes are not one, but a whole set of different materials with different electronic structure, conductance and optical properties [2].

A lot of effort has been directed at combining the outstanding properties of CNTs with other materials via functionalization. New high performance polymer compound materials were designed to for highly specialized applications [10–12]. Functionalization was used to solubilize and debundle CNTs [5, 13, 14]. Carbon nanotubes have been exploited as sensors for changes in their chemical environment, utilizing the tubes' sensitivity to changes in their dielectric environment [15, 16].

As carbon nanotubes constitute a whole set of different materials, it is of fundamental and technological interest to find ways for controlled and reversible tuning their optoelectronic properties. One way of gaining such a control mechanism is functionalization with optical molecular switches. Molecular switches are compounds possessing multiple (meta)stable configurations in the ground state. In photochromic switches, transition between these configurations is accessible via optical stimuli. Once adsorbed to the nanotube surface, depending on the switching state, the molecules will interact differently with the tube, thus, altering for example the conductivity or optical fingerprint.

In this work, we investigate two different kinds of molecular switches, azobenzene and spiropyran. Azobenzene is a conformational switch. Upon irradiation, the compound can be switched between a *trans* and a *cis* configuration, thus, inducing severe changes in its morphology. Spiropyran, on the other hand, is a dipole switch. Upon illumination, a transition from the colorless spiropyran (SP) form to the blue colored merocyanine (MC) form is observed. This isomerization leads to a charge separation and subsequently a change in the molecules electric dipole moment from $\mu$=7.5 D to $\mu$=13.6 D [17].

In literature carbon nanotube functionalization using both, azobenzene and spiropyran, have been reported. Guo *et al.* functionalized single walled carbon nanotube (SWCNT) field effect transistors (FETs) non covalently with spiropyran molecules [18]. They were able to continuously, reversibly shift the transistor's U-I characteristics upon UV illumination. Similarly, Simmons *et al.* non covalently attached azobenzene moieties to SWCNT FETs, allowing them to reversibly change the transistor's threshold voltage. Covalent nanotube functionalization with spiropyran located at different distances to the tubes was reported by the groups of Haddon and Giordani [19, 20]. The compounds were able to isomerize, however, luminescence of the tubes was destroyed in the process.

These functionalization schemes involved either single, deposited nanotubes, thus, allowing only for investigations of single devices and chiralities at a time, or involved covalently binding the switch to the tube, resulting in severe distortions of the tubes' electronic structure.

We developed a method of dealing with bulk amount of pristine nanotubes and isolate them in solution by homogeneously coating them with optical dipole switches. This method is non covalent, it preserves the tubes' pristine one dimensional quantum properties, as proven by the observed bright CNT IR emission, the first experimental report in literature for dipole-switches coated tubes. Thus, we have started to gain insight into the coupling mechanisms, trying to itemize them. Using conformational switches, we were able to reversibly de-bundle carbon nanotubes in solution upon optical stimulation. This allows for light driven deposition of carbon nanotubes, thus, easing their incorporation into, for example, nanoelectronic devices.

Switch molecules and CNT-switch complexes were characterized by optical absorption and luminescence measurements. Optical stimuli lead to isomerization of the molecules that can be monitored using absorption spectroscopy. Using photo luminescence the abundance of isolated semiconducting CNTs in a sample can be probed, as in nanotube bundles, luminescence is usually quenched by the presence of metallic species. Isolated single walled carbon nanotubes show distinct fluorescence peaks with positions positions depending on the interaction with their environment (i.e. solvent and adsorbates). Absorption measurements can be used to determine the total nanotube density, also taking into account bundles and metallic tubes.

This thesis, which is the result of a highly interdisciplinary work at the edge between physics, chemistry and material science, is organized as follows: In the **first chapter** of this thesis the structure of carbon nanotubes, as well as their electronic and optical properties will be introduced. The **second chapter** will give an overview over different methods of nanotube functionalization. In the **third chapter** I will describe the experimental setup used to obtain absorption and photo luminescence data. **Chapter four** focuses on amphiphilic design, probing several polyglycerol dendrons and their ability to efficiently disperse CNTs. Following this, **chapter five** describes our investigations of polyglycerol derived conformational azobenzene switches used for nanotube functionalization. In **chapter six**, dipole switch functionalization using spiropyran derivatives, non covalently bound via pyrene anchor groups will be investigated and in **chapter seven** we will show our results on the adsorption of spiropyran/merocyanine onto carbon nanotubes using the micelle swelling method. The last chapter gives a summary of our work and will provide an outlook to possible future research.

# 1 | Carbon Nanotubes

Carbon nanotubes are often described as rolled up sheets of graphene [2,3]. They are considered quasi one dimensional crystals or sometimes macromolecules. Carbon nanotubes can have a length ranging from a few micrometers up to centimeters. Their diameter is typically in the range of a few nanometers. For theoretical purposes, nanotubes are, thus, often considered infinitely long cylinders.

As a there are infinitely many ways to roll a sheet into a cylinder, this leads to a wide range of different nanotube structures and diameters. Nanotubs are distinguished by their diameter and chiral angle, the angle of the graphene helix around the tube. From these two characteristic values, the properties of a nanotube can be derived, for example whether a tube is semiconducting or metallic.

This chapter will give a basic introduction to the structure carbon nanotubes. It will be shown how to approximate the electronic band structure using a nearest neighbor tight-binding model of graphene (**section one**), followed by zone folding (**section two**). For a more thorough introduction see Refs. [2–4]. **Section three** will detail the nanotubes' optical properties.

Note in this thesis, unless specified otherwise, "carbon nanotubes" always refers to single walled carbon nanotubes (SWCNTs), consisting of exactly one graphene cylinder. In contrast, multiwalled carbon nanotubes (MWCNTs) consisting of multiple SWCNTs layered around one another.

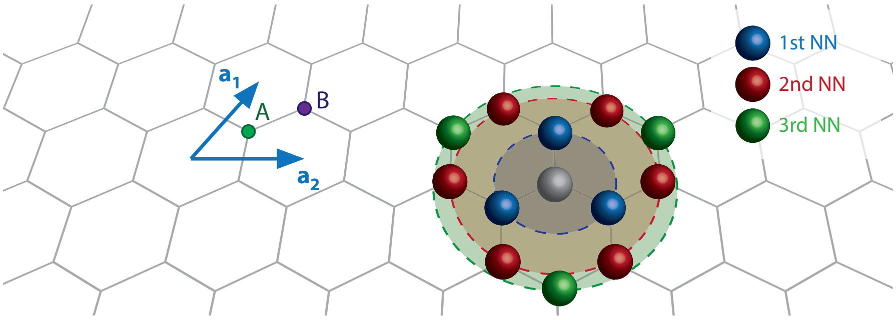

Figure 1.1. Sketch of the honeycomb structure of graphene, as well as the graphene unit vectors $\mathbf{a}_1$ and $\mathbf{a}_2$ (blue arrows). The two base atoms are labeled A (green) and B (purple). Further, for a given carbon atom (gray sphere), the first (blue spheres), second (red spheres) and third nearest neighbors (green spheres) are shown.

## 1.1. Graphene

### 1.1.1. Lattice and Unit Cell

Graphene is a quasi two dimensional carbon allotrope that, by itself, has drawn a tremendous amount of attention by the scientific community, culminating, for the time being, in the bestowal of the 2010 Nobel prize in physics to Andre Geim and Konstantin Novoselov "*for groundbreaking experiments regarding the two-dimensional material graphene*".

In this section, a theoretical description will be derived following Ref. [2].

Consisting of threefold coordinated carbon atoms arranged in a honeycomb structure with a lattice constant of $a_0 = 2.461\,\text{Å}$, graphene sheets can be considered monolayers of graphite. The graphene unit cell is described by a two atomic base, labeled A and B in Fig. 1.1, giving rise to two equal sub lattices. The translational unit vectors $\mathbf{a}_1$ and $\mathbf{a}_2$ have the length $a_0$, point from the center of one hexagon to the center of an adjacent one and and form an angle of 60°. The reciprocal lattice also has hexagonal structure and can be described by

$$\mathbf{k}_i \cdot \mathbf{a}_j = 2\pi\delta_{ij}, \tag{1.1}$$

where the $k_i$ are reciprocal lattice vectors and $\delta_{ij}$ is the Dirac delta function. The two lattice points within the graphene unit cell (occupied by an A and a B carbon atom) are located at $1/3(\mathbf{a}_1 + \mathbf{a}_2)$ and $2/3(\mathbf{a}_1 + \mathbf{a}_2)$, respectively.

### 1.1.2. Electronic Properties

A mathematical approach for ob obtaining the electronic band structure of carbon nanotubes consists of first deriving a tight binding approximation for the electronic bands of graphene. From there, the carbon nanotube bands can be calculated by the so called "zone folding" method, projecting the graphene band structure onto the nanotube Brillouin zone.

#### Tight Binding Approximation of Graphene

Within the tight binding description, the electrons in the system are considered strongly bound to their respective atomic cores and only weakly interacting with the neighboring atoms, similar to molecule orbital theory, used in chemistry.

Free carbon exhibits a $[He]2s^2 2p^2$ configuration and, thus, possesses four valence electrons. Within the hexagonal graphene sheet, they form planar $sp^2$ hybridized orbitals, linear superposition of the $2p_x$, $2p_y$, and $2s$ electrons. These orbitals overlap in-plane and form the so called $\sigma$-bonds of graphene. The remaining $p_z$ electrons (one per atom) are oriented perpendicularly to the graphene sheet. As the $sp^2$, and $p_z$ orbitals have no overlap, the $p_z$ orbitals can be treated independently. They form the so called $\pi$-bands.

Obtaining a description of the carbon nanotube $\pi$ bands, Schrödinger's equation has to be solved

$$\mathcal{H}\Psi(\mathbf{k}) = E(\mathbf{k})\Psi(\mathbf{k}). \tag{1.2}$$

Here $\mathcal{H}$ is the general Hamiltonian with the eigenvalues $E(\mathbf{k})$ and the eigenfunctions $\Psi(\mathbf{k})$, $\mathbf{k}$ is a wave vector. The eigenfunctions can now be written as a superposition of Bloch functions $\Phi_l(\mathbf{k})$

$$\Psi(\mathbf{k}) = \sum_l C_l \Phi_l(\mathbf{k}). \tag{1.3}$$

Using the tight-binding approximation, the Bloch functions of both sub lattices (A and B) can be expressed as a linear combination of the atomic wave functions:

$$\Psi_{A/B} = \frac{1}{\sqrt{N}} \sum_{\mathbf{R}_{A/B}} e^{i\mathbf{k}\mathbf{R}_{A/B}} \varphi(\mathbf{r} - \mathbf{R}_{A/B}). \tag{1.4}$$

The sum is taken over the whole graphene sheet. $\mathbf{R}_A$ is a lattice vector, $N$ the number of unit cells and $\varphi(\mathbf{r})$ are the normalized $2p_z$ orbitals of the isolated carbon. Inserting these eigenfunctions into Schrödinger's equation (Eq. (1.2)) yields

$$\begin{aligned} C_A[H_{AA}(\mathbf{k}) - E(\mathbf{k})S_{AA}(\mathbf{k})] + C_B[H_{AB}(\mathbf{k}) - E(\mathbf{k})S_{AB}(\mathbf{k})] &= 0 \\ C_A[H^*_{AB}(\mathbf{k}) - E(\mathbf{k})S^*_{AB}(\mathbf{k})] + C_B[H_{AA}(\mathbf{k}) - E(\mathbf{k})S_{AA}(\mathbf{k})] &= 0, \end{aligned} \tag{1.5}$$

with

$$S_{ij} = \langle \Phi_i \Phi_j \rangle = S^*_{ji}, \qquad H_{ij} = \langle \Phi_i | \mathcal{H} | \Phi_j \rangle = H^*_{ji}. \tag{1.6}$$

Here $S_{ij}$ is the overlap integral of the Bloch functions and $H_{ij}$ is the $ij$ matrix element of the Hamilton operator. Note that in Eq. (1.5) both carbon atoms in the base have been considered identical in assuming that $H_{BB} = H_{AA}$ and $S_{BB} = S_{AA}$. For $\det[H - ES] = 0$, Eg. (1.5) has non trivial solutions. Solving this determinant yields two bands denoted by $E(\mathbf{k})^+$ and $E(\mathbf{k})^-$, the eigenvalues of the antisymmetric conduction band ($E(\mathbf{k})^-$) and the symmetric valence band ($E(\mathbf{k})^+$):

$$E(\mathbf{k})^\pm = \frac{-(-2E_0 + E_1) \mp \sqrt{(-2E_0 + E_1)^2 - 4E_2E_3}}{2E_3}, \tag{1.7}$$

with

$$\begin{aligned} E_0 &= H_{AA}(\mathbf{k})S_{AA}(\mathbf{k}) \\ E_1 &= S_{AB}(\mathbf{k})H^*_{AB}(\mathbf{k}) + H_{AB}(\mathbf{k})S^*_{AB}(\mathbf{k}) \\ E_2 &= H^2_{AA}(\mathbf{k}) - |H_{AB}(\mathbf{k})|^2 \\ E_3 &= S^2_{AA}(\mathbf{k}) - |S_{AB}(\mathbf{k})|^2. \end{aligned} \tag{1.8}$$

Neglecting the overlap between wave functions located at different atoms yields a reasonably good approximation of the bands at the Γ-point. Thus, the overlap

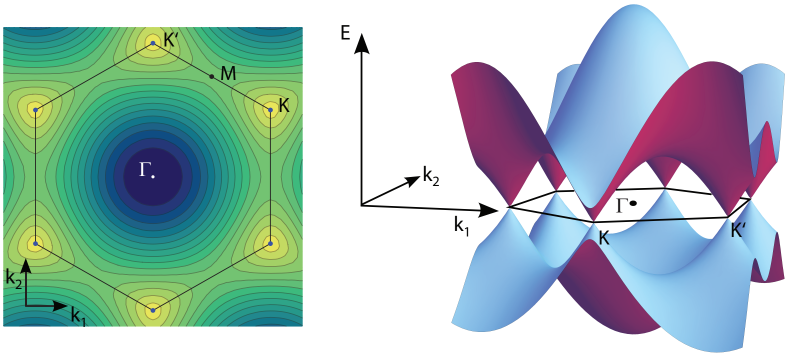

Figure 1.2. Band structure and Brillouin zone of graphene. The band structure was derived by a nearest-neighbor tight-binding approximation. left: Contour Plot of the $\pi$ band near the . right: 3d plot of the $\pi$ and $\pi^*$ bands. The linear band behavior at the K and K' points can clearly be observed.

integral $S_{ij}$ disappears for $i \neq j$ ($S_{AB} = \langle \Phi_A | \Phi_B \rangle = \delta_{AB}$). Equation (1.8) then becomes

$$\begin{aligned} E_0 &= H_{AA}(\mathbf{k}) \\ E_1 &= 0 \\ E_2 &= H_{AA}^2(\mathbf{k}) - |H_{AB}(\mathbf{k})|^2 \\ E_3 &= 1. \end{aligned} \tag{1.9}$$

With this Eq. (1.7) becomes

$$E_{S_{AB}=0}(\mathbf{k})^{\pm} = H_{AA}(\mathbf{k}) \mp |H_{AB}(\mathbf{k})|. \tag{1.10}$$

Considering only interactions between nearest neighbors, every carbon only sees its three adjacent neighboring atoms. Thus, $H_{AA}(\mathbf{k}) = H_{AA} = const.$ As a consequence of the $p$ orbital symmetry, the $\pi$ and $\pi^*$-band cross the K-point at the Fermi level. This and leads to

$$H_{AA} - |H_{AB}(K)| = H_{AA} + |H_{AB}(K)| = E_F = 0 \tag{1.11}$$

and

$$E^{nn}_{S_{AB}=0}(\mathbf{k})^{\pm} = \pm|H_{AB}(\mathbf{k})|. \tag{1.12}$$

This approximation, though a crude oversimplification, gives a sufficient description of the band structure close to the K-point where the $\pi$ and $\pi^*$ bands are almost linear (Dirac cones, see Fig. 1.2).

For a more general treatment, the matrix elements $H_{AB}$ and $S_{AB}$ in Eq. (1.7) have to be calculated from the Bloch functions. This yields

$$E^{\pm}(k_1, k_2) = \frac{(E_{2p_z} + E_{lattice}) \pm \gamma_0 \sqrt{f_{12}(k_1, k_2)}}{1 \pm \ s_0 \sqrt{f_{12}(k_1, k_2)}}. \tag{1.13}$$

Here $E_{2p_z}$ is the energy of the $2p_z$ orbital, $E_{lattice}$ is a contribution due to the crystal potential and $\gamma_0$ and $s_0$ are empirical parameters. Further, the remaining $f_{12}$ is

$$f_{12}(k_1, k_2) = 3 + 2[\cos(2\pi k_1) + \cos(2\pi k_1) + \cos(2\pi(k_1 - k_2))]. \tag{1.14}$$

At the K point ($K = 1/3(\mathbf{k}_1 - \mathbf{k}_2)$), $f_{12}$ vanishes resulting in a touching of the $E^+$ and $E^-$ bands (i.e. $E^{\pm}(k_1, k_2) = E_F$). As the overlap integral $s_0$ only takes values between 0 and 1 and the bonding state $E^+$ being of lower energy than the anti-bonding state $E^-$, $\gamma_0$ has to be negative.

The result of the tight binding calculation can be seen in Fig. 1.2, depicting the first valence and conduction bands of graphene.

## 1.2. Zone Folding

Carbon nanotubes are often described as rolled up sheets of graphene, the reason being that, like graphene, carbon nanotubes consist of $sp^2$ hybridized carbon atoms arranged in a hexagonal structure. Thus, using the base and unit vectors of the graphene lattice, the nanotube unit cell can be constructed. Figure 1.3 shows the unit cell of a nanotube mapped onto a graphene layer (gray area). The nanotube is created by rolling up the graphene sheet along the red arrow labeled **c** (the circumferential vector), connecting both ends of it. As can be seen in Fig. 1.3, **c** can be expressed as a linear combination of $\mathbf{a}_1$ and $\mathbf{a}_2$. Similarly, perpendicular to **c**, a vector **a** denoting the smallest graphene lattice vector along the tube axis can

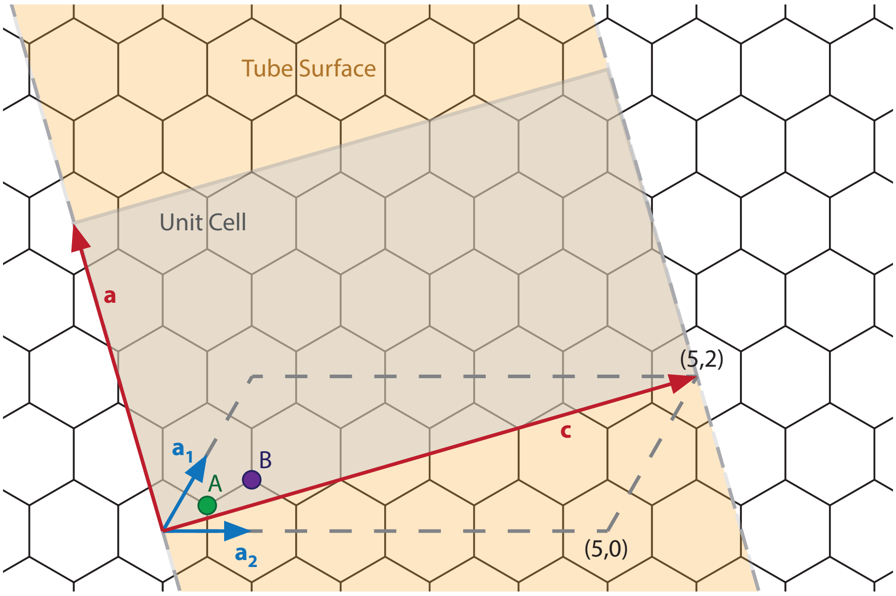

Figure 1.3. Sketch of the honeycomb structure of graphene, as well as the graphene unit vectors $\mathbf{a}_1$ and $\mathbf{a}_2$ (blue arrows). The two base atoms are labeled A (green) and B (purple). Also shown is the unit cell of a chiral (5,2) tube (gray shaded area), as well as the smallest vector along the tube axis $\mathbf{a}$ and the circumferential vector $\mathbf{c}$ (red vectors). The orange shaded area denotes the part of the sheet used to roll up the (5,2) tube.

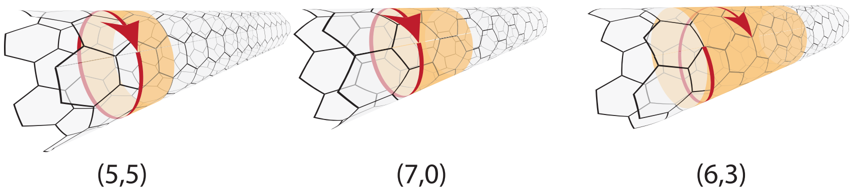

Figure 1.4. Structure of achiral (5,5) armchair and (7,0) zigzag tubes, as well as a chiral (6,3) tube. The red vectors demonstrate the chirality, running along either the armchair or the zigzag edge.

be defined (red arrow in Fig. 1.3). $\mathbf{c}$ and $\mathbf{a}$ can be expressed through the graphene unit vectors:

$$\mathbf{c} = n_1\mathbf{a}_1 + n_2\mathbf{a}_2 \tag{1.15}$$

$$\mathbf{a} = -\frac{2n_2 + n_1}{n\mathcal{R}}\mathbf{a}_1 + \frac{2n_1 + n_2}{n\mathcal{R}}\mathbf{a}_2. \tag{1.16}$$

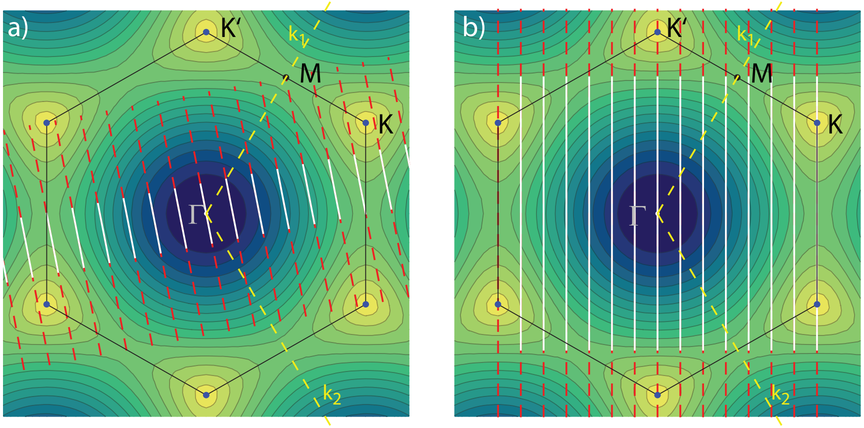

Figure 1.5. Brillouin zones of a (8,4) (a) and a (7,7) (b) carbon nanotube (white lines) plotted over the Brillouin zone and band structure of graphene. The dotted yellow lines denote the reciprocal lattice vectors and the red dashed lines are the allowed $k$ vectors along the tube axis.

Here, $n$ denotes the greatest common divisor of $n_1$ and $n_2$ while $\mathcal{R}$=3 if $(n_1-n_2)/3n$ is an integer and $\mathcal{R}$=1 if not. A carbon nanotube can be uniquely identified by its circumferential vector or ($n_1$,$n_2$) values, often also referred to as the tube's "chirality". The tube in Fig. 1.3, thus, is called a (5,2) tube. Depending on the chirality, two different kinds of tubes are distinguished. Armchair and zigzag tubes (see Fig. 1.4, left and middle) are rolled up along a high symmetry direction (0° and 30°) and are called achiral tubes. Chiral tubes, on the other hand can be rolled up any other angle (see Fig. 1.4, right). A carbon nanotube unit cell is composed of

$$q = \frac{A_{CNT}}{A_{graphene}} = \frac{n_1^2 + n_1 n_2 + n_2^2}{n\mathcal{R}} = \frac{2N}{n\mathcal{R}} \tag{1.17}$$

graphene unit cells and, thus, contains $2q$ lattice points. $A_{graphene}$ and $A_{CNT}$ denote the areas of the graphene and nanotube unit cell, respectively and $N = \sqrt{n_1^2 + 2n_1 n_2 + n_2^2}$. Along the axis, the tube can be considered infinitely long. Thus, the allowed electronic wave vector $k_{\|}$ is continuous. Corresponding to the translational period it has a length of $k_{\|} = 2\pi/|\mathbf{a}|$. However, in contrast to the infinite graphene sheet discussed before, the electrons in the carbon nanotube $\pi$ orbitals underlie periodic boundary conditions due to the finite circumference causing quantization of the waves perpendicular to the axis:

$$k_{\perp} = \frac{2\pi}{\lambda} = \frac{2\pi}{|c|}m = \frac{2}{d}m, \tag{1.18}$$

$m$ being an integer ranging from $-\frac{q}{2}+1, ..., 0, 1, ..., \frac{q}{2}$, while $d$ is the tube diameter and $\lambda$ is the wavelength. The first Brillouin zone of carbon nanotubes, thus, consists of $q$ lines parallel to the tube axis, separated by $k_{\perp} = 2/d$. Allowed vectors are in the range of $]-\pi/a, \pi/a]$. The projections of $k_{\perp}$ and $k_{\|}$ onto the tube axis ($\mathbf{a}$) and circumference ($\mathbf{c}$), yields

$$\mathbf{k}_{\perp} \cdot \mathbf{c} = 2\pi, \quad \mathbf{k}_{\perp} \cdot \mathbf{a} = \mathbf{k}_{\|} \cdot \mathbf{c} = 0 \quad \text{and} \quad \mathbf{k}_{\|} \cdot \mathbf{a} = 2\pi. \tag{1.19}$$

Thus, $k_{\perp}$ and $k_{\|}$ can be expressed as in terms of the reciprocal lattice vectors $k_1$ and $k_2$

$$\begin{aligned} \mathbf{k}_{\perp} &= \frac{2n_1+n_2}{qn\mathcal{R}}\mathbf{k}_1 + \frac{2n_2+n_1}{qn\mathcal{R}}\mathbf{k}_2 \\ \mathbf{k}_{\|} &= -\frac{n_2}{q}\mathbf{k}_{+}\frac{n_1}{q}\mathbf{k}_2. \end{aligned} \tag{1.20}$$

Figure 1.5 depicts Brillouin zones of an (8,4) and a (7,7) nanotube exemplarily (white lines). The dashed red lines are the allowed $k$ vectors along the tube axis. As can be seen, in the case of the (7,7) tube, an allowed $k$ vector contains the K point and, thus, the band crossing making the tube metallic. In the (8,4) tube, the K point is not covered by any allowed $k$ vectors and consequently the tube is semi conducting.

The high quality of this relatively simple approach becomes obvious in Fig. 1.6. Comparing a third nearest neighbor (3rd NN) tight binding model (a) with a band structure derived by a 1st NN tight binding approach (b) and ab initio calculations (c). As can be seen, even the band structures predicted by the 1st NN model achieves qualitatively good results. The 3rd NN model gives almost identical results to the first principle calculations.

Considering $i$ one-dimensional electronic bands, the density of states (DOS) $n(E)$

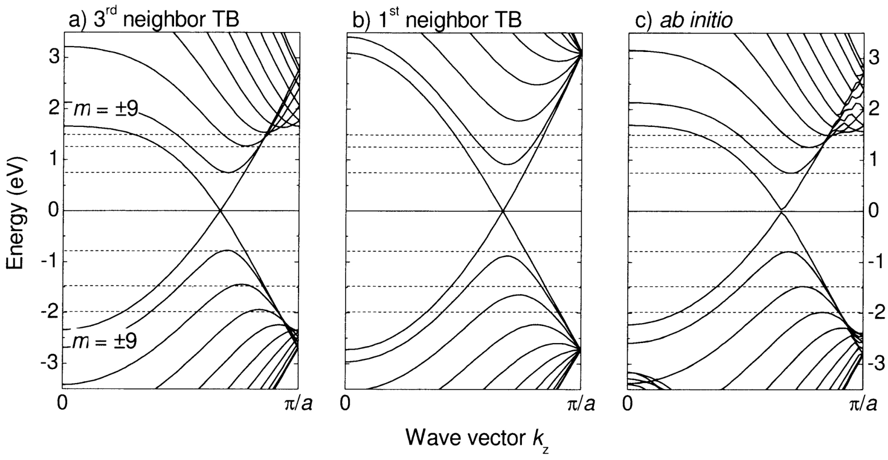

Figure 1.6. Band structure of a (10,10) nanotube derived using (a) zone-folding factoring in the third-nearest-neighbors tight-binding model, (b) zone-folding within the nearest-neighbor tight-binding approximation and (c) ab initio calculations. The dashed lines mark the energies with vanishing slope. (Taken from Ref. [2] ).

is given by

$$n(E) = \frac{2}{A_{BZ}} \sum_i \int dk_z \delta(k_z - k_i) \left| \frac{\delta E^{\pm}(k_\perp, k_z)}{\delta k_z} \right|^{-1} \tag{1.21}$$

(from Ref. [21]). The total area of the CNT Brillouin zone is denoted $A_{BZ} = q|k_z| = 4\pi^2 d/\sqrt[3]{a_0}^{2}$ and the $k_i$ are given by $E - E^{\pm}(k_\perp, k_z)$. Assuming linear bands near the K-point $n(E)$ can be derived to:

$$n(E) = \frac{4a_0}{\pi^2 d\gamma_0} \sum_{m=-\infty}^{\infty} \begin{cases} \frac{|E|}{\sqrt{E^2 - E_m^2}} & |E| > |E_m| \\ 0 & |E| < |E_m| \end{cases} . \tag{1.22}$$

This expression diverges at $E = E_m$, the so called *van-Hove* singularities. This relation is the result of a nearest-neighbor tight-binding approximation and only depends on the tube diameter. However, Fig. 1.7 reveals that Eq. (1.22) is in good agreement with first-principle calculations.

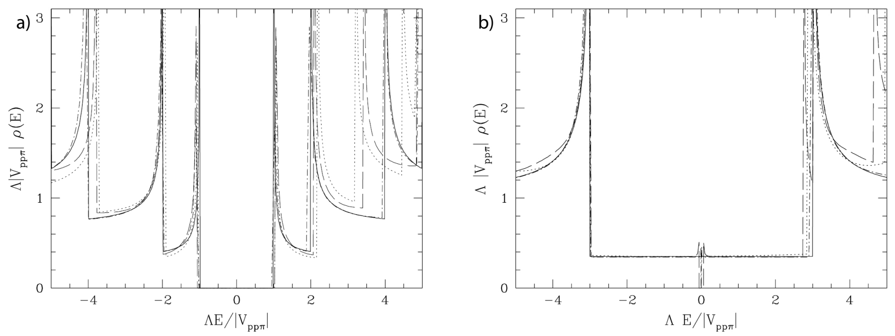

Figure 1.7. Electronic density of states calculated from Eq. (1.22) and from ab-initio calculations. (a) shows the electronic DOS for a (16,10) (dotted line), a (13,6) (dashed line) and a (21,20) (dot-dashed line) nanotube, derived from ab-initio calculations. The universal relationship for semiconducting nanotubes (solid line) has been calculated using Eq. (1.21). (b) depicts the result for metallic tubes (solid line) and ab-initio calculations for a (10,10) (dotted), (14,5) (dashed) and (22,19) (dot-dashed) SWNT. (Taken from Ref. [21])

## 1.3. Optical Properties of Carbon Nanotubes

### 1.3.1. Optical Absorption

The dielectric response of a solid-state system to a photon of frequency $\omega$ can be described using the complex dielectric function $\epsilon(\omega)$. It connects the dielectric displacement $\mathbf{D}(\omega)$ to the external electric field $\mathbf{E}(\omega)$:

$$\mathbf{D}(\omega) = \epsilon(\omega)\mathbf{E}(\omega) = \left[\epsilon_{re}(\omega) + i\epsilon_{im}(\omega)\right]\mathbf{E}(\omega). \tag{1.23}$$

Here $\epsilon_{re}$ and $\epsilon_{im}$ are the real and imaginary parts of the dielectric function, respectively. The absorption of a sample can be expressed in terms of the imaginary part $\epsilon_{im}$ by

$$\alpha = \frac{2\kappa\omega}{c} = \frac{\epsilon_{im}\omega}{\eta c}, \tag{1.24}$$

with the speed of light $c$ and the $\eta$ and $\kappa$ as the real and imaginary parts of the index of refraction, respectively. $\eta$ varies slowly and is, thus, approximated as constant. Within the dipole approximation, $\epsilon_{im}$ can be written as

$$\epsilon_{im}(\omega) = \left(\frac{2\pi e}{m\omega}\right)^2 \sum_{c,v}\sum_{k} |P_{vc}|^2 \delta(\Delta E_{cv} - \hbar\omega) = \left(\frac{2\pi e}{m\omega}\right)^2 |P_{vc}|^2 n_j(E), \qquad (1.25)$$

with the dipole matrix element $P_{vc}$ assumed to be constant. $\Delta E_{cv} = E_c(\mathbf{k}) - E_v(\mathbf{k})$ is the energy gap between valence and conduction bands and $n_j(E)$ is the joint density of states (JDOS)

$$n_j(E) = \int \frac{dS_{\mathbf{k}}}{\nabla_{\mathbf{k}}(\Delta E_{cv}(\mathbf{k}))}. \qquad (1.26)$$

Here $S_{\mathbf{k}}$ is the constant energy surface ($\Delta E_{cv} = const$). The optical absorption is, thus, dominated by regions in the band structure $\nabla \Delta E_{cv} = 0$, i.e. parallel bands.

### 1.3.2. Optical Selection Rules

Due to their symmetry, carbon nanotubes give rise to certain selection rules. Due to conservation of momentum, only vertical transitions ($\Delta k \approx 0$) between valence and conduction bands are optically allowed. Further, the selection rules are dependent on the polarization of the electric field vector relative to the tube axis. To conserve total angular momentum upon photon absorption, the following selection rules must be fulfilled:

$$\begin{aligned} \Delta m &= 0 \quad \text{for} \quad \mathbf{E}||z, \\ \Delta m &= \pm 1 \quad \text{for} \quad \mathbf{E} \perp z. \end{aligned} \qquad (1.27)$$

Here $z$ is the direction of the tube axis and $m$ is the $z$ component of the angular momentum. While $z$-polarized photons, inducing transitions between bands with the same $m$ are always allowed, transitions polarized in the $xy$-plane are usually restricted to the two bands closest to the Fermi level.

Absorption of light polarized perpendicularly to the tube axes is suppressed in carbon nanotubes. While parallel external field will not induce a polarization $\mathbf{P}$ in an infinitely long cylinder and, thus, $\mathbf{E}_{||}$ matches the applied external field, a field perpendicular to the cylinder axis induces a charge redistribution on the tube sidewalls. This polarization opposes the external field thus reducing $\mathbf{E}_\perp$. This so-called antenna or depolarization effect is diameter dependent and the screening increases for smaller diameters.

### 1.3.3. Photo Luminescence of Carbon Nanotubes

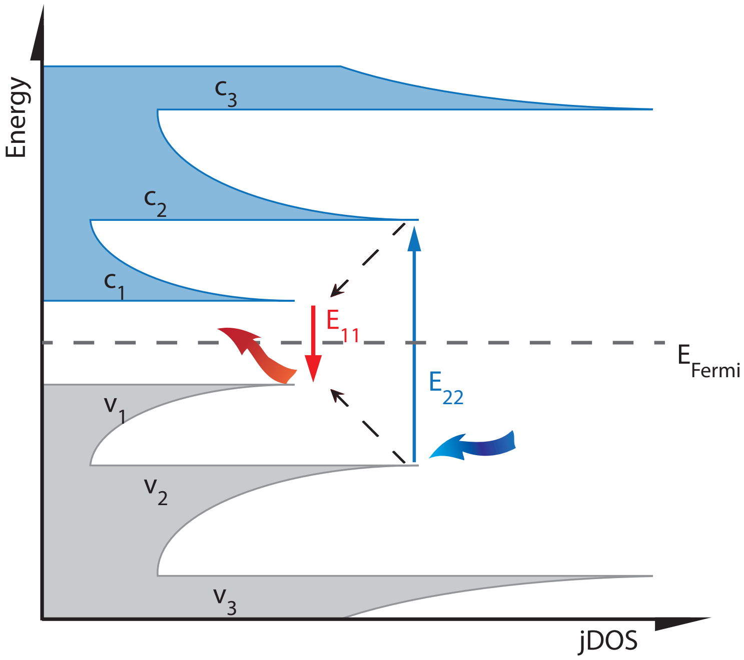

Figure 1.8. Schematic absorption and fluorescence in a semiconducting carbon nanotube . Absorption is allowed between bands of the same index. An absorption $v_x \rightarrow c_x$ is denoted $E_{xx}$. After internal conversion, $E_{11}$ fluorescence is observed. Here, a photon of energy $\mathrm{E}_{22}$ is absorbed (blue, curved arrow) and excites an electron (blue arrow). Electron and hole then relax non radiatively to the ground state (dashed arrows), recombine (red arrow) emitting a photon of energy $\mathrm{E}_{11}$ (red curved arrow).

In the single particle picture, optical transitions in carbon nanotubes occur mainly between the van-hove singularities in the JDOS. Carbon nanotubes, thus, exhibit sharp absorption features. However, in a nanotube ensemble containing many different nanotubes, it is often not possible to resolve individual chiralities, as they can have very similar transition energies. Photo luminescence Excitation (PLE) experiments can be used to separate the signal originating from different

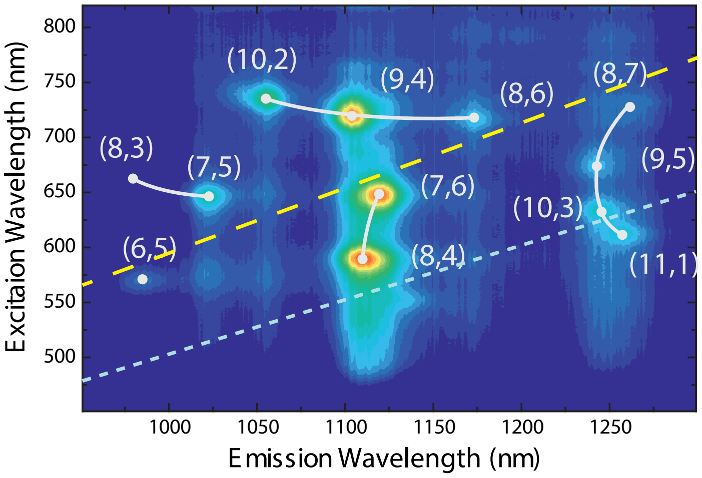

Figure 1.9. PLE map for carbon nanotubes covered with SDS in water. After absorption at $E_{22}$, $E_{11}$ luminescence is observed. The chiral index assignment was done by comparison with Ref. [13]. The gray curves connect tubes of the same (2n+m) values and the gray dashed line marks $\mathrm{E}_{ex}/\mathrm{E}_{em} = 2$, while the yellow dashed line marks $\mathrm{E}_{ex}/\mathrm{E}_{em} \approx 1.7$.

tube chiralities. The nanotube luminescence is measured as a function of the excitation energy. Figure 1.8 illustrated the involved processes. First, absorption occurs at energy $E_{22}$ (blue arrows). Then, radiation free internal conversion leads to relaxation into the lowest band (dashed arrows), followed by fluorescent recombination over the $E_{11}$ band gap (red arrow).

Figure 1.9 shows a PLE map of carbon nanotubes with excitation light provided in the visible ($\mathrm{E}_{22}$) and emitted light detected in the infrared region ($\mathrm{E}_{11}$). The map shows a pattern of distinct peaks, uniquely identifying the different chiralities (in principle probing the JDOS). At the gray dashed line, the excitation energy is twice the emission energy ($\mathrm{E}_{ex}$=2$\mathrm{E}_{em}$). From the single particle picture, the $\mathrm{E}_{22}/\mathrm{E}_{11}$ ratio is is expected to be 2 for large diameter tubes. However, it is found that this is not the case. This phenomenon is called the "Ratio Problem". Figure 1.8 also shows a relaxation in the valence band from $v_2$ to $v_1$ (lower dashed black arrow). This denotes the hole, left behind by the excited electron relaxing into $v_1$. In contrast to the relatively simple single particle picture, optical transitions in carbon nanotubes are dominated by excitonic effects, even at room temperature.

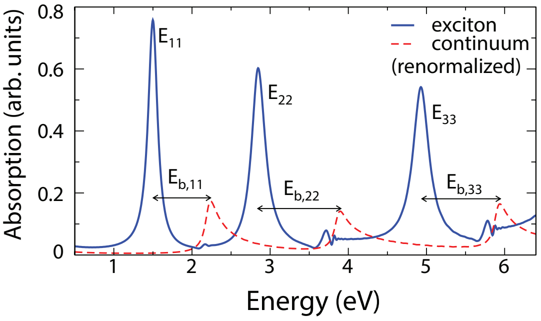

Figure 1.10. Change of the absorption spectra of a (10,0) zigzag nanotube when moving from a single particle description, including electron electron interactions (red, dashed line) to a picture including excitonic effects (blue, solid line). The relatively large shifts of the $E_{ii}$ transition energies between the two theories correspond to the excitonic binding energy $E_{b,ii}$ and are in the order of 1 eV. As can be seen, the binding energy increases for higher transitions (larger $i$). Adapted from Ref. [22].

## 1.3.4. Excitons in Carbon Nanotubes

While the single particle picture gives good approximations for large diameter tubes, curvature effects in narrow SWNTs (≈1 nm [23]) lead to an overlap between the $\sigma$ and $\pi$ bands and, thus, the tight binding approximation becomes less reliable. This, together with the ratio problem shows the necessity of taking into account excitonic effects brought about by, for example, the coulombic attraction between electron and hole, as well as the electron-electron repulsion. As excitons in carbon nanotubes exhibit remarkably strong binding energies in the range of 1 eV, excitonic effects strongly influence the nanotubes' optoelectronic properties even at room temperature [2, 23].

Upon excitation of an electron from a valence to a conduction band, a hole in the valence band is left behind, acting like a positively charged particle. Electron and hole attract via Coulomb interaction, forming an exciton. The electrons left in the valence band, on the other hand, act repulsive on the excited electron. These excitonic effects lead to a distortion of the bands, thus, affecting the $E_{ii}$ transition energies and responsible for the ratio problem. Figure 1.10 illustrates the difference between the single particle and the excitonic picture comparing the theoretical absorption spectra of a (10,0) tube.

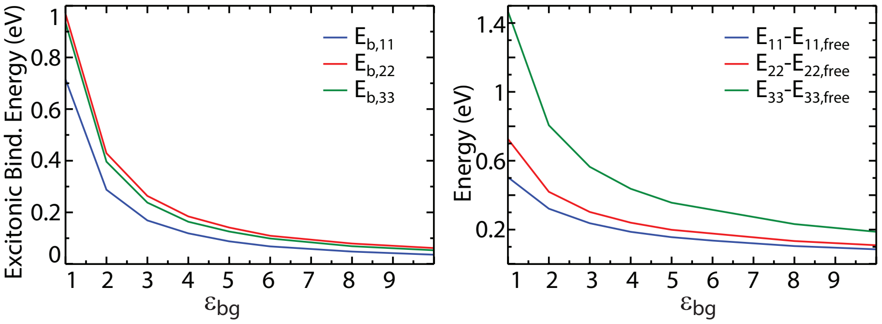

Figure 1.11. Dependence of the excitonic binding energies (left), as well as the transition energies compared to the free particle energies (right) on the dielectric environment constant. As can be seen, for large $\epsilon_{bg}$, the exciton binding energies become strongly suppressed excitonic effects become less pronounced. Looking at the total transition energies, it can be seen that for large dielectric backgrounds, the transition energies approach those from the single particle picture. (Adapted from Ref. [22]).

The Coulomb interaction leads to a localization of the excitonic wave functions in real space. Thus, $\mathbf{k}_c$ and $\mathbf{k}_v$ (the wave vectors for the valence and conduction bands, respectively) are no longer good quantum numbers. The Hamilton operator for the mixed system is written as:

$$H = E^*_{\mathbf{k_c}} - E^*_{\mathbf{k_v}} + V_{eh,Coulomb} + W_{eh,Exchange} \tag{1.28}$$

[23]. Here, the $E^*_{\mathbf{x}}$ are defined as

$$E^*_{\mathbf{x}} = E_{\mathbf{x}} - E_{self}, \tag{1.29}$$

$E_{\mathbf{x}}$ is energy from the single particle picture, while $E_{self}$ is the self energy caused by a Coulomb exchange interaction between particle and field. The other parameters in in Eq. (1.28) represent electron-hole interactions, namely the direct Coulomb interaction (V) and the exchange interaction (W). The direct Coulomb interaction is screened by the valence electrons as well as a potentially surrounding medium. Miyauchi *et al.* [24] approximated V as

$$V_{eh} = \frac{\nu_{eh}}{\epsilon_{bg}} = \frac{\nu_{eh}}{\kappa\ \rho(\mathbf{k_c} - \mathbf{k_v})}, \qquad \frac{1}{\kappa} = \frac{C_{tube}}{\kappa_{tube}} - \frac{C_{env}}{\kappa_{env}}. \tag{1.30}$$

The parameters $C_{tube}$ and $C_{env}$ are coefficients for the inside and outside of the nanotube, respectively, depending on the tube's diameter and chiral angle. $\kappa_{tube}$ is the dielectric constant inside the tube, excluding the $\pi$-orbitals and $\kappa_{env}$ is the dielectric constant of the tube environment. $\rho$ is the dielectric function describing effects of the $\pi$ band polarization.

Taking into account screening of the carrier-carrier interactions by an external (environmental) electric potential, Malic *et al.* [22] found a simple scaling law for the exciton binding energies as a function of $\epsilon_{bg}$:

$$E_{b,ii} \propto \; A_{i,d}\epsilon_{bg}^{-1.3}. \tag{1.31}$$

Here, the factor A depends on the transition $E_{ii}$, as well as the tube diameter. From this it can be understood that environments with large dielectric constants lead to a strong suppression of the exciton binding energies. This is illustrated in the left part of Fig. 1.11. The overall changes in the transition energies are expressed as:

$$\Delta E_{b,ii} \propto \; B_{i,d}e^{-\beta_1 \epsilon_{bg}} + C_{i,d}\epsilon_{bg}^{-\beta_2}, \tag{1.32}$$

with $\beta_1 \approx 0.2$ and $\beta_2 \approx 0.8$. This relation is shown in the right part of Fig. 1.11. For large dielectric background constants, the transition energies approach those of the single particle picture and excitonic effects become less important. However, the fact that the transition energies in general depend on the dielectric environment can be exploited as a way of tuning CNTs by altering their environment.

In later works [25, 26], Malic *et al.* extended this picture and added a coupling interaction between the excitons within the tubes and external dipole moments. This coupling was found to depend on the dipole orientation compared to the tube axis, as well the distance and, of course magnitude and coverage. For a (10,10) a red shift of the $E_{11}$ transition of up to 40 meV has been predicted for MC functionalized tubes, compared to SP, providing optimal coupling geometry. Thus, dipole switch functionalization, could provide a valuable tool for tailoring the optoelectronic properties of carbon nanotubes.

# 2 | Functionalization of Carbon Nanotubes

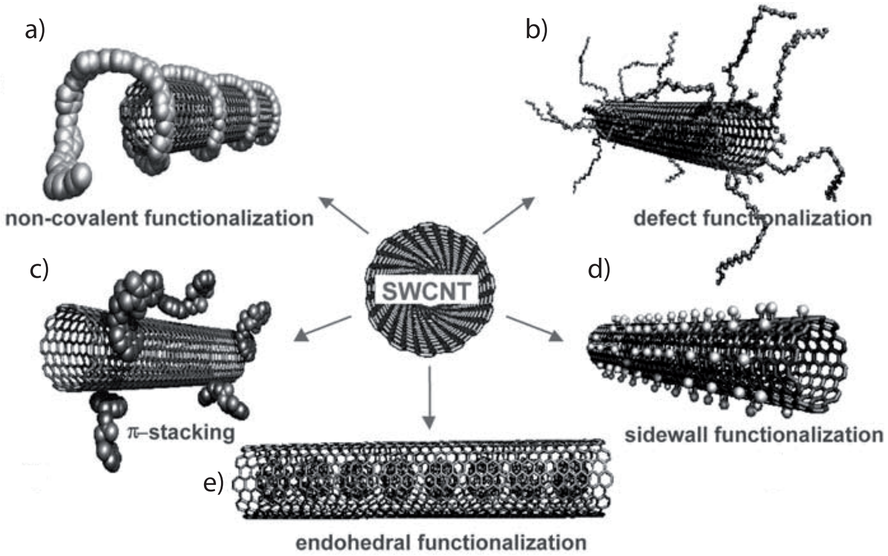

Figure 2.1. Functionalization of carbon nanotubes has been achieved using different approaches. There are non covalent ways to attach molecules to the surface of carbon nanotubes like wrapping them in polymers (a), through $\pi$-$\pi$ stacking interactions (c) or by endohedral filling (e), as well as more radical ways of covalent functionalization of defects (b) or direct sidewall functionalization (d). (Taken from Ref. [27])

Due to their extended $\pi$-network, perfect SWCNTs can be considered aromatic macro molecules. As produced SWCNTs tend to aggregate via van-der-Waals interaction and form bundles, subsequently distorting their optoelectronic properties and quenching photo luminescence, as the presence of metallic nanotubes inside the aggregates opens up non radiative de-excitation pathways. Functionalization has been widely exploited as a way of lowering the strong tube-tube van-der-Waals attraction, thus separating carbon nanotubes and, for example, restoring the pristine tubes' optical and electronic properties [13, 28]. Further, functionalization has been used to improve nanotube solubility [5,13,28], change the tubes' properties [18, 29–31] or endow nanotubes with new functionalities [5, 6, 32, 33].

Figure 2.1 shows different ways of nanotube functionalization. These approaches can be split into two major groups: covalent and non covalent. Covalent approaches like defect or sidewall functionalization (Fig. 2.1 (b) and (d), respectively), rely on chemically bonding functional groups to the tube surface. Non covalent approaches through polymer wrapping, physisorption or endohedral filling (Fig. 2.1 (a), (c) and (e), respectively), attach functional groups physically, through comparatively weak forces like van-der-Waals interactions or $\pi$-$\pi$ stacking.

In the following section different ways of covalent and non covalent nanotube functionalization will be explained, motivating why for the work at hand, non covalent approaches were chosen.

## 2.1. Covalent Functionalization of Carbon Nanotubes

Perfect SWCNTs are hardly chemically reactive. However, their finite radius induces two effects that cause local strain making the tube more susceptible to addition reactions. The surface curvature leads to pyramidalization of conjugated carbon atoms. As the nanotube surface is curved, adjacent carbon atoms are not located within the same plane. Thus, the $\pi$ and $\sigma$-orbitals are not fully perpendicular to each other, but oriented at an angle $\theta_{\sigma\pi}$, the so called pyramidalization angle. This causes a deformation of the $\pi$-orbitals increasing the electron density outside of the tube, making it more reactive [34](see Fig. 2.2a). Simultaneously, the inner part of the tube becomes even more inert.

A similar effect is caused by a misalignment of adjacent $\pi$-orbitals (see Fig. 2.2b). Niyogi *et al.* even believe the $\pi$-orbitals misalignment to be the main reason for strain in carbon nanotubes [35]. As both effects scale with the surface curvature, chemical reactivity of carbon nanotubes strongly depends on the tube's diameter.

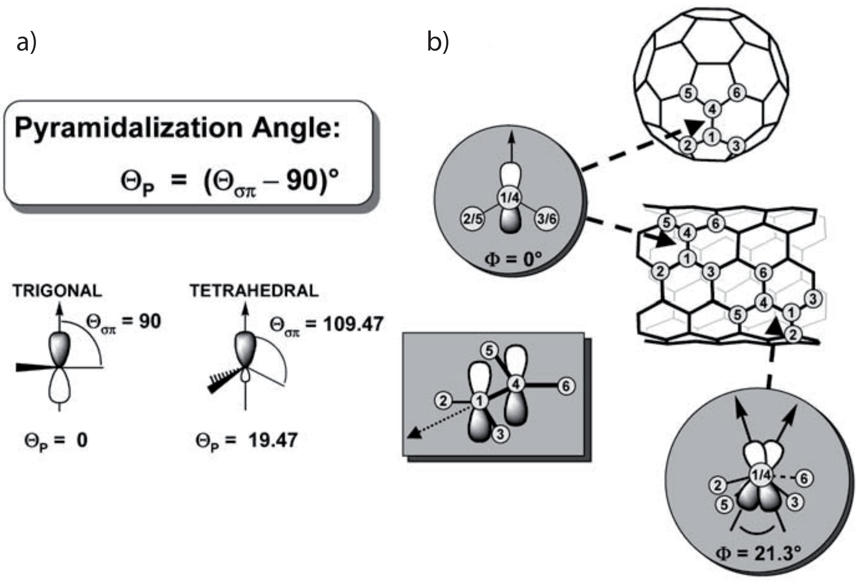

Figure 2.2. Curvature induced pyramidalization. To the curvature of the nanotube surface leads to to the $\sigma$-orbital not being planar as for example in graphene. The angle of pyramidalization is defined by the angle between the $\sigma$ and $\pi$-orbitals ($\theta_{\sigma\pi}$) is illustrated in (a). The misalignment of the $\pi$-orbital along the C1-C4 bond for a (5,5) tube and $C_{60}$ is shown in (b). (Taken from Ref. [5])

Defect functionalization, as the name suggests, utilizes defects in the nanotube structure to chemically bind functional moieties to the tube surface. To this end, either pre existing defects (for example from the preparation method) can be exploited or using invasive treatments, new defects can be induced. Oxidation treatments utilizing various acids like nitric acid and sulfuric acid or piranha (sulfuric acid-hydrogen peroxide), open up the nanotube caps, induce defects in the tubes' sidewalls, attaching carboxyl groups [5, 36–38]. The attached carboxyl groups can then replaced by the desired functionalities. Further defect inducing methods involve fluorination and hydrogenation, however, inducing even stronger distortions of the $\pi$ bands than reported for oxidative treatment (see [5, 27] and references therein).

Direct covalent sidewall functionalization changes the carbon hybridization from $sp^2$ to $sp^3$ and, thus, results in a loss of conjugation. Cycloadditions with, for example, nitride and carbene have been investigated by Holzinger *et al.* [39].

These methods allow for stable nanotube functionalization, offering ways to separate

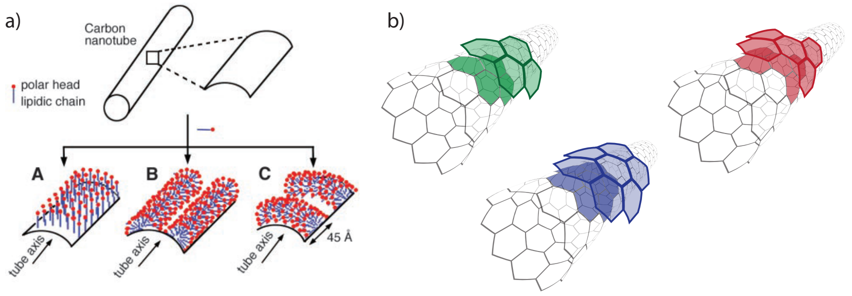

Figure 2.3. a) Possible micellar structures built around a carbon nanotube. The amphiphiles can either form one micelle (A) or many small hemi micelles (B, C) around the tube (Taken from Ref. [40]. b) Structure or carbon nanotube, with the shapes of different possible aromatic adsorbates marked on the surface (left to right: pyrene, coronene, perylene).

and solubilize carbon nanotubes. A major disadvantage of these techniques is, however, that chemical functionalization, whether directly or defect promoted, induces great perturbations to the nanotube structure, altering the electronic and vibronic properties [5]. Thus, while offering elegant ways to implement certain desired functionalities even on an industrial scale, for investigating the influence of different functional groups on the nanotubes, a less perturbative approach is desirable.

## 2.2. Non Covalent Functionalization

Non covalent functionalization offers ways of attaching functional groups to the nanotube surface without destroying the tubes' extended $\pi$ network, thus inducing only little changes to the pristine nanotube's optoelectronic properties [5]. In non covalent functionalization, several different methods are distinguished.

### 2.2.1. Micellar Suspension

First reports on luminescence from suspended SWCNTs has been reported after separating and encapsulating the tubes using sodium dodecyl sulfate (SDS) micelles [28]. Since then, micelle encapsulation, using surfactants (soaps) has been widely exploited to obtain samples of individualized carbon nanotubes [5, 13, 32, 33, 40–

44]. Amphiphiles within an aqueous environment form micelles, hydrophilic on the outside, hydrophobic on the inside. Carbon nanotubes, being hydrophobic themselves, thus, preferably move to the inside of micelles. In these experiments, bundles are typically separated using kinetic stimulation like ultrasound or stirring. Figure 2.3b shows different possible ways of micelle formation at the nanotube-solvent interface.

### 2.2.2. Adsorption

In contrast to micelle encapsulation, strongly relying on the surrounding medium, several compounds have been attached to carbon nanotubes purely by adsorption, depending less on the surrounding medium. Aromatic molecules like pyrene [45–48], perylene [49] and porphyrine [50] have been shown to adsorb onto the nanotube surface via $\pi$-$\pi$-stacking interactions. Recent work suggests further, that non covalent functionalization utilizing aromatic interactions may be a way of selecting certain nanotube chiralities [49, 51]. Figure 2.3b shows a schematic presentation of different aromatic molecules adsorbed onto carbon nanotubes.

### 2.2.3. Polymer and DNA Wrapping, Endohedral filling

Polymer wrapping is a way of exfoliating carbon nanotube bundles and obtain individual nanotubes [52]. Long polymer chains have been shown to stably wrap around the nanotubes, producing extremely stable complexes [53, 54]. Polymer wrapped nanotubes have been proposed to be ideal for building up highly specialized nanopolymer composites [10–12]. Similarly, DNA molecules have been shown to wrap around carbon nanotubes. Efforts have been devoted to producing DNA sequences, selective to certain tube chiralities, thus creating chirality enriched samples [55, 56].

Endohedral filling of carbon nanotubes has been subject of extensive investigations. Research is dedicated to encapsulation of fullerenes [57, 58], as well as bio molecules and liquids [52].

## 2.3. Solvatochromic Shifts

The electronic states of a molecule in general depend on the dielectric environment, solvents, surfactants, etc. Upon changing this environment, shifts in the energies can be observed. These shifts are the so called solvatochromic shifts, giving a measure for the influence of the surrounding medium on the molecule [59].
Choi *et al.* found a linear relation for carbon nanotubes describing the solvatochromic shifts in terms of the tube diameter [60]:

$$E_{ref}^2(\Delta E) = E_{ref}^2(E_{ref} - E_{solvent}) = \frac{c_{solvent}}{d^4}. \tag{2.1}$$

Here, $c$ depends only on the nanotubes' surrounding medium (solvent, matrix, etc.) and d is the diameter of the tube. As the solvatochromic shift $\Delta E$ measures the change in the transition energies, a set of reference energies is needed. Following Ref. [60] transition energies for $\epsilon \approx 1$ can be calculated by:

$$E_{ii}^{Air} = \frac{1241}{A_1 + A_2 d} + A_3 \frac{col(3\theta)}{d^2}. \tag{2.2}$$

The $A_i$ values can be found in Table 2.1. Note that $A_i$ depend on the transition number $E_{ii}$, but $A_3$ depends also on the nanotube chirality. From these the solvatochromic shifts can be calculated. As plotting $E_{ref}^2(\Delta E)$ over $d^{-4}$, yields a linear relationship, fitting the data points with a linear model yields the solvent factor $c$ as the slope. This factor is a measure of the magnitude of the interaction between the nanotubes and their surrounding. From here on for simplicity, c will be referred to as the **solvatochromic shift**.

| | $A_1$ | $A_2$ | $A_3$ Mod((n-m),3))=1 | $A_3$ Mod((n-m),3)=2 |
|---|---|---|---|---|
| $E_{11}$ | 61.1 nm | 1113.6 | -0.077 eV nm$^2$ | 0.032 eV nm$^2$ |
| $E_{22}$ | 87.4 nm | 613.7 | 0.143 eV nm$^2$ | -0.191 eV nm$^2$ |

Table 2.1. $A_i$ values for Eq. (2.2). $A_1$ and $A_2$ depend on the transition $E_{ii}$, while $A_1$ further depends on the tube chirality (n,m) [60].

# 3 | Experimental Methods

Carbon nanotube samples have been characterized using optical spectroscopic methods. This chapter details the experimental systems, starting with two absorption spectrometers, followed by the photo luminescence setup.

## 3.1. Absorption Measurements

### 3.1.1. Lambda 950

Figure 3.1 shows the *PerkinElmer LAMBDA 950 UV/Vis/NIR spectrometer*. Excitation is provided by deuterium and tungsten halogen light sources (1). The wavelength is tuned using holographic double grating monochromators (2) for the UV/Vis (1440 grooves/mm, blazed at 240 nm) and NIR (360 grooves/mm, blazed at 1100 nm), respectively. A beam depolarizer (3) produces isotropically polarized excitation. The chopper (4) is used to alternate between sample and reference compound (5). Finally, the detector system consists of a photomultiplier and peltier cooled PbS and InGaAs detectors (6) [62].
This setup covers a large spectral range of $175 - 3300$ nm, allowing for measurements of the tubes $E_{11}$ transitions at a resolution of $\leq$0.05 nm in the UV/Vis and $\leq$0.20 nm NIR. The disadvantage of the setup is the relatively long acquisition time in the order of ten minutes per spectrum. Further, the setup features a closed sample chamber, minimizing stray light entering the system, but on the other hand not allowing for simultaneous irradiation of the samples. Thus, the setup produces high resolution spectra of static samples, but is not suitable for measuring dynamic samples containing molecular switches.

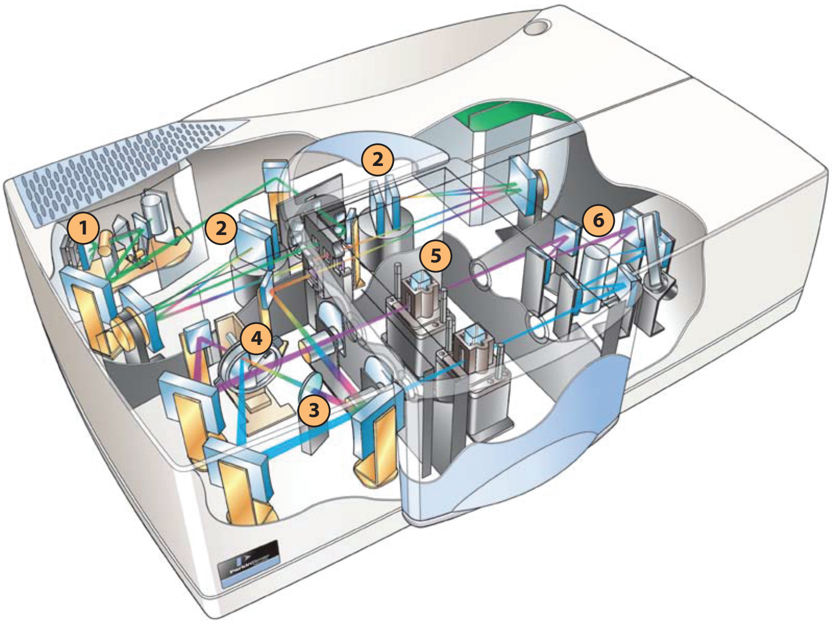

Figure 3.1. Sketch of the PerkinElmer LAMBDA 950 UV/Vis/NIR spectrometer. (1) Deuterium and tungsten halogen light sources, (2) double grating monochromator, (3) beam depolarizer (4) chopper, (5) sample compartment (6) detector system composed of photomultiplier and peltier cooled PbS and InGaAs detectors (adapted from Ref. [61]).

### 3.1.2. Thermo Scientific Evolution Array

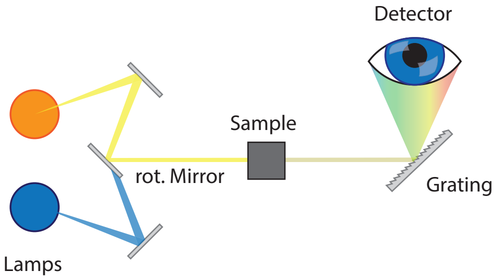

Figure 3.2. Sketch of Thermo Scientific Evolution Array. The two lamp system provides continuous illumination in the range of $190 - 1100\,\mathrm{nm}$. A rotating mirror is used to select one light source. After passing the sample, the signal is expanded by a grating and detected by a photo diode array.

The *Thermo Scientific Evolution Array* is a simple UV/Vis spectrometer. A sketch of the setup is shown in Fig. 3.2. A combination of a deuterium and a tungsten lamp is used to provide excitation in the UV, Vis and NIR [63]. After passing through the sample, the signal is expanded by a single grating monochromator and directed onto a photo diode array (sensitive in the range of 190 – 1100 nm), allowing for simultaneous measurement of the whole spectrum. This setup has the advantage of being extremely fast (typical acquisition time of about 1 s). This way, molecular switch samples sensitive to optical stimuli can be measured without inducing back isomerization. Further, the setup has the advantage of containing an open sample chamber, allowing for external UV irradiation during the measurement. The disadvantage of this system is the relatively small wavelength range only reaching up to 1100 nm.

## 3.2. Photo Luminescence Excitation

Photo luminescence measurements have been have been acquired with a *Horiba Jobin Yvon Fluorolog-3 Spectrofluometer* [64]. The system allows for measuring PL and PLE in solid and liquid samples. A sketch of the setup can be seen in Fig. 3.3. Light source is a 450 W xenon lamp, providing continuous output in the range of 240 nm (UV) to 1000 nm (NIR). A double grating monochromator serves as excitation spectrometer. Between the excitation spectrometer and the sample compartment a slit of adjustable width is acting as a bandpass. A turnable mirror is used to select between two detection geometries. Luminescence can either be collected parallel to incident radiation ("Front Face Configuration" in Fig. 3.3) or perpendicular to the excitation beam ("Right Angle Configuration"). An iHR320 single grating monochromator with three different gratings blazed at 500 nm, 1000 nm and 1200 nm, respectively, for measuring different wavelength ranges. In the iHR320, the signal can be focused either onto a photo multiplier (190 – 860 nm) or a liquid nitrogen cooled InGaAs detector (800 – 1600 nm).

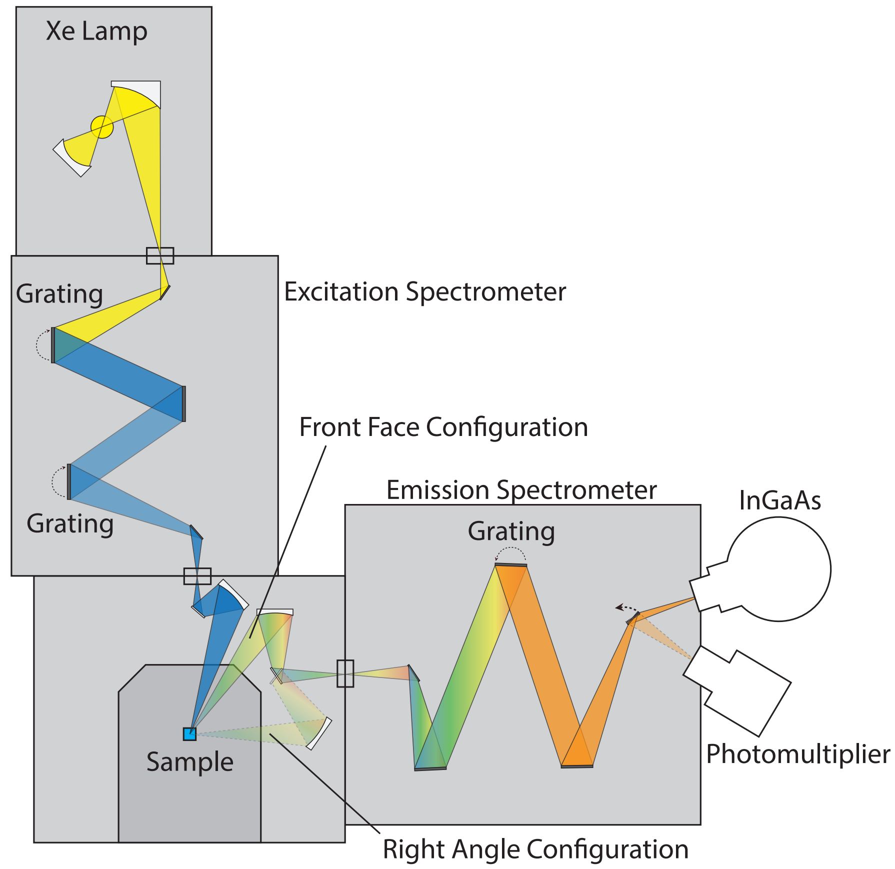

Figure 3.3. Sketch of the Horiba Jobin Yvon Fluorlog-3 spectrofluorometer (adapted from Ref. [64]). Excitation is provided by a xenon lamp and selected by a double grating monochromator. The emitted light can be detected in front face or right angle configuration and is measured by a photomultiplier or an InGaAs detector, after passing and additional single grating monochromator.

# 4 | Amphiphile Engineering

Carbon nanotubes are nano materials consisting only of surface, possessing no bulk volume. They are extremely sensitive to their dielectric environment and the optical properties of carbon nanotubes are highly dependent on nanotube individualization. Whether suspended in a medium or free standing on a surface, it is important to keep the tubes separated, as for example metallic nanotubes in a bundle open non radiative de-excitation channels, consequently, quenching the luminescence. Thus, a requirement for a surfactant is the ability to efficiently individualize carbon nanotubes.

During the design and engineering of an azobenzene derivative able to switch (see chapter 5), we observed effects of the morphology of the amphiphiles on the nanotube suspensions. As this has a technological and fundamental impact, we decided to perform systematic investigations on different aspects of dispersion agents. This is the result of multidisciplinary cooperation within the framework of the SfB658.

Working with suspended nanotubes allows to neglect interaction effects between nanotubes and substrate and, thus, direct investigation of the functionalized tubes. It also offers the possibility to achieve homogeneous coverage of the tube surface. For certain experiments, it is important to suspend the nanotubes in a certain medium. In Raman experiments, for example, organic solvents show strong signals, in some cases like THF and DMF completely cloaking the tube signal. Water, however, is an excellent medium for such measurements and also offers the advantage of being non toxic, cheap and extremely easy to handle. Therefore, a good surfactant should be able to efficiently stabilize carbon nanotubes in water. Furthermore, a high nanotube density is desired, simply to obtain stronger signal, when performing optical experiments, such as photo luminescence, Raman or absorption measurements. A high tube density is also desirable for depositing functionalized tubes onto surface structures, especially with the aim of up scaling these procedures to industrial quantities and preparing large amounts of functionalized tubes at the same time.

In this chapter, different amphiphiles are used to suspend carbon nanotubes in water. These amphiphiles consist of three main parts. First of all, alkyl chains of different lengths ($C_{12}$, $C_{16}$, $C_{22}$) are used to attach onto carbon nanotubes, as alkyl chains have been shown to be a very efficient **anchor group** [13]. Secondly, polyglycerol **dendrons** of different generations are used to achieve water solubility (G1, G2, G3). Each generation roughly consists of two dendrons of the generation before. The G2 dendron for example consists of two G1 dendrons connected by an oxygen atom. The last element is a **linker group** connecting anchor and dendron. This group can be as simple as a methylacetamide, a triazol pentagon, a phenyl group or a combination of those. A sketch of the amphiphiles used in this chapter can be found in Fig. 4.1, the detailed structures can be found in Fig. A.1 and Fig. A.2. As can be seen, the amphiphiles are classified into three groups, the molecules in each group only differing in one part (anchor, dendron or linker), while being identical in the other two.

In this chapter, the effect of varying alkyl chain length, dendron size and linker composition with regard to the quality of produced nanotube suspensions (tube density, luminescence intensity, chiral selectivity) will be investigated. The results discussed in this chapter have been partially published in Ref [42].

## 4.1. Sample Preparation

CoMoCAT nanotubes from Southwestern Nanotechnologies, all belonging to the same production batch were dispersed in water at a starting concentration of 0.01g/L. Amphiphiles were added at a concentration of $10^{-4}$ Mol/L. The dispersions were then tip sonicated for one hour at ≈20 W and subsequently centrifuged for one hour at 31 000 g and 27° C. The resulting supernatant was collected and used for the experiments.

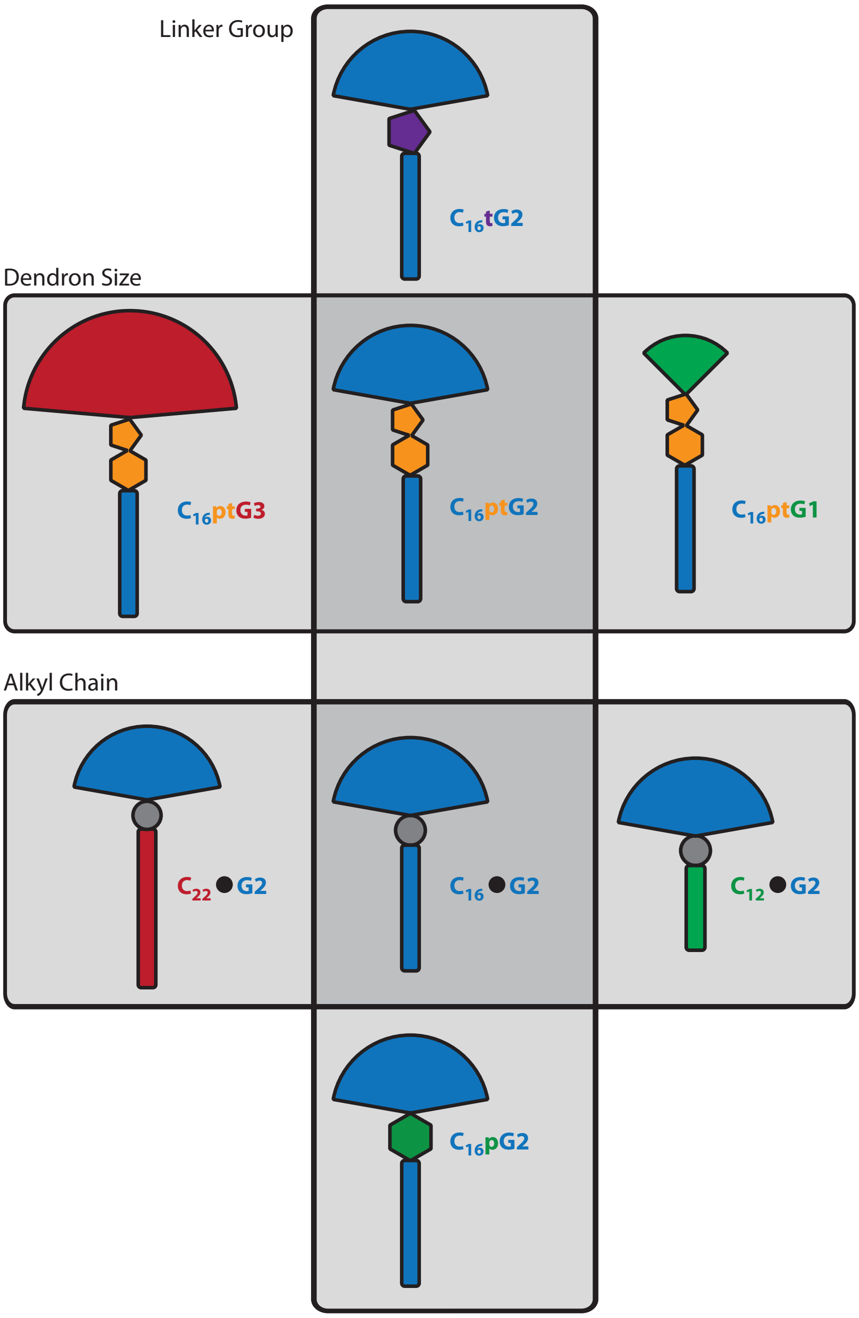

Figure 4.1. Structures of the compounds used in this chapter. It can be seen that the amphiphiles are distinguished in three categories, denoted by the three gray boxes. Within each group the molecules differ in only one feature, namely dendron size (or generation), anchor length or linker group. The full structure of the amphiphiles can be found in Fig. A.1 and Fig. A.2.

## 4.2. Alkyl Chains as Nanotube Anchors

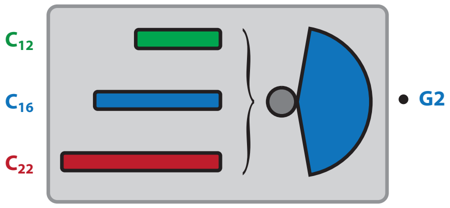

Figure 4.2. Schematic representation of the amphiphiles investigated in this section. As can be seen, the molecules only differ in the length of the alkyl chain (Again, the full structure of the amphiphiles can be found in A.1 and A.2).

Various organic surfactant have been shown to interact strongly with the tube surface. Using these moieties as anchor groups allows molecular agents to adsorb to the tubes' sidewalls [45, 49, 65]. The interaction between carbon nanotubes and amphiphilic surfactants in water primarily involves the lipophilic part. It was found that alkyl chains as an anchoring moiety can be used to promote nanotube de-bundling and, as a matter of fact, the first and one of the most commonly used surfactants for nanotube dispersion, SDS, is based on an alkyl chain [13].

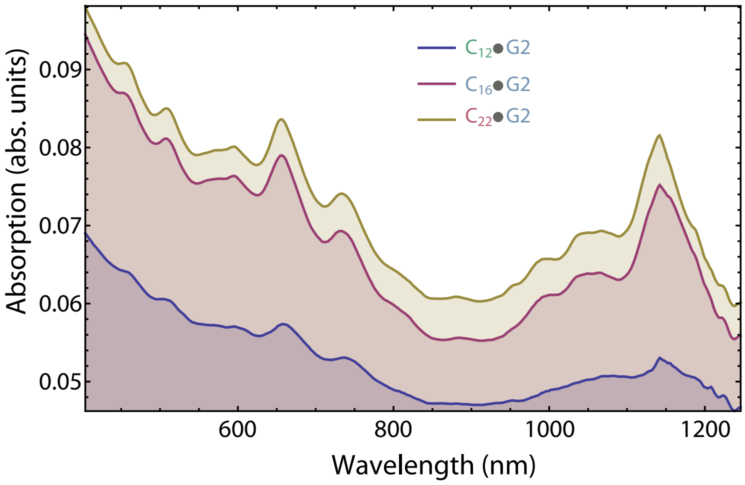

Figure 4.3. Absorption measurements of carbon nanotubes in water, solubilized with amphiphiles bearing alkyl chains of different lengths. Strongest absorption is observed in the case of the longest chain (**$C_{22}$•G2**, $C_{22}$), followed by the amphiphile possessing a medium chain (**$C_{16}$•G2**, $C_{16}$). The signal is weakest in the case of the shortest chain (**$C_{12}$•G2**, $C_{12}$), indicating the lowest tube density.

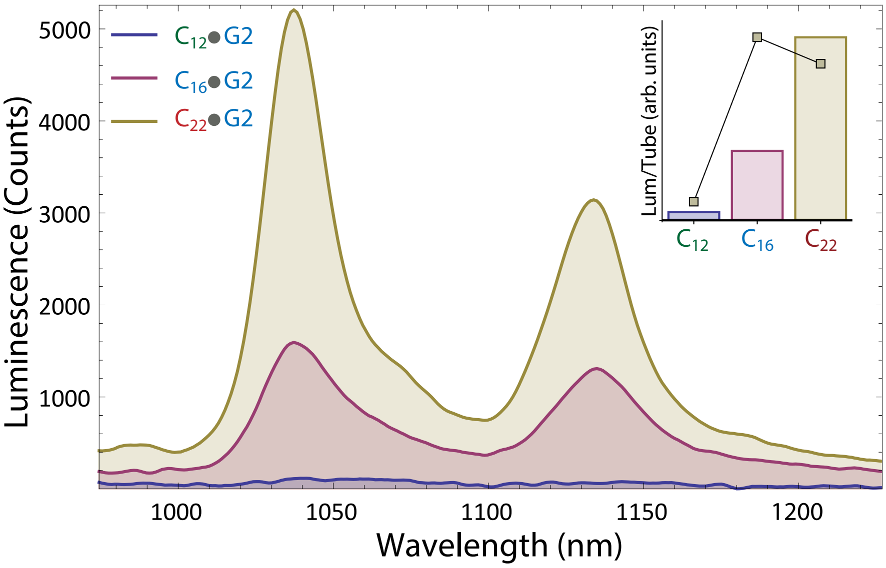

Figure 4.4. Luminescence spectra of HiPCO nanotubes solubilized in water, excited at 632 nm (1.95 eV). As can be seen, strongest luminescence is observed for the sample containing the longest chain, the medium chain results in a weaker signal an for the shortest chain, almost no luminescence can be seen, at all. The inset shows the luminescence per nanotube as a bar chart, as well as normalized by the bundle density (scatter plot).

The first set of amphiphiles used in our investigations differ only in the number of carbon atoms in their respective alkyl chains to investigate the influence of the chain length onto the tube de-bundling and solubility.

Figure 4.3 shows absorption spectra of HiPCO nanotubes in water, suspended using $\mathbf{C_{12}}$**•G2**, $\mathbf{C_{16}}$**•G2**, and $\mathbf{C_{22}}$**•G2**. With increasing length of the alkyl chain, the absorption gets stronger. However, as the absorption setup actually measures transmittance, it has to be noted that what seems like stronger absorption, could in fact just be a higher amount of scattering. This is important, as a rise in absorption indicates more nanotubes in the sample, while more scattering rather indicates larger objects (i.e. bundles). From the increased absorption background in Fig. 4.3, an increasing abundance of SWCNT bundles is observed with increase in chain length.

To understand whether the loss in transmission intensity is due to scattering (more bundles) or increased absorption (more tubes), PL measurements provides a viable tool. As bundling of carbon nanotubes leads to quenching of the luminescence, a

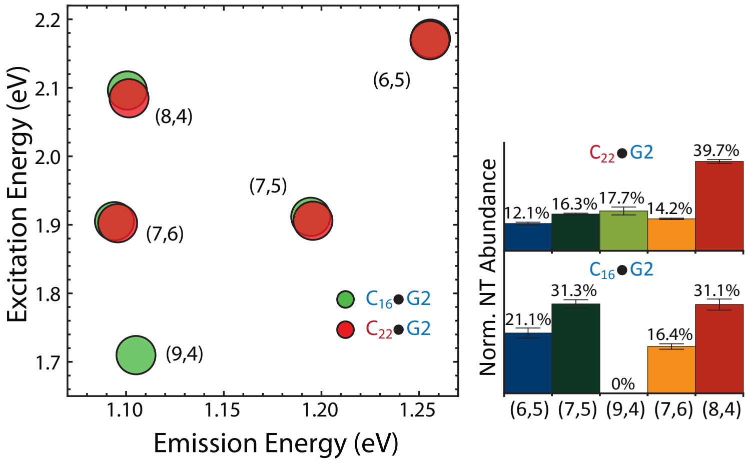

Figure 4.5. left: PLE peak positions for the **C$_{22}$•G2** (long chain) and **C$_{16}$•G2** (medium chain) samples. The **C$_{12}$•G2** sample did not show sufficient emission to determine any peak positions. As can be seen, the positions only differ slightly between the two samples, indicating that the chain length does not induce large changes to the tubes' chemical environment. right: Relative PLE intensities for the **C$_{22}$•G2** (long chain) and **C$_{16}$•G2** (medium chain) samples. It is evident that both samples differ in selectivity. While the **C$_{22}$•G2** sample shows a very dominant abundance of the (8,4)-tube, the **C$_{16}$•G2** sample shows similar abundances for the (8.4) and (7,5)-tubes. The (9,4)-tube, however, was not observed in the **C$_{16}$•G2** sample, at all.

strong luminescence together with strong absorption would indicate the presence of many individualized nanotubes, while a weak luminescence would instead point at a large abundance of bundled tubes in the sample. Figure 4.4 shows luminescence of the three samples. The **C$_{12}$•G2** functionalized tubes (blue line) exhibit no luminescence at all, indicating the sample mainly consists of bundles, while the tubes functionalized using **C$_{22}$•G2** have the strongest luminescence (yellow line). The **C$_{16}$•G2** tubes are, again, intermediate (red line). Thus, it can be seen that, as with the absorption measurements, longer chains result in stronger signal indicating that the increased absorption is indeed the result of a larger number of nanotubes. When comparing the increase in absorption in Fig. 4.3 with the increase in luminescence, especially between the C$_{16}$ and C$_{22}$ chain, it becomes apparent that, while the absorbance only slightly increases, the increase in luminescence is much stronger. Thus, while there are certainly more tubes in solution, the C$_{22}$ chain is much more efficiently de-bundling the nanotubes, while the ability to suspend tubes, as seen by the sample density, is much more similar between both amphiphiles. This is illustrated in the inset of Fig. 4.4, showing a bar chart of the average luminescence per tube, derived from the areas of the luminescence ($I_\lambda$) and absorption peaks (A) at 650 nm, after background subtraction:

$$\Phi_{650nm} = \frac{I_{1030nm} + I_{1130nm}}{A}. \tag{4.1}$$

The scatter plot in the inset of Fig. 4.4 shows the average luminescence per tube, normalized by the bundle density, taken from the absorption background. As can be seen, this value is maximized for the $C_{16}$ dendron. The reason for that behavior is, that while the $C_{22}$ chain results in higher average luminescence, the sample also contains more bundles. Note that small bundles of about three nanotubes can contribute to the luminescence, as long as no metallic tubes are contained.
As the **$C_{12}$•G2** covered tubes did not show any luminescence, only PLE maps of the **$C_{16}$•G2** and **$C_{22}$•G2** functionalized tubes can be compared. As can be seen in the pseudo PLE map in the left part of Fig. 4.5, the nanotube peak positions between the two samples only shift slightly and not uniformly, indicating that indeed the tube-amphiphile interaction is slightly different for both amphiphiles. Going from $C_{16}$ to $C_{22}$, the (8,4) tube for example mainly red shifts in the $E_{22}$ transition energy (excitation), while the (7,5) tube exhibits a red shift in the $E_{11}$ transition (emission) and a blue shift in the $E_{22}$ transition. Table 4.1 shows the solvatochromic shifts calculated from the PLE maps.
Comparing the relative tube abundances in both samples, it becomes apparent that even though both molecules have very similar structures, they do lead to very different sample compositions. A reason for this could be the different micellar structures. While **$C_{22}$•G2** has a critical micelle concentration (CMC) of 14 $\mu$ Mol/L, the CMC of **$C_{16}$•G2** is six times higher (the CMC of **$C_{12}$•G2**even exceeding 1000 $\mu$ Mol/L, see Ref. [42, 66] and references therein).

| Compound | Solv. Shift ($E_{11}$) | Solv. Shift ($E_{22}$) |
|---|---|---|
| **$C_{12}$•G2** | - | - |
| **$C_{16}$•G2** | 0.062±0.004 | 0.25±0.004 |
| **$C_{22}$•G2** | 0.057±0.004 | 0.28±0.004 |

Table 4.1. Solvatochromic shifts of the carbon nanotubes solubilized using **$C_{22}$•G2** and **$C_{16}$•G2**, respectively. Even though the longest chain resulted in strongest luminescence, as well as absorbance, the medium chain sample seems to exhibit stronger interaction with carbon nanotubes. However, it has to be noted that due to the absence of the (9,4)-tube in the **$C_{16}$•G2** sample, as well as the small overall PLE shifts between the two samples, the actual solvatochromic shift of the **$C_{16}$•G2** sample is probably found at the lower boundary of the error interval (the plots can be found in the appendix in Fig. A.3 and A.4).

## 4.3. Dendron size

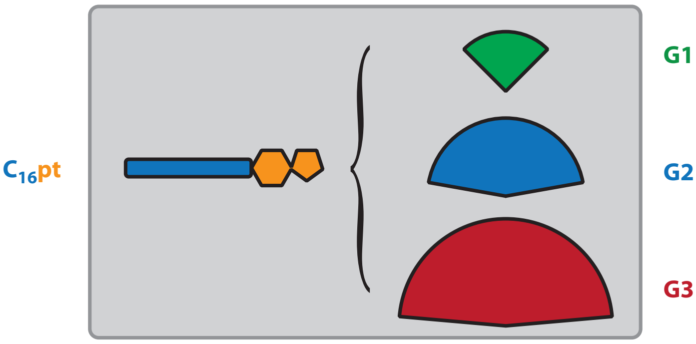

Figure 4.6. Schematic representation of the amphiphiles investigated in this section. As can be seen, the molecules only differ in the size of the polyglycerol dendron (Again, the full structure of the amphiphiles can be found in A.1 and A.2).

Preparing samples in water is desirable for many applications. Water is cheap, non volatile, available, non hazardous and easy to handle. Furthermore, when working with carbon nanotubes, water is a perfect environment for certain spectroscopic methods like Raman spectroscopy. Water does not exhibit any Raman

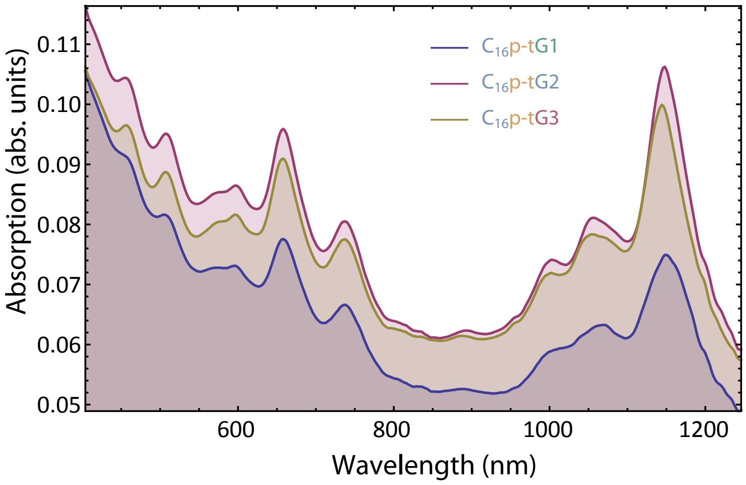

Figure 4.7. Absorption measurements of carbon nanotubes suspended in water using molecules containing different generations of polyglycerol dendrons. Lowest overall absorption yield is found for the first generation molecule (**$C_{16}$p-tG1**), while the second generation dendron (**$C_{16}$p-tG2**) leads to the strongest absorption. The third generation dendron, however, leads to a slight decrease again.

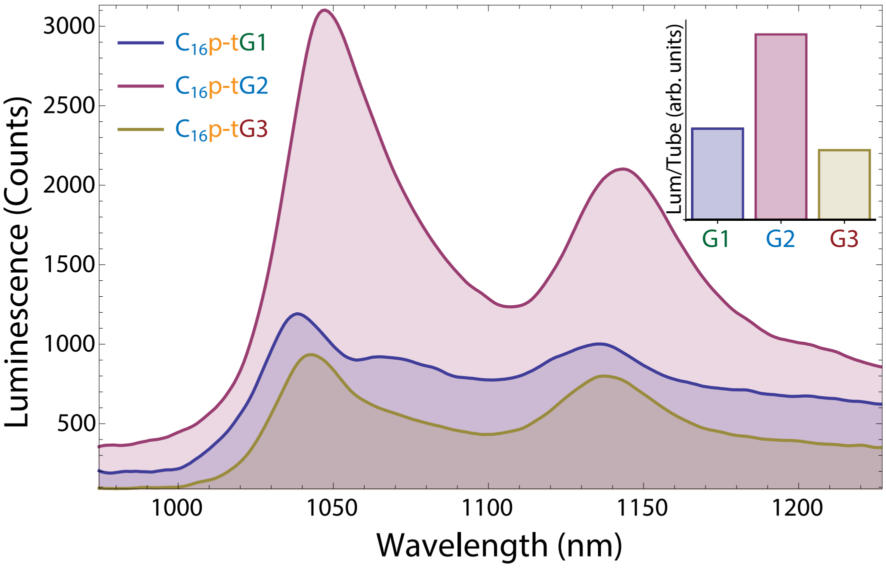

Figure 4.8. PL spectra of carbon nanotubes suspended in water using **$C_{16}$p-tG1**, **$C_{16}$p-tG2** and **$C_{16}$p-tG3**. Excitation was provided at 632 nm. The generation two dendron shows to the strongest signal, followed by the first and then third generation dendron.

signal in the spectroscopic region where the characteristic nanotube features can be found. Thus, designing amphiphiles with highest possible water solubility is desirable. To this end, three amphiphilic compounds consisting of a $C_{16}$ alkyl chain followed by an aromatic linker and polyglycerol dendrons of different sizes were investigated on their ability to suspend nanotubes.

Every generation of the dendron consists of two molecules of the generation before plus a small linker. The generation three dendron, for example, consists of two generation two dendrons or four generation one dendrons. Thus, the size roughly doubles with every generation. It has been shown that the critical micelle concentration (CMC) of these amphiphiles, that is the amphiphile concentration needed before micelles are formed, decreases with increasing dendron size [66]. As an amphiphiles ability to suspend carbon nanotubes is closely related to the CMC, it would expected that increasing the dendron size would lead to an increase in nanotube density and possibly improved de-bundling.

However, when looking at the absorption spectra of carbon nanotubes suspensions using the amphiphiles **$C_{16}$p-tG1**, **$C_{16}$p-tG2**, and **$C_{16}$p-tG3** (see Fig. 4.7), it can

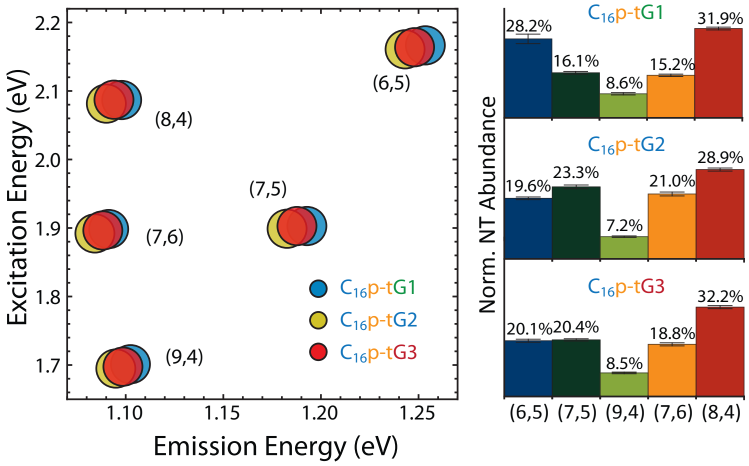

Figure 4.9. left: PLE peak positions for carbon nanotube samples functionalized with molecules of different sized polyglycerol dendrons. It can be seen that the third generation sample peaks can be found in between the other two. The second generation sample peaks are uniformly located at low energies. right: Relative sample composition of carbon nanotubes in water suspended using **$C_{16}$p-tG1** **$C_{16}$p-tG2** and **$C_{16}$p-tG3**, obtained from PLE experiments. Apart from the stronger abundance of the (6,5)-tube in the **$C_{16}$p-tG1** sample, all samples exhibit similar compositions.

be seen that the highest nanotube density can be observed when using the generation two dendron, while the generation three dendron leads to a slight decrease. The lowest tube density is - as expected - found for the generation one dendron. PL measurements of the samples (see Fig. 4.8) reveal that the second generation dendron also seems to be the most efficient in individualizing the tubes, resulting in a strong luminescence. Interestingly, the samples prepared using the generation three dendron show the lowest PL signal indicating, together with the relatively strong absorption, that the amphiphile works well as a solubilization agent for carbon nanotubes, but is ineffective in de-bundling them.

As the amphiphiles only differ in their dendron size, the relative nanotube compositions of all samples are expected to be very similar. This is confirmed by the histograms in Fig. 4.9 (right). Apart from a stronger (6,5)-abundance in the **$C_{16}$p-tG1** sample all three samples exhibit similar tube compositions.

Figure 4.9 (left) shows the positions of the carbon nanotube luminescence peaks for all three samples. The strongest red shift can be observed for the generation two sample, while the generation one sample exhibits the smallest red shift, generation three lying intermediate. Therefore, the amphiphile-tube interaction seems strongest for the PG2 sample.

Table 4.2 shows the solvatochromic shifts for the **$C_{16}$p-tG1**, **$C_{16}$p-tG2** and **$C_{16}$p-tG3** sample. As expected from the PLE peak positions, the **$C_{16}$p-tG2** sample (generation two) exhibits the biggest slope and, thus, the strongest amphiphile-tube interaction, while **$C_{16}$p-tG1** interacts comparatively weak. In contrast to the samples with differing chain length, here the molecules' CMC does not differ as much. The CMCs for the G1, G2 and G3 molecule in water are 15 $\mu$Mol/L, 11 $\mu$Mol/L and 7.1 $\mu$Mol/L, respectively. However, the micelle shapes where found to be very different. Amphiphiles carrying G1 dendrons have been shown to build up tube shaped micelles, while G2 and G3 dendrons form spherical micellar structures [66]. So, even though the tubular micelle forming G1 compound would be expected attach optimal to carbon nanotubes, as the micellar shape could basically stay the same, the G2 carrying compound is bound stronger.

| Compound | Solv. Shift ($E_{11}$) | Solv. Shift ($E_{22}$) |
|---|---|---|
| **$C_{16}$p-tG1** | 0.058±0.005 | 0.27±0.03 |
| **$C_{16}$p-tG2** | 0.064±0.005 | 0.27±0.03 |
| **$C_{16}$p-tG3** | 0.062±0.005 | 0.27±0.03 |

Table 4.2. Solvatochromic shifts of the carbon nanotube samples suspended using molecules with different dendron generations. The slopes indicate strongest amphiphile-tube interaction for the generation two dendron (the plots can be found in the appendix in Fig. A.5 and A.6).

## 4.4. Linker Group

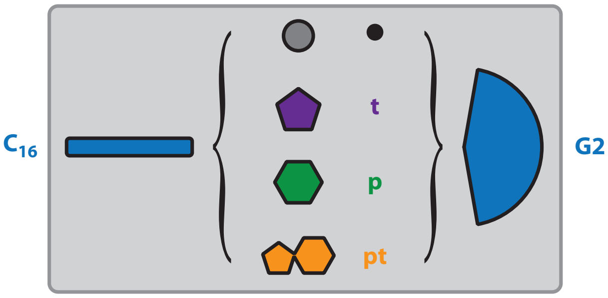

Figure 4.10. Schematic representation of the amphiphiles investigated in this section. As can be seen, the molecules consist of the identical alkyl chains and dendrons, while the linking moiety, connecting the two parts has been replaced (Again, the full structure of the amphiphiles can be found in A.1 and A.2).

After investigating the effect of varying the chain length and dendron size, it is time to take a look at the effect of the intermediate moiety. For these investigations,

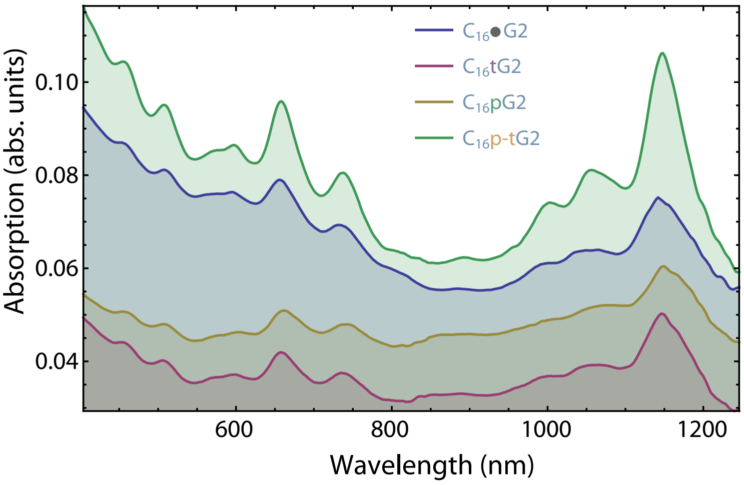

Figure 4.11. Absorption measurements of carbon nanotube samples suspended using similar molecules, differing only in the linker moiety between anchor chain and water soluble dendron. It can be seen that all samples show significantly different spectra. Strongest absorption is found for the phenyl group combined with a triazol pentagon (green line), followed by the N-methylacetamide linker (blue line), the single phenyl group (yellow line) and finally the single triazol pentagon (red line).

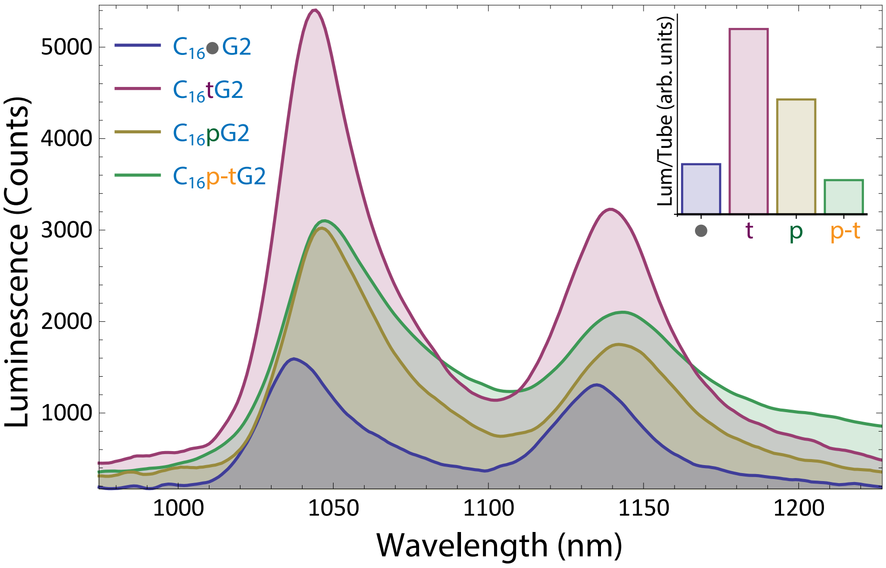

Figure 4.12. Photo luminescence measurements of carbon nanotube samples utilizing amphiphilic surfactants containing different linker groups. Excitation was provided at 632 nm. It can be seen that the strongest emission can be observed using the amphiphile linked by the single triazole pentagon (red line), followed by the combination of a phenyl group and a triazol pentagon (green line), the phenyl moiety (yellow line) and finally the N-methylacetamide (blue line).

all samples possessed a $C_{16}$ chain and a G2 dendron. Intermediate groups used in this chapter are a N-methylacetamide (•), a triazol pentagon (**t**), a phenyl group (**p**) and a combination of a phenyl group and a triazol pentagon (**p-t**). At first glance, it is not seem obvious that this group should have a large influence on the tube-amphiphile interaction, as they are supposedly rather far away from the tube surface (≈1.8 nm for a $C_{16}$ chain).

Absorption measurements in Fig. 4.11 of the tube-amphiphile complexes show strongest nanotube density for the sample containing the **p-t** group (green line), followed by the • group (blue line). The **p** and **t** samples exhibit much weaker absorption and, thus, tube density. Therefore, even though all four amphiphiles consist of essentially the same interacting moieties - $C_{16}$ chains interacting with the tubes and G2 dendrons interacting with the surrounding water - their abilities to suspend nanotubes differ greatly. It has to be noted that, apparently, the aromaticity of the linker groups does not seem to be the reason as for example the **p-t** and **p** samples result in a very different tube density.

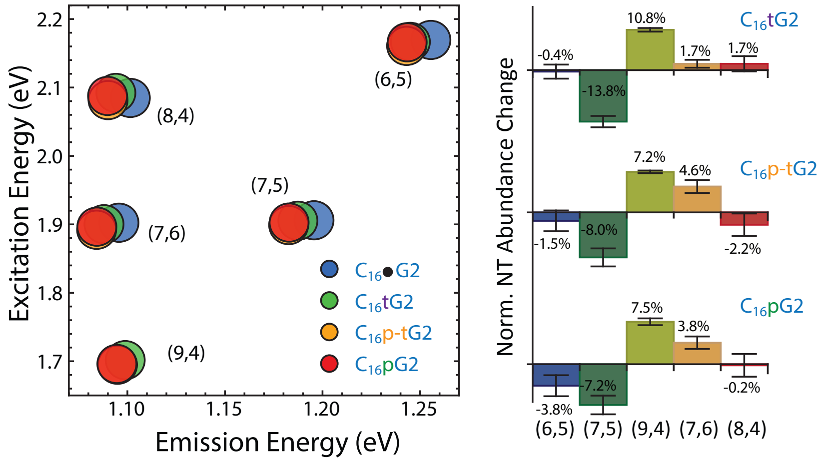

Figure 4.13. Left: PLE peak positions for carbon nanotube samples made using amphiphiles containing different linker moieties. Strongest over all red shifts can be observed for the samples containing phenyl linkers (red circles) and the combination of phenyl and a triazol pentagon (yellow circles), followed by the single triazol pentagon (green circles) and finally the N-methylacetamide (blue circles). Right: Change of the relative sample compositions of carbon nanotube samples made using amphiphilic surfactants bearing different linker groups, compared to the **$C_{16}$•G2**sample. It can be seen that there are different between all four samples.

Figure 4.12 shows PL measurements for the four samples. Interestingly, here the **t** sample results in the strongest luminescence, despite its weak absorption. This indicates that, it is highly efficient in suspending individualized nanotubes in contrast to bundles. The weakest signal is found for the • sample, the other two lying in between. Again, very different behaviors for all four samples can be observed.

Most interestingly, the positions of the carbon nanotube peaks in the four samples change radically (see Fig. 4.13, left). The strongest relative red shifts can be observed for the **p** (red circles) and the **p-t** samples (yellow circles), followed by the **t** sample (green circles) and, lastly, the • sample (blue circles). This yet again showing a different behavior than in both, the absorption and luminescence measurements. Table 4.3 shows the solvatochromic shifts for all four samples. Here, not only the peak position, but also its dependance on the tube diameter matter. It can be seen that the strongest interaction can be observed for the **t** sample, followed by the **p** and the **p-t** samples and in the end the • sample.

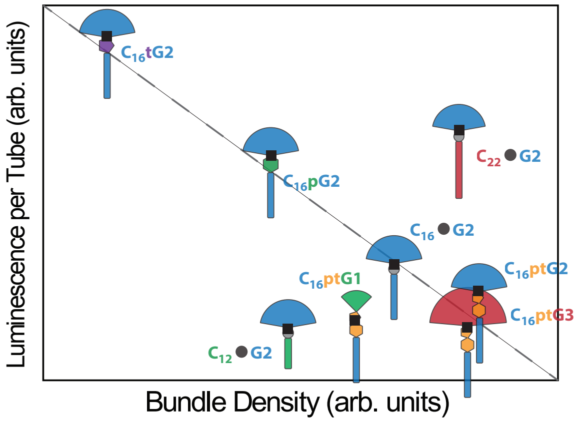

Figure 4.14. Plot of the average luminescence per tube over the sample density. **C$_{16}$tG2** gives the highest luminescence, while at the same time achieving highest de-bundling. A general trend is observable, indicating a correlation between strong average luminescence and bundle density. It has to be noted, that this trend only seems valid for the C$_{16}$ compounds, while the C$_{12}$ and C$_{22}$ molecules show the strongest deviations.

A look at the chiral distributions of the samples reveals different selectivities between the amphiphiles (see Fig. 4.13, right). The (9,4) tube, for example is hardly present in the **C$_{16}$•G2** sample, but shows strong contributions in the other three. The most striking differences can be seen in the decrease of the (7,5) abundance, as well as the increase of the abundance of the (7,6) species.

| Compound | Solv. Shift (E$_{11}$) | Solv. Shift (E$_{22}$) |
|---|---|---|
| **C$_{16}$•G2** | 0.062±0.004 | 0.25±0.02 |
| **C$_{16}$tG2** | 0.065±0.004 | 0.28±0.02 |
| **C$_{16}$pG2** | 0.063±0.004 | 0.27±0.02 |
| **C$_{16}$p-tG2** | 0.064±0.004 | 0.27±0.02 |

Table 4.3. Solvatochromic shifts obtained from E$_{11}$ energies for samples made with amphiphiles containing different linker moieties. The largest slope is found in the triazole pentagon sample, followed by the combination of a phenyl ring and a triazol pentagon, a single phenyl ring and finally a simple nitrogen (the plots can be found in the appendix in Fig. A.7 and A.8).

## 4.5. Summary

Carbon nanotubes were solubilized in water using three groups of polyglycerol derived amphiphiles. First the effect of changes in the anchor groups onto nanotube density and luminescence was investigated by using alkyl chains of various length. Using $C_{12}$, $C_{16}$ and $C_{22}$ chains, it was found that the longest chain resulted in the strongest luminescence per tube and, thus, high efficiency in dispersing individualized SWCNTs. However, apart from stronger luminescence, the stronger absorption background revealed higher bundle density within the $C_{22}$ sample, indicating that, while the sample has very high tube density, as well as average luminescence, still a large numbers bundles persists. Thus, the amphiphile most efficiently dispersing individualized SWCNTs is actually the $C_{16}$ amphiphile. Secondly, different polyglycerol dendron generations were investigated. Here, the most efficient compound was found to be the one, carrying the G2 dendron, producing strong average luminescence and high individualization. Lastly, changing the intermediate groups of the amphiphiles revealed strong influence on the spectral positions nanotubes' $E_{11}$ and $E_{22}$ transitions, as well as the compounds selectivity. This could in principle be exploited for both, static tailoring of the tubes' optoelectronic properties, as well surfactant driven chirality enrichment.

Figure 4.14 shows the average luminescence per nanotube plotted over the bundle density. It can be seen that all samples are located on a straight line. The largest deviations can be observed for the two samples not bearing $C_{16}$ chains. The highest luminescence/bundle density ratio can be observed for the **$C_{16}$tG2** sample. Among the investigated compounds, **$C_{16}$tG2** is, thus, found to be the best at suspending individualized nanotubes.

# 5 Conformational Switch Functionalization

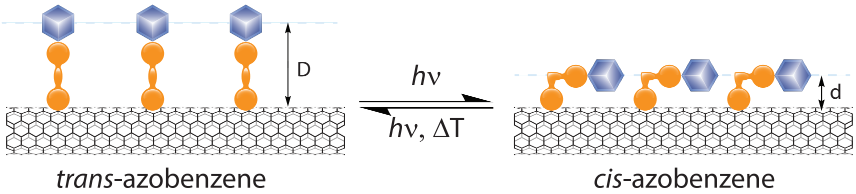

Figure 5.1. Sketch of a SWCNT functionalized with a conformational azobenzene switch (orange). Upon illumination, the molecule passes from a linear *trans* to a bent *cis* structure. Using azobenzene switches, the distance between the nanotube and an attached functional moiety(blue box) can be controlled via the switch isomerization state.

Optical conformational switches are molecules able to transit between two structurally different isomers upon optical excitation. Attaching functional moieties like chromophores to carbon nanotubes via conformational switches offers prospects of reversibly changing the tube-chromophore distance and, thus, interaction strength, subsequently influencing the optoelectronic properties of both depending on the switching state (see Fig. 5.1).

This chapter focuses on the functionalization of SWCNTs with azobenzene compounds. **Section one** introduces conformational switches in general and azobenzenes in particular and gives an overview over the literature connected to nanotube azobenzene functionalization. In **section two**, the sample preparation is explained, followed by a recapitulation of our groups previous work on azobenzene switches [67, 68]. **Section five** describes azobenzene mediated reversible de-bundling of carbon nanotubes [69].

## 5.1. Conformational Switches

### 5.1.1. Azobenzene

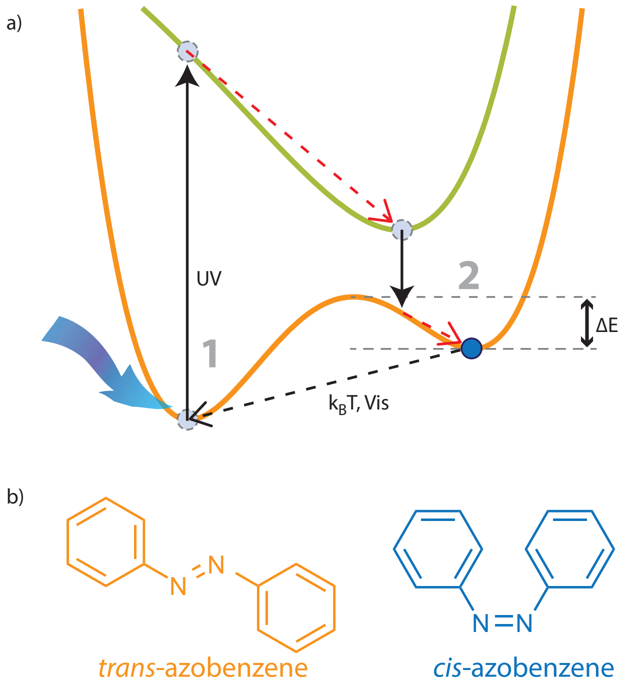

Figure 5.2. a) Sketch of the potential landscape of azobenzene. The switch has a two minima in the ground state (orange line), labeled **1** and **2**, respectively. A system in the **1** ground state is excited upon UV illumination. After internal conversion, a transition from the minimum of the excited state (green line) into minimum **2** of the ground state takes place. From the *cis* state, a thermally or optically activated transition to the **1** state is possible. b) Structures of the azobenzene *trans* (orange) and *cis* (blue) isomers.

Azobenzene is a well known conformational photo switch [71–73]. It is composed of two benzene rings, connected by two nitrogen atoms (Fig. 5.2b). Under ambient conditions mainly in the linear *trans* configuration (E-azobenzene), isomerization into the metastable *cis* state (Z-azobenzene) can be triggered by UV illumination. Figure 5.2a shows a scheme of the isomerization process. The ground state contains

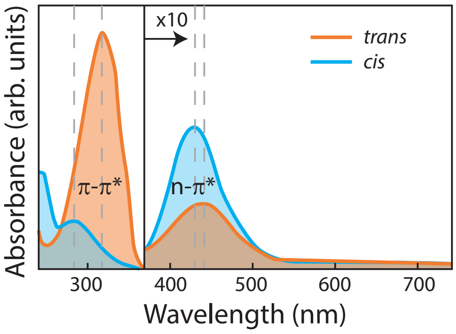

Figure 5.3. Absorption spectra of azobenzene in the *trans* (orange) and *cis* state (blue). While the absorption of the E-isomer is governed by the $\pi - \pi^*$ in the Z-isomer, the $n - \pi^*$ transition is dominant (adapted from Ref. [70]).

two minima (**1** and **2** of *trans* and *cis*, respectively). Upon UV illumination, the molecule is exited from state **1**. After internal conversion, the system transits back into the ground state, however, ending in the metastable state **2**. From there, back isomerization is possible either via optical or thermal stimuli. Note that, depending on the surrounding medium or chemical alterations to the structure, the *cis* isomer might become the stable form.

The absorption spectrum of E-azobenzene is governed by a very pronounced $\pi - \pi^*$ transition located at 320 nm, called the $S_2$ band. A weaker band related to an $n-\pi^*$ transition is located around 445 nm, the $S_1$ band. The switching efficiencies when exciting these transitions are $\phi_{t \to c}^{\pi-\pi^*} = 0.1$ and $\phi_{t \to c}^{n-\pi^*} = 0.25$. After isomerization, the absorption characteristics change drastically. In Z-azobenzene the $S_2$ band is much less pronounced, while the $S_1$ transition now is much more pronounced than in the *trans* form. This is a result of the structural change between the two isomers. While in the planar E-azobenzene, the $n - \pi^*$ transition is forbidden and only occurs because of non-planar distortions [71], the Z-isomer is bent and the $n - \pi^*$ transition is allowed. The $S_0 \rightarrow S_2$ transition band will here forth be referred to as *trans* peak, while the $S_0 \rightarrow S_1$ transition will be called *cis* band.

## 5.1.2. Publication History

In 2007, Simmons *et al.* investigated azobenzene functionalized SWCNT transistors [74]. The nanotube transistors were assembled on a $SiO_2$ surface and non

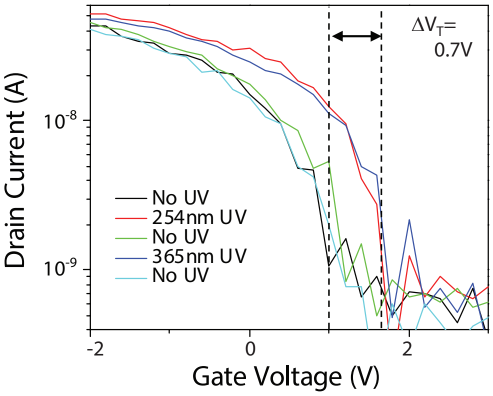

Figure 5.4. U-I characteristics of a nanotube transistor non covalently functionalized with an azobenzene derivative. Upon isomerization to the *cis* state, the threshold voltage shifts about 0.7 V. Back isomerization reverses this effect (Adapted from Ref. [74].

covalently functionalized using an anthracene anchor group. It was demonstrated, that the transistors' UV characteristics were susceptible to the switch state of the attached azobenzene molecules. Upon irradiation, the threshold voltage changes by ≈0.7 V. After back isomerization in darkness, the initially observed signal was restored (see Fig. 5.4). Similar experiments using a pyrene anchor group have been conducted in 2009 by Zhou *et al.* [31], again functionalizing SWCNT FETs. These assemblies can be used as wavelength selective photo detectors. Kim *et al.* showed that this concept also works for graphene transistors. They were able to tune the U-I characteristics and the position of the phonon G-band (i.e. the in-plane carbon vibrations).

Imin *et al.* showed that azobenzene based polymers can be used for chirality selective dispersion of carbon nanotubes in THF and toluene [30]. Depending on the switching state, different chiral compositions were found. Feng *et al.* attached azobenzene covalently to MWCNTs and characterized the different switch states by monitoring the nanotube conductivity [29]. Recently, Kolpac *et al.* proposed a nanotube-azobenzene hybrid structure used as a battery [75]. They modeled a system of densely packed azobenzene molecules, covalently grafted onto nanotubes. They found an increased energy separation between the *cis* and *trans* state as a result of the geometry and proximity induced interactions. Within these hybrid structures, theoretically, very high energy densities are possible, making them ideal for energy storage.

In contrast to the functionalization schemes in literature, exploiting azobenzene for tailoring the tubes' optoelectronic properties, we use a approach, non covalently functionalizing nanotubes in aqueous solution. This offers the advantage of homogeneously covering and investigating large ensembles of tubes, while only inducting minimal alterations to the tubes' band structure. This allows for simultaneous investigations of different nanotube chiralities using photo luminescence spectroscopy.

## 5.2. Previous Experiments

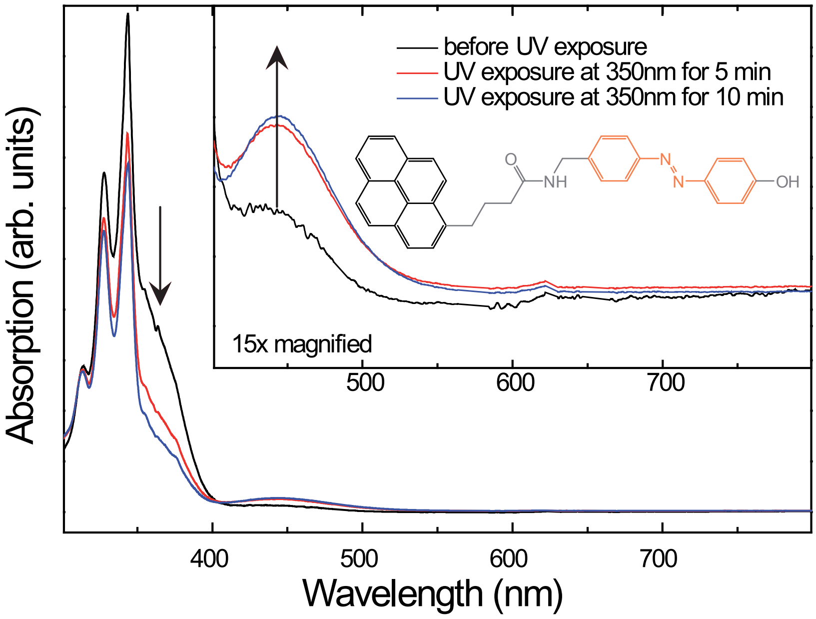

Figure 5.5. Absorption spectrum and structure of pyrene-azobenzene-OH compound. The spectrum consists of a pyrene contribution in the UV and the azobenzene *trans* absorption at 350 nm. After UV irradiation, isomerization leads to the *trans* band decreasing, while the *cis* peak at 450 nm rises (Taken from Ref. [68]).

In Ref. [68] several azobenzene derivatives were investigated in an attempt to functionalize carbon nanotubes. Figure 5.5 shows the structure and absorption spectra of an azobenzene compound connected to a pyrene anchor group on one end and a hydroxy group on the other. As can be seen, the spectrum consists of the characteristic pyrene absorption bands in the UV, as well as the azobenzene *trans* absorption peak at 350 nm. After UV irradiation, isomerization is triggered and the azobenzene trans peak decreases while at 450 nm the azobenzene *cis* peak rises.

A first attempt to manufacture a water soluble azobenzene switch was prepared by replacing the hydroxy group with polyglycerol dendrons (G2) connected to the azobenzene moiety. As has been shown in Chapter 4, polyglycerol dendrons work remarkably well for suspending carbon nanotubes in water. The structure of this compound can be seen in Fig. 5.6. As can be seen it consists of a pyrene

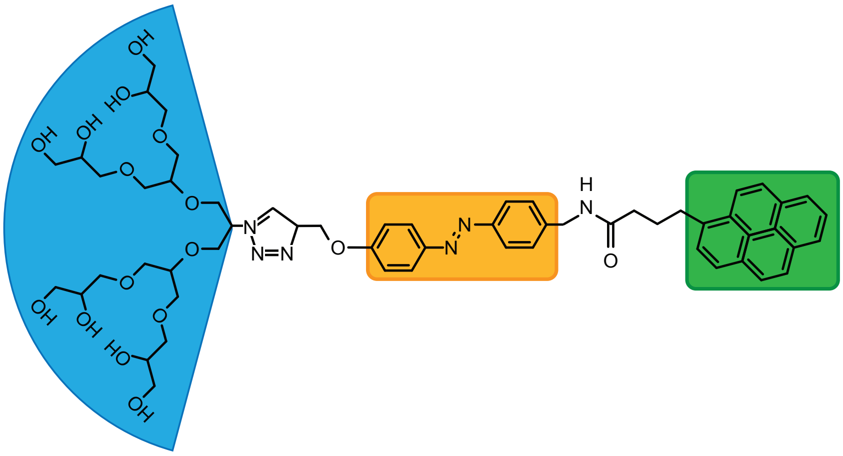

Figure 5.6. Structure of pyrAZO. The molecule consists of a pyrene anchor group used to attach covalently onto carbon nanotubes (green), a polyglycerol group to enable water solubility (blue) and an azobenzene switch moiety (orange).

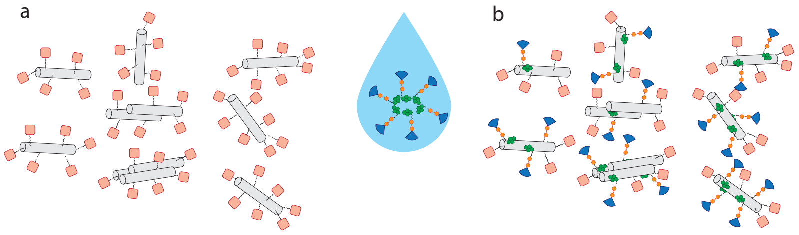

Figure 5.7. Sketch of surfactant replacement procedure. (a) CNTs are suspended using one SDS (red). pyrAZO (green, orange and blue) is added to the sample and sonication and centrifugation is applied (drop). (b) depending on the amount of added pyrAZO, some of the SDS has been replaced by pyrAZO.

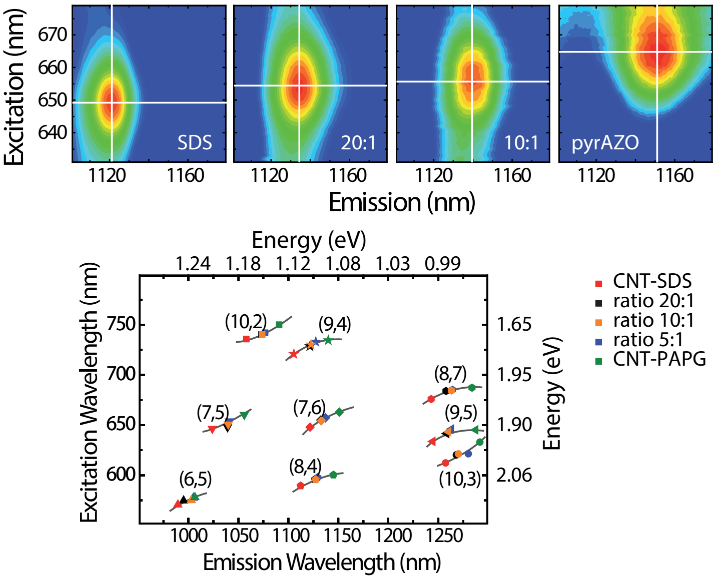

Figure 5.8. Top: PLE signal of the (7,6) tube functionalized with SDS (left) increasing additions of pyrAZO (two middle panels) and using only pyrAZO (right). The sample containing both, SDS and pyrAZO exhibits peak positions intermediate of those using only one surfactant. Bottom: Pseudo PLE map showing the peak positions for a variety of different nanotubes with different SDS:pyrAZO ratios.

anchor (green), an azobenzene switch (orange) and a G2 dendron (blue) (here forth called pyrAZO). Pyrene was chosen as anchor group, as it has been shown to be an effective in adsorbing onto carbon nanotubes [31, 45].

First investigations of the compound before and after nanotube functionalization quickly revealed that it was unable to undergo the isomerization process. Saalfrank *et al.* showed that the isomerization behavior of push-pull azobenzenes (azobenzenes functionalized at the para 4-4-positions) highly depends on the functional groups as well as the dielectric constant of the solvent [76]. In the case of pyrAZO, the azobenzene *trans* absorption band is shifted into the pyrene bands, thus, leading to large spectral overlap, subsequently strongly suppressing the isomerization.

Nevertheless, pyrAZO was used to investigate the effects of surfactant replacement onto carbon nanotubes. HiPCO nanotubes were suspended in water using SDS. Different amounts of pyrAZO were added to the suspensions and sonication was applied. As a result, the SDS at the nanotube-solvent interface was partially replaced by pyrAZO moieties (see Fig. 5.7). Finally, CNTs were suspended using

only pyrAZO.
It was found that pyrAZO is able to efficiently disperse and debundle carbon nanotubes. Photo luminescence experiments were used to compare SDS and pyrAZO functionalized nanotubes. The top part of Fig. 5.8 shows the position of the (7,6) chirality's PLE signal. Adding different amounts of pyrAZO to SDS suspended nanotubes leads to a shift of the peak position towards the value found for pyrAZO suspended tubes, thus indicating the replacement of SDS at the tube-water interface by pyrAZO.

## 5.3. Reversible De-bundling of CNTs

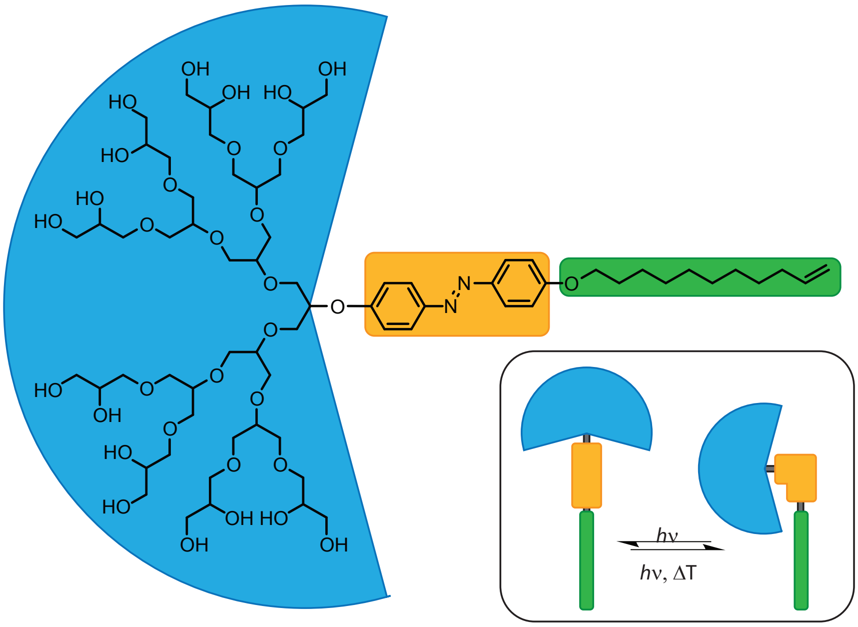

Figure 5.9. Structure of the new AlkAzoG3 switch. It consists of three main parts: A third generation polyglycerol dendron (blue), a $C_{11}$ alkyl chain as tail group (green) and the azobenzene switch moiety as a linker in between (orange). The inset box shows the structural change upon illumination. Once irradiated with UV light, the azobenzene undergoes a trans to cis isomerization and the molecule gets bent.

As the pyrAZO compound lost its switching capabilities due to the spectral overlap between the azobenzene and pyrene moieties, a new compound (alkAZO) utilizing a different anchor group was prepared. In chapter 4 a G2 dendron combined with a $C_{16}$ chain has been found to be highly efficient in solubilizing carbon nanotubes.*Koerdel et al.* synthesized and investigated different compounds consisting of alkyl chains, azobenzene and PG dendrons [77]. It was found that most compounds investigated showed very low *trans* → *cis* conversion rates below 50%. The highest conversion rate of 70% was found for $C_{11}$-Azobenzene-G3 (see Fig. 5.9), making it the prime candidate for our experiments. Interestingly, the CMC of the *cis* isomer was found to be about ten times larger than for the *trans* isomer. Isomerization of the compounds, thus, leads to breaking of the micellar structures.

Upon isomerization, the molecule changes from a straight to a bent form (see Fig. 5.9, inset). In contrast to the azobenzene derivative used in the last section, this molecule is thought to mostly interact with the nanotubes by forming micelles around them instead of strong adsorption through an aromatic anchor group. After switching to the cis form, however, the amphiphile is not able to retain stable micelles. It was proposed that isomerization would as well lead to precipitation of the tubes and de-bundling.

Light driven precipitation of carbon nanotubes has very interesting prospects for nanoelectronics, as it would allow for spacial selective nanotube deposition. If the re-bundling process is found to be reversible, it would allow for controlling the nanotube density within a solution at will.

### 5.3.1. Sample Preparation

HiPCO nanotube from Unidym, all belonging to the same production batch were dispersed in water at a starting concentration of 0.01g/L. Azobenzene derivatives were added at a concentration of $10^{-4}$ Mol/L and tip sonicated for one hour at ≈20 W and subsequently centrifuged for one hour at 31 000 g and 27° C. The resulting supernatant was collected and used for the experiments.

### 5.3.2. Investigation of the Azobenzene Nanotube Complexes

The absorption spectra confirm the abundance of both, alkAZO (see Fig. 5.10, left) and nanotubes (see Fig. 5.10, right) inside the sample. UV irradiation leads to a

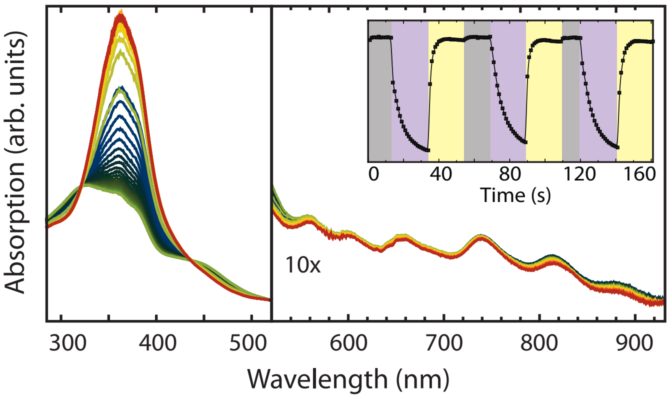

Figure 5.10. Absorption spectra of HiPCO nanotubes functionalized with alkAZO. The left part of the spectrum shows the azobenzene contribution. Upon illumination the 350 nm trans band starts to decrease while a 450 nm cis band arises. As it is a two state system, an isosbestic point around 440 nm can be observed. The right part of the spectrum shows the nanotube contribution magnified by a factor of 10 for better visibility. The inset shows the area of the azobenzene trans peak for several isomerization cycles.

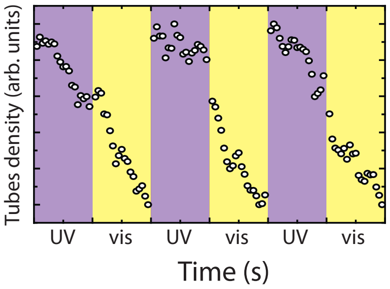

Figure 5.11. Carbon nanotube concentration derived from the absorption background at 670 nm over the course of three switching cycles. Each visible irradiation is followed by a short sonication step in order to stir up tube bundles and promote re-encapsulation

decrease of the azobenzene $\pi - \pi^*$ transition band (*trans* band), as well as a rise of the $n - \pi^*$ absorption band (*cis* band). As alkAZO is a two state system, an isosbestic point can be observed around 440 nm. The isomerization process is fully reversible, as is shown for several isomerization cycles in the inset of Fig. 5.10. Monitoring the absorption behavior over several switching cycles (see Fig. 5.11), it can be seen that during the UV irradiation, the nanotube density in the samples

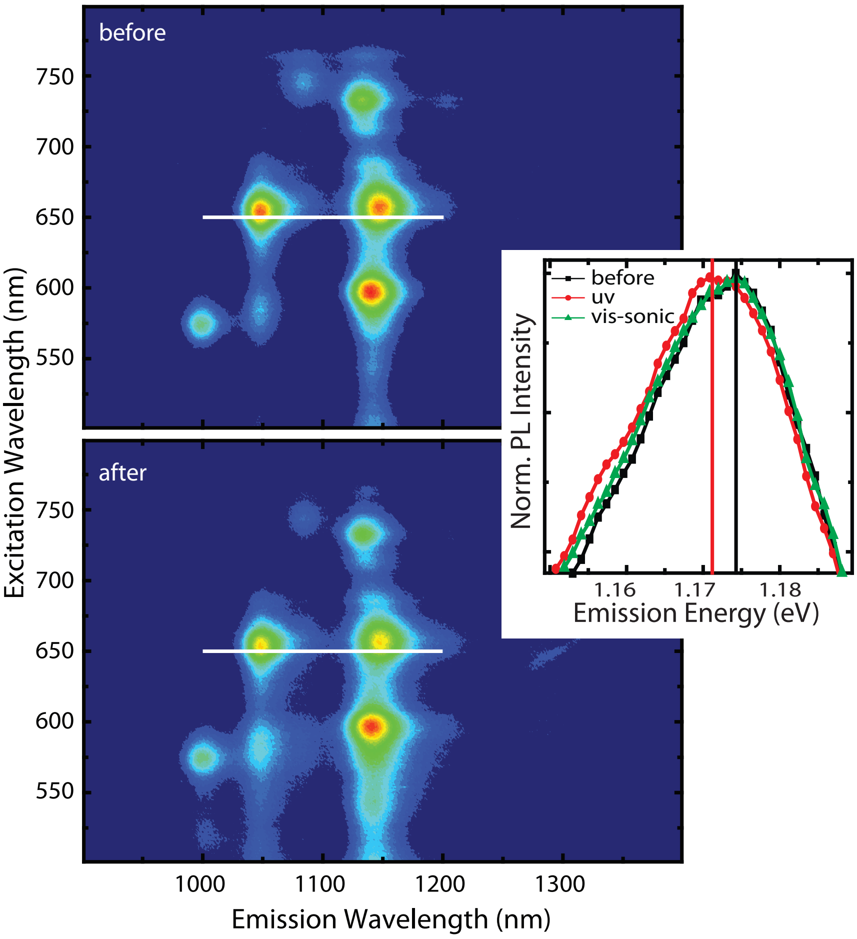

Figure 5.12. Photo luminescence excitation maps of HiPCO nanotubes solubilized in water using alkAZO. The top map shows the sample after preparation, while the bottom map was taken after several isomerization cycles. Both maps are in the same intensity range. As can be seen, even after different isomerization cycles the PL signal remains almost identical. The inset shows The luminescence of the (7,5) tube irradiated at 650 nm before isomerization, after UV irradiation and after visible back isomerization followed by sonication treatment. As can be seen, after UV irradiation, the peak position is red shifted by about 3 meV. The back isomerization treatment shifts the peak back to its original position.

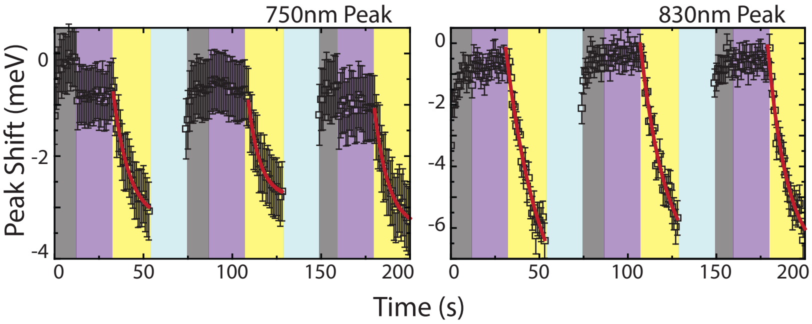

Figure 5.13. Shifts of the nanotube absorption peaks at 750 nm and 830 nm monitored over three isomerization cycles. As can be seen, the 750 nm peak shifts about 5 meV, while the 830 nm peak exhibits a shift of almost 8 meV. Note that in these measurements saturation was not reached.

decreases. This can be attributed to the tenfold higher critical micelle concentration of the *cis* compound. Micelles break up and the nanotubes are set free, allowed to re-bundle and precipitate. Visible light irradiation, however does not reverse this process, although it still induces back isomerization to the trans form. Moreover, the nanotube concentration sill decreases further. This is due to the micelles not forming around the tubes, but besides them. Further, the compound is unable to individualize nanotubes without the help of sonication.

To revert the system back to its original state, following the visible irradiation, mild sonication (here, a sonic bath with much less power than used for the preparation process) needs to be applied. UV/Vis irradiation can then been used to induce precipitation again, and so forth.

PLE maps of the sample were taken before and after several isomerization cycles (see Fig. 5.12). Both maps confirm successful individualization of nanotubes. It can be seen that even after several cycles, the PL signals are almost identical and no intensity is lost, assuring the purity of the tubes' quantum properties is preserved. The inset of Fig. 5.12 shows PL spectra of the (7,5) tube irradiated at 650nm. After UV irradiation, a mild red shift of about 3 meV can be observed. Visible irradiation followed by sonication leads the peak to shift back to its origin position.

The red shift in the PL position can most likely be attributed to a change in the dielectric environment due to the density of molecules on tube surface. It may also be related to the re-bundling of nanotubes, although here only very small bundles can actually contribute to the PL signal.

However, the discovery of the PL red shift lead to an investigation of the peak positions in the absorption spectra. In contrast to photo luminescence excitation experiments, absorption measurements cannot resolve single tube species, as for example the (7,5) and (7,6) tubes $E_{22}$ transitions are at very similar energies. Observing the distinct shift of one chirality is not expected, but a trend like a systematic red shift due to bundling effects might be seen.

Figure 5.13 shows the energy shifts for the most distinct absorption peaks located at 750 nm and 850 nm. It can be seen that during the time the sample is left in darkness, while it thermalizes after the sonication treatment, a slight blue shift can be observed. During UV irradiation the peak position remains the same. Visible irradiation, then, leads to a significant red shift of about 4 meV in the case of the 750 nm peak and about 6 meV in the case of the 850 nm peak.

## 5.4. Summary

Stable suspensions of carbon nanotubes in water were obtained using alkAZO. After functionalization, the azobenzene compound retained its switching properties. Reversible light driven isomerization to the *cis* state, as well as thermal back isomerization to the *trans* state was monitored using absorption measurements. From the nanotube absorption, we were able to show a decrease in the sample density upon switching to the *cis* state. This was attributed to the large differences in the CMC of the *trans* and *cis* compound, resulting in a breaking of the micelles upon turning to the *cis* form and subsequent release, re-bundling, and precipitation of the tubes. Mediated by sonication, the tubes were re-dispersed, restoring the samples original tube density. This process was repeatable for several cycles. Photo luminescence experiments were conducted to confirm that even after three cycles, the tubes were still individually suspended. Lastly, during the isomerization process, a shift in the nanotube peak positions in the range of a few meV was observed.

# 6 | Dipole Switch Functionalization of CNTs

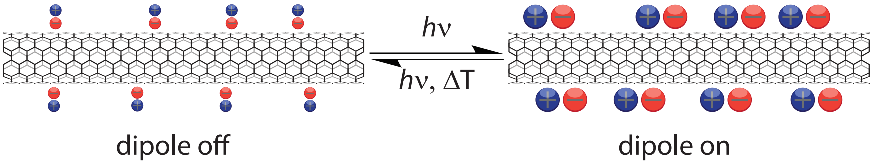

Figure 6.1. Sketch of a dipole switch functionalized nanotube. Triggering isomerization, the complex can be transferred between an *on* and *off* state. In the *off* state, the dipole moments in the vicinity of the tubes are relatively small, only minimaly influencing the tube's optoelectronic properties. In the *on* state, on the other hand, the dipole moments are large and, thus, is the influence on the tube.

As discussed before (see Chapter 1), the optoelectronic properties of carbon nanotubes are highly sensitive to the tubes' dielectric environment. Molecular switches, changing their dipole moment upon isomerization were proposed as a way of tailoring the properties of SWCNTs by providing a way of optically tuning an electric field in the tubes' immediate vicinity (see Fig. 6.1). This chapter describes non covalently functionalized SWCNTs, using spiropyran/merocyanine (SP/MC). The switches are adsorbed using a pyrene anchor group. In the **first section**, the spiropyran molecule is described and an overview of the literature concerning dipole functionalization of nanotubes is given. **Section two** explains the sample preparation process. In **section three**, our groups previous work on pyrene-spiropyran switch compounds is recapitulated [67, 78]. **Section four** details nanotube functionalization with a switch compound having a smaller pyrene-spiropyran spacing and in **section five**, the influence of the tube-switch separation distance is investigated [79, 80].

## 6.1. Spiropyran

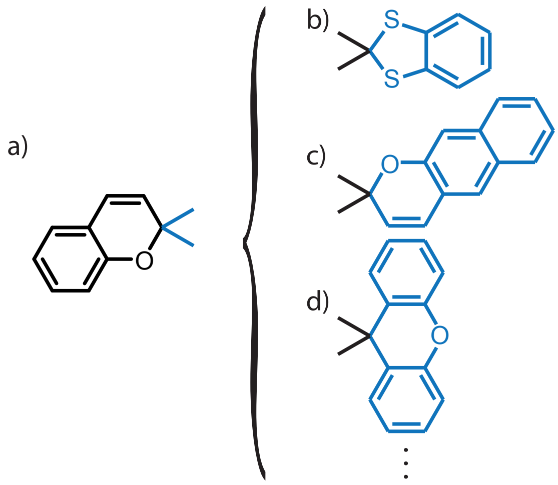

Figure 6.2. Structural build up of spiropyran molecules. Common element of all spiropyrans is a benzopyran moiety (a). The blue bonds denote the adjacent part of the spiropyran molecule, consisting for example of benzodithiole (b), naphtopyran (c) or xanthene (d).

Spiropyrans are a group of molecules, consisting two hetero cyclic parts, bound by a $sp^3$ carbon atom [81]. The two parts of the molecules are, thus, oriented perpendicular to each other. The common part in all spiropyran moieties is a benzopyran (see Fig. 6.2a), for the other half, a variety of structures has been exploited (see Fig. 6.2c-e for some examples). The spiropyrans used in the present work have an indoline group connected to the benzopyran part (see Fig. 6.3) and will here forth be referenced to simply as spiropyran (SP).

Under ambient conditions spiropyran is colorless, only exhibiting absorption features in the UV. Upon UV illumination, the molecule undergoes a ring opening reaction, allowing the molecule to isomerize into the merocyanine (MC) form. This results in a change of the hybridization, making the molecule planar, as well as drastically changing the absorption features. An absorption band rises in the visible region, consequently making the compound appear blue (see Fig. 6.4). Note that

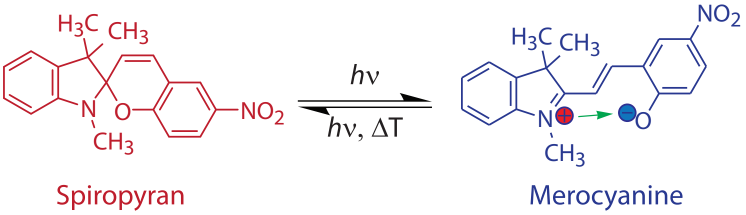

Figure 6.3. Structural build up of spiropyran molecules. Common element of all spiropyrans is a benzopyran moiety (a). The blue bonds denote the adjacent part of the spiropyran molecule, consisting for example of benzodithiole (b), naphtopyran (c) or xanthene (d).

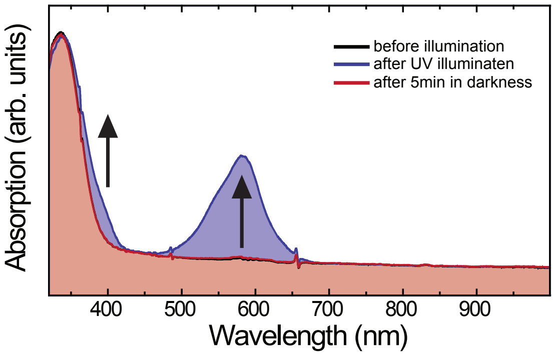

Figure 6.4. Absorption spectra of spiropyran in THF. At the beginning of the experiment, the only observed feature exists in the UV region. UV illumination leads to the rise of two bands located at ≈380 nm and ≈580 nm, resulting in a blue coloration of the solution. After switching off the light source, the spectra relax back to the original state.

this process is completely reversible. Back isomerization occurs thermally or by illumination with visible light. Figure 6.3 shows the structures of both, SP (left, red) and MC (right, blue). From the structures it can be seen that the ring opening reaction leads to a charge separation and, thus, dipole formation within the MC isomer of ≈14D [17] (green arrow in Fig. 6.3). The SP moiety also exhibits a dipole moment, however, much smaller than the MC form [17, 22].

Figure 6.4 shows the spectral change of the spiropyran molecule absorption upon UV irradiation (blue curve). When isomerizing to the MC form, two additional bands arise. A weaker band at ≈380 nm and a stronger absorption at ≈580 nm caused by the large de-localized $\pi$ orbital, only present in the planar MC isomer.

In this work, the 580 nm band will be referred to as the merocyanine absorption band.

### 6.1.1. Publication History

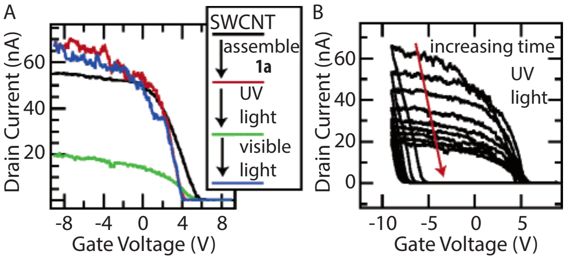

Figure 6.5. U-I characteristics of a CNT FET, functionalized with pyrene-spiropyran. Drain current and threshold voltage change upon switch deposition, as well as illumination, depending on the switch state (A). Irradiation was found to slowly alter the U-I characteristics as more and more SP molecules are converted into MC (B). (Adapted from Ref. [18]).

The drastic change of dipole moment upon isomerization from SP to MC has attracted the attention of the carbon nanotube community. Depending of the switching state, SP/MC switches placed in the vicinity of the nanotube were expected to differently manipulate the optoelectronic properties of carbon nanotubes. Thus, UV irradiation was proposed as a way of nanotube manipulation.
In 2004, the group of Haddon investigates SP/SWCNT complexes formed by covalently grafting SP onto SWCNTs nanotubes [19]. The spiropyran was linked to the tubes through the nitrogen atom of the indoline moiety, thus, resulting in the MC dipole moment being oriented parallel to the nanotube surface. They showed that through isomerization, they were able to reversibly change the nanotubes' $E_{11}$ intensity in semiconducting nanotubes. Other works describing spiropyran covalently attached to nanotubes used larger distance, thus reducing interaction [20], or utilized SP/CNT complexes for ion trapping [82] or to switch protein activity [83]. The group of Nuckols deposited spiropyrans non covalently onto single nanotube field effect transistors (FET). Using UV and visible light to induce isomerization, it was possible to tune the device's U-I characteristics, changing drain current as well as shifting the threshold voltage [18] (see Fig. 6.5). Isomerization was almost

completely reversible, making the FET susceptible to irradiation with certain wavelengths, enabling color detection.

Of the previous experimental attempts, however, none has provided evidence of effective coating of pristine, unperturbed nanotubes with spiropyran derivatives. As a matter of fact, no IR emission - experimental signature of the preservation of the SWCNTs pristine quantum properties - has been reported. Our approach offers the advantage of a scalable functionalization scheme for large quantities of nanotubes simultaneously, preserving their 1D quantum nature. At the same time it is allowing control over the tubes' optoelectronic properties by inducing light triggered, reversible changes to their dielectric environment.

## 6.2. Sample Preparation

Carbon nanotubes were dispersed in THF at a concentration of 0.01 G/L. Pyrene spiropyran derivatives were added at a total concentration of 5 $\mu$Mol/L and the samples were sonicated while in a water bath for one hour at $\approx 20$ W, using 500 ms pulses. Subsequently, centrifugation at 3500 g was applied for one hour, followed by another 30 min of sonication at the same parameters.

## 6.3. Pyrene-Spiropyran Functionalization

### 6.3.1. Free Pyrene-Spiropyran Dyad

The pyrene-spiropyran (pyrSP) dyad consists of two components, anchor and switch moiety. Pyrene-1-butyric acid is used as the anchoring moiety, while the switching part switch is 1-(2-hydroxyethyl)-3,3-dimethyl-6'-nitroindolspirobenzopyran, commonly called spiropyran. A detailed description of the synthesis can be found in Ref. [79].

Figure 6.7 shows the absorption spectra of the free dyad solubilized in THF. The spectra consist of the well separated features of the individual compounds indicating little interaction between the two parts, at this spatial separation. Before UV irradiation (purple spectrum), the only features that can be observed are the bands in the ultraviolet region, characteristic for the pyrene absorption. Upon irradiation

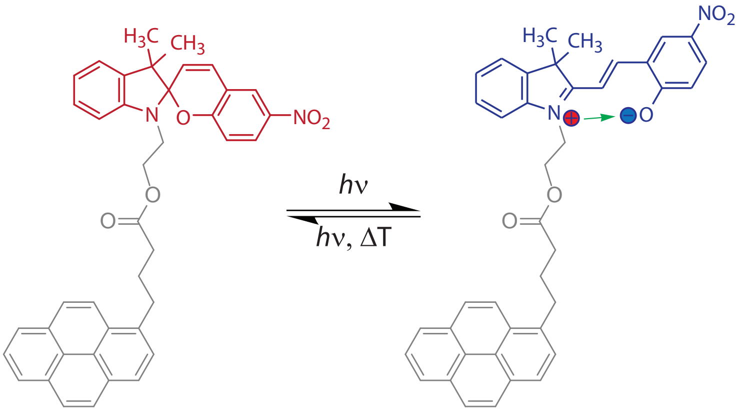

Figure 6.6. Structures of pyrene-spiropyran in the closed ring form (left) and the open ring form called merocyanine (right). While spiropyran exhibits a small dipole moment (≈7 D) perpendicular to its axis, merocyanine possesses a much larger dipole moment (≈14 D), due to charge separation along the axis (green arrow).

with a 366 nm light source, the pyrSP undergoes a ring opening transition and transforms into pyrene-merocyanine (pyrMC, blue spectrum). This leads to the rise of two characteristic merocyanine absorption bands at ≈370 nm and ≈570 nm, resulting in change in the color of the suspension from transparent to blue. Back isomerization to the original state occurs thermally or via irradiation with visible light into the 570 nm absorption band.

### 6.3.2. Investigation of the Pyrene-Spiropyran Functionalized Tubes

After adsorption of the pyrSP onto carbon nanotubes and subsequent formation of the tube-dyad complexes, UV-Vis absorption spectra reveal the characteristic nanotube $S_{22}$ features (see Fig. 6.8). After irradiation with UV light (366 nm), the rise of the 570 nm merocyanine band can be observed. Monitoring the merocyanine absorption over several cycles reveals that the isomerization process still seems to be fully reversible (see Fig. 6.8, inset). Figure 6.9 shows the kinetic behavious in the absence and presence of the tubes, respectively. Is can be seen, that the nanotubes do not significantly change the isomerization behavior.

Figure 6.10 shows a PLE map of the pyrSP covered nanotubes suspended in THF,

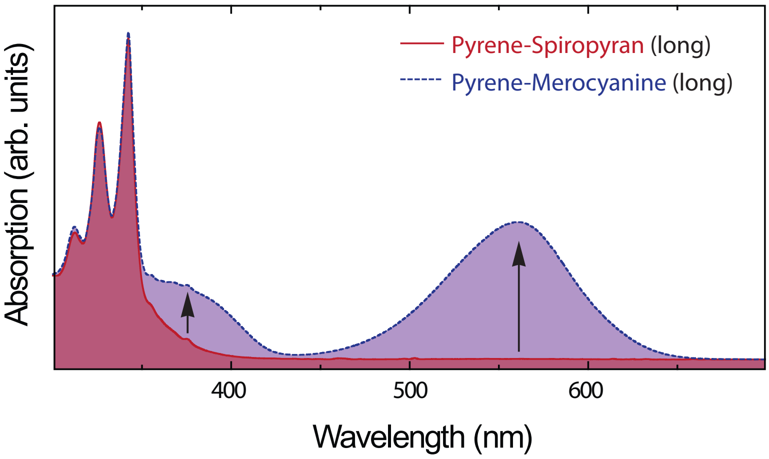

Figure 6.7. Absorption spectra of pyrene-spiropyran in THF before (red line) and after UV irradiation (dotted blue line). After isomerization from the closed ring spiropyran form to the open ring merocyanine form, peaks at 375 nm and 580 nm appear. [79]

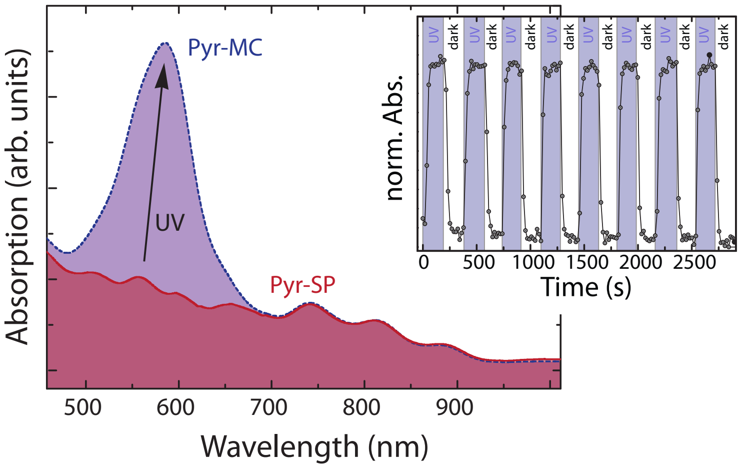

Figure 6.8. Absorption spectra of carbon nanotubes in THF after successful functionalization with pyrene-spiropyran (red line). Upon UV irradiation (366 nm), the 580 nm merocyanine absorption band can be observed. In the UV region, the characteristic pyrene peaks can be observed.

thus confirming the preservation of the tubes' pristine one dimensional quantum properties. This experiment was the first example of successful solubilization and isolation of carbon nanotubes using non covalently attached molecular dipole switches preserving tube luminescence reported in literature [78]. Other experiments used

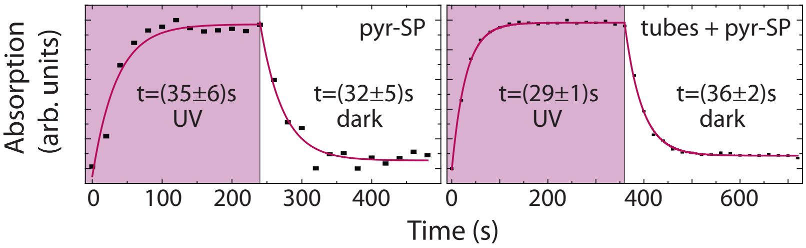

Figure 6.9. Isomerization behavior of pyrSP, both free and after adsorption. The area of the 570 nm merocyanine absorption peak was monitored. The data points where then fitted with an exponential decay function, the errors result from the fit. It can be seen, that within the error interval, the switch times are equal.

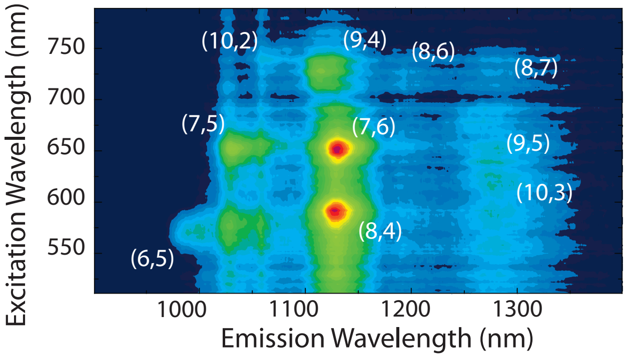

Figure 6.10. PLE map of pyrSP functionalized nanotubes. As in nanotube bundles, the presence of metallic tubes leads to quenching of the luminescence, this is proof of successful de-bundling. Carbon nanotubes are suspended in THF using only the spiropyran dyad to separate and stabilize them.

covalently attached spiropyranes, subsequently destroying the luminescence [19, 20] or only functionalized single tubes in specific nanoelectronic geometries [18].

As the kinetic switching process does not seem to be influenced by the presence of the tubes, it has to be clarified whether the switching moieties are placed at the tube surface or if there still are a large number of free compounds in the solution, not attached to the tubes. To this end, PL spectra can be used. The left part of Fig. 6.11 shows the emission of pyrene upon excitation at 340 nm from the free compound (dashed light blue line) and after nanotube functionalization (solid blue line). As can be seen, the emission from the adsorbed molecules is strongly suppressed, suggesting that all pyrene moieties are attached to the tubes, thus

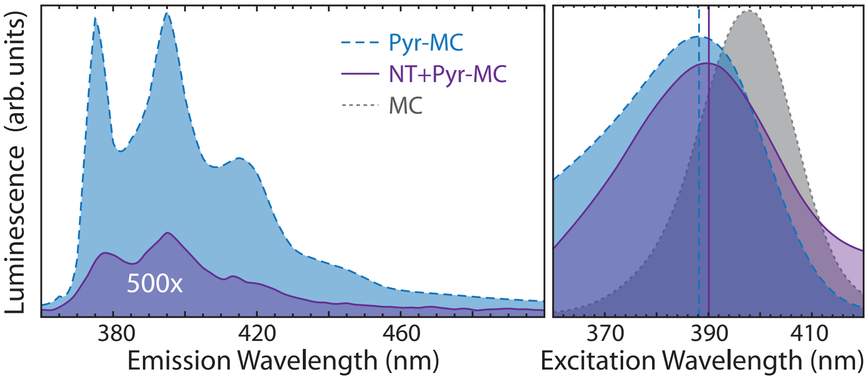

Figure 6.11. (left) Photo luminescence spectra of the pyrene moiety in free pyrene-merocyanine (blue, dashed) and pyrene-merocyanine adsorbed onto carbon nanotubes (purple, solid), excited at 340 nm. Note that after the adsorption, the signal is severely quenched and had to be up scaled by a factor of 500 to actually be visible. (right) Photo luminescence excitation spectra of free merocyanine (gray, dotted), free pyrene-merocyanine and adsorbed pyrene-merocyanine at 660 nm emission. As can be seen, the intensity is similar in all three cases, while the position shifts between all of them. Also it can be seen that, while the free MC exhibits a very symmetrical signal, this is not the case for the free pyrMC. After adsorption to carbon nanotubes, the signal regains a more symmetrical shape.

quenching its luminescence. However, monitoring the emission of the merocyanine moiety at 660 nm, similar intensities can be observed indicating comparable molecular concentrations in both cases (see Fig. 6.11, right).

Furthermore, the right part of Fig. 6.11 reveals a change in the symmetry of the merocyanine emission. While free merocyanine exhibits a relatively symmetrical photo luminescence signal (gray, dotted spectrum), the signal from the free pyrMC dyad is very asymmetrical, indicating an interaction between the two parts of the dyad. However, after functionalization, the peak takes a more symmetrical shape again, indicating a weakening of the interaction between the pyrene and merocyanine moieties, attributed to the tube-pyrene interaction, thus, also confirming adsorption.

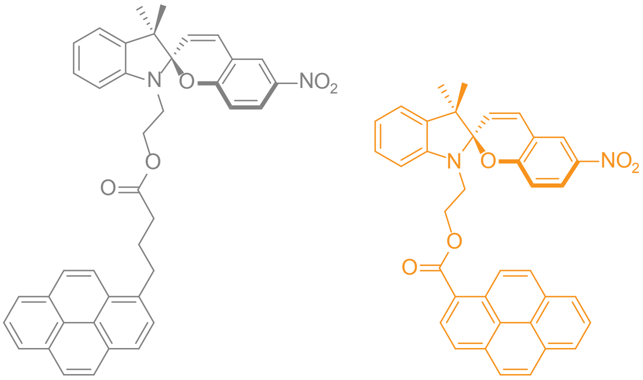

Figure 6.12. Structures of pyrene-spiropyran compounds. The short dyad (short pyrSP, orange) differs from the long pyrSP compound, used in the previous section (gray) in the length of the linker between pyrene and spiropyran moiety, i.e. the spacing between anchor and dipole.

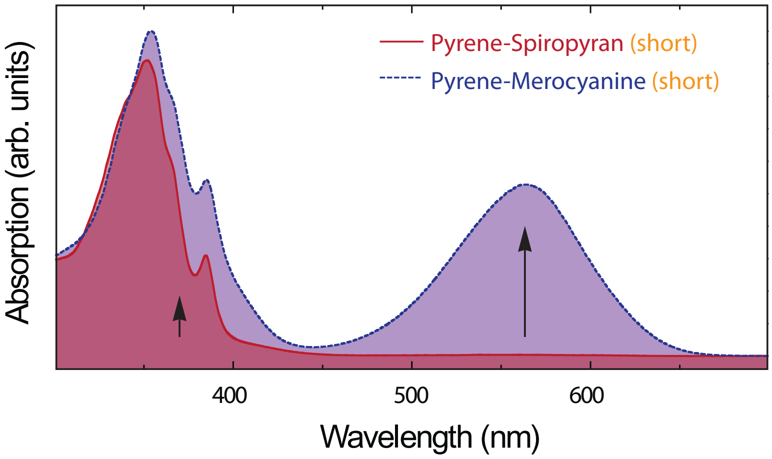

Figure 6.13. Absorption spectra of short-pyrene-spiropyran in THF before (red line) and after UV irradiation (dotted blue line). The spectra look very similar to the long linker compound, however, here the pyrene contribution is smeared out. [79]

## 6.4. Decreasing the Tube-Switch Separation

The interaction between nanotubes and dipoles is assumed to be of coulombic nature [22, 24, 26]. Thus, its magnitude strongly depends on the tube-dipole distance. The dyad used in the previous section had pyrene-spiropyran spacing of about 1 nm.

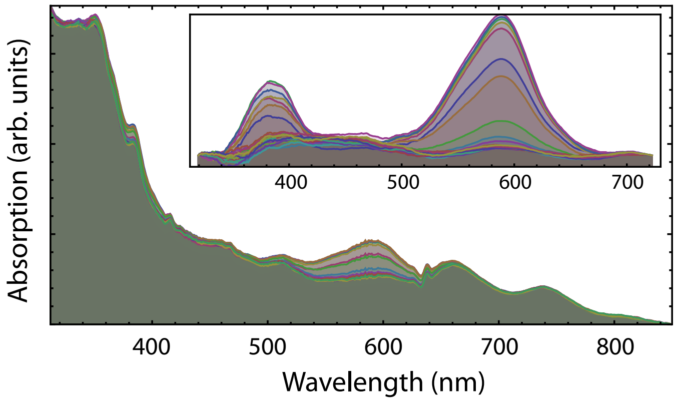

Figure 6.14. Absorption spectra of CoMoCAT nanotubes functionalized short-pyrSP in THF. Upon 366 nm UV irradiation, the rise of the 570 nm merocyanine band can be observed. The inset shows the change of the absorption spectra upon irradiation. Here, both merocyanine peaks can clearly be observed.

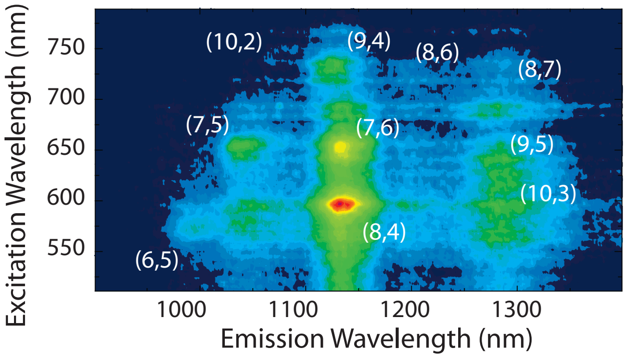

Figure 6.15. PLE map of pyrSP (short) functionalized nanotubes. Again, this is taken as proof of successful de-bundling, because the luminescence is no longer quenched by metallic tubes. Carbon nanotubes are suspended in THF using only the short spiropyran dyad to separate and stabilize them.

Using 1-pyrenecarboxylic acid instead of pyrenebutyric acid, pyrene-spiropyran dyads with a separation of only about 0.6 nm were created in an attempt to increase the tube-dipole interaction. Henceforth, the two dyads will be differentiated by the additions "long" (1 nm spacer) or "short" (0.6 nm spacer) to their name.

Looking at the absorption spectra of short pyrSP in THF (see Fig. 6.13), the features of anchor and switch can be identified similar to the long pyrSP compound. This time, the pyrene absorption is strongly broadened and not consisting of sharp features anymore. However, this is not due to the reduced anchor-switch distance, but an inherent attribute of pyrenecarboxylic acid [79]. UV irradiation (350nm), again leads to a rise in the merocyanine absorption features around 370 nm and 570 nm.

Figure 6.14 shows absorption spectra of short-pyrSP functionalized CoMoCAT nanotubes in THF. As with the long pyrSP compound, both, the dyad and the tubes' absorption features can be observed. UV irradiation still triggers the isomerization process, visible as an increase in the familiar merocyanine bands, which can be identified more clearly in the difference spectra, subtracting the spectra of the pre-irradiated tube-switch complexes (see Fig. 6.14, inset).

Successful de-bundling is investigated as before, by looking at the photo luminescence of the samples (see Fig. 6.15). Again, individual chiralities can clearly be identified, thus confirming stabilization of individual tubes within the sample.

## 6.5. Comparing both Spiropyran Dyads

### 6.5.1. Influence on the Nanotubes

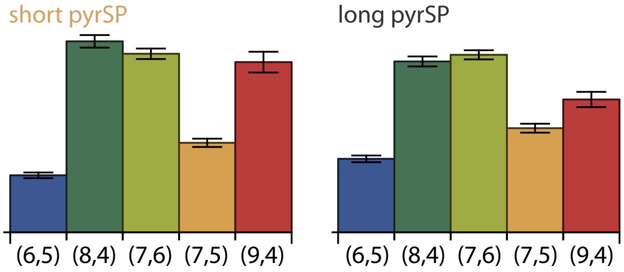

Figure 6.16. Relative chiral abundances of CoMoCAT tubes solubilized in THF using short-pyrSP (left) and long-pyrSP (right), taken from PLE measurements. Both samples exhibit very similar compositions.

Carbon nanotubes were de-bundled and suspended in THF using pyrSP dyads with spacer length of ≈0.6 nm and ≈1 nm. However, as the spacer length directly influences the tube-dipole distance, it is now interesting to compare the behavior of the two compounds, when in contact with carbon nanotubes, as well differences in both tube-switch complexes in general.

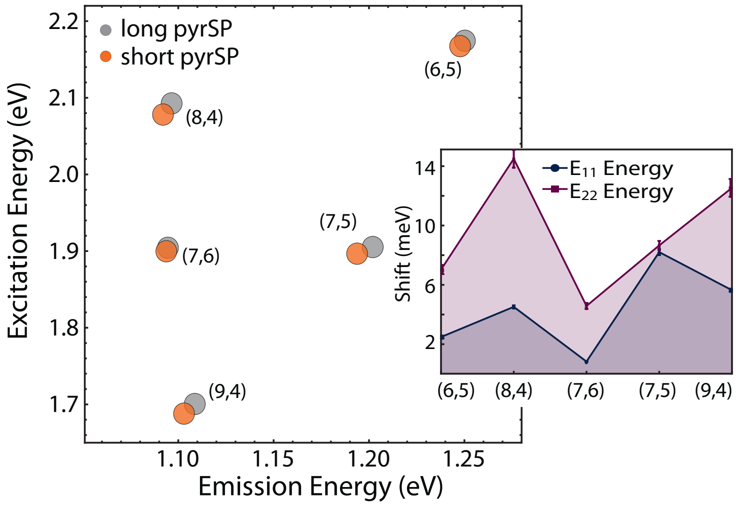

Figure 6.17. Pseudo PLE map of CoMoCAT nanotubes suspended with short- (orange circles) and long (gray circles) pyrSP. Peak positions were obtained from PLE measurements of both samples. The positions differ for all chiralities, however, the magnitude of the shifts vary. The inset shows the absolute peak shifts between the two samples. It ranges from 0 meV - 7 meV in the emission and 4 meV - 14 meV in the excitation.

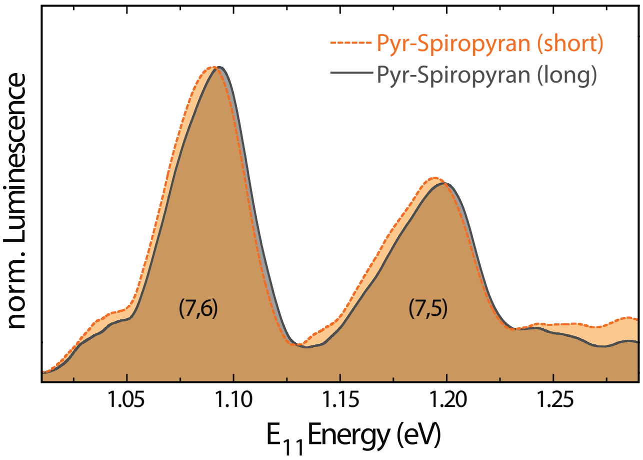

Figure 6.18. Photo luminescence spectra of carbon nanotubes functionalized with short- (orange, dotted) and long-pyrene-spiropyran (black). As can be seen, although the anchor group as well as the dipole moment of the compounds are similar, different $E_{11}$ transition energies can be observed.

First, the relative sample compositions are of interest. In both samples, the most abundant chiralities are the (7,6) and (8,4) tubes while all other species give very similar contributions (see Fig. 6.16). This nicely shows how similar the binding interaction between nanotubes and pyrSP dyads is. Based on the use of pyrene as an anchor group, both samples exhibit similar composition in the isolation and solubilization process. As it is known that changes in the anchoring moiety affect the sample composition, this was expected. However, it was also found that not only the immediate anchor group, but in some case also the directly adjacent moieties can influence a compounds selectivity (see Ref. [44] and chapter 4). Here, the spacer length and, thus, dipole distance, does not seem to induce significant changes in the selectivity.
Comparing the nanotube luminescence in both samples, the influence of the different tube-dipole separations becomes apparent. Figure 6.17 shows the peak positions in both samples as a pseudo PLE map. It reveals a shift in the $E_{11}$ and $E_{22}$ transition energies between the two samples that differs in magnitude, depending on the chirality in question. The inset of Fig. 6.17 shows the absolute shifts range from 0 meV - 7 meV in the emission and 4 meV - 14 meV in the excitation. This reveals that the influence of the dipoles on the tubes is strongly chirality dependent. Figure 6.18 exemplarily shows the PL spectra of both samples for an excitation at 650 nm.

### 6.5.2. Effect of the Isomerization Process

Interaction always needs at least two partners, thus, not only the nanotubes, but also the switches themselves are altered upon adsorption. And again, the different spacing comes into play. Up until now, only the influence of the spiropyran dyads on the nanotubes has been taken into account. Upon UV irradiation, spiropyran undergoes a ring opening transition and converts into the merocyanine form. Merocyanine is a planar molecule with an extended $\pi$-system that is expected to interact more strongly with the tubes. Thus, interaction between tubes and dyad is expected to alter upon irradiation and the intensity of this interaction should in principle depend on the relative distance.

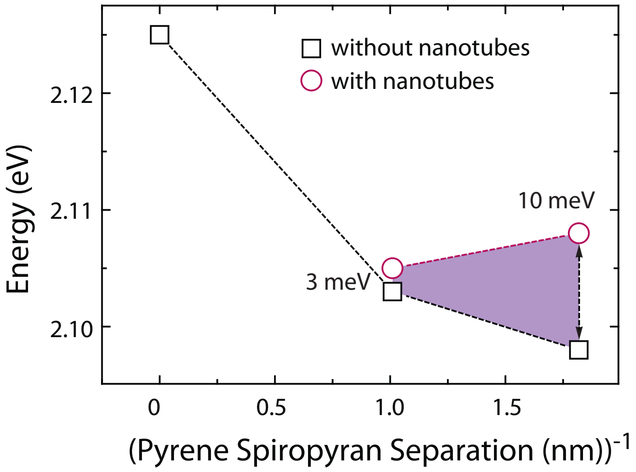

Figure 6.19. Merocyanine transition energy. Compared to free merocyanine, with decreasing pyrene-merocyanine separation, the peak shifts towards lower energies. However, upon adsorption to the nanotube surface, this red shift is partially countered. Hence, with decreasing pyrene-merocyanine separation, an increasing splitting in the positions of the free and adsorbed compounds can be found.

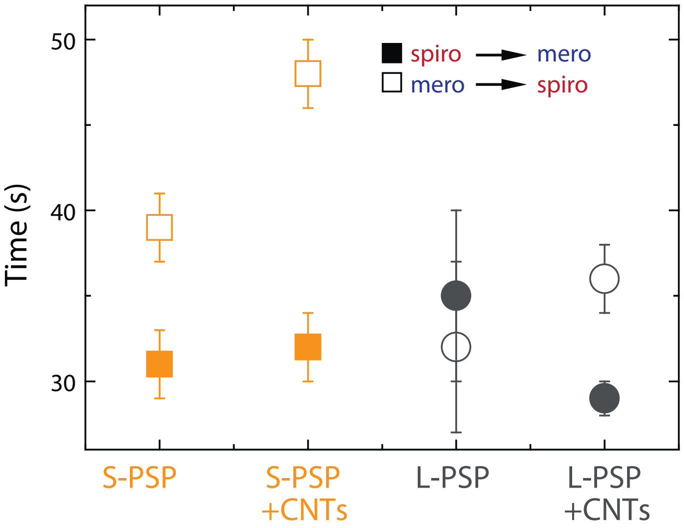

Figure 6.20. Ring opening and closing reaction times for free and adsorbed pyrene-spiropyran, both with short (orange) and long linkers (black). While almost all isomerization times are very similar, the merocyanine to spiropyran back isomerization of the adsorbed short compound is slowed down considerably compared to the free molecule.

When investigating the behavior of the switch molecules, two effects can be observed upon UV irradiation:

Firstly, the position of the 570 nm merocyanine changes depending on the pyrene-merocyanine distance. Considering pure spiropyran as a pyrene-spiropyran dyad with an infinitely long spacer in between, thus, neglecting any interaction between the two, one can monitor the change of the MC peak positions depending on the anchor-switch distance (see Fig. 6.19). With decreasing spacer length, a systematic red shift can be observed in the free compounds (black, dashed line). This shift is most likely attributed to an increase in interaction between merocyanine's and pyrene's $\pi$-systems. As both samples where created under equivalent conditions in THF, solvent effects can be ruled out.

Secondly, after complexation with carbon nanotubes, the red shift found for the free compounds gets partially reversed and the peak shifts back towards the original position of the unperturbed merocyanine compound. Most likely, this opposing effect is caused by the strong $\pi$-$\pi$ interaction between nanotubes and pyrene, leading to a lowered perturbation of the merocyanine $\pi$-system by the pyrene.

Interestingly, the tube-dipole separation not only affects the electronic properties of the switch molecule, resulting in a change in the spectral position of the MC absorption band, but also alters the kinetic behavior of the isomerization process (see Fig. 6.20). Before functionalization, the isomerization times for the two pyrSP compounds are very similar. After the adsorption to carbon nanotubes, however, a drastic change can be observed. The dyad with the long spacer seems to have a sufficiently large tube-switch distance to induce only little changes to its switching dynamics. The back isomerization time of the shorter molecule, on the other hand, is increased by roughly 25%. This can be attributed to a stabilizing effect of the nanotubes sidewalls on the planar merocyanine form at low distances due to enhanced $\pi$-$\pi$ interaction and is in agreement with reports of MC stabilization on gold (111) surfaces [84]. The effect on the photochemical ring opening isomerization, in contrast, is negligible within the experimental error. It has to be pointed out that all these effects are measured in an ensemble of nanotubes and molecules in suspension and not on the single-molecule level.

## 6.6. Summary

Carbon nanotubes were non covalently functionalized with pyrene spiropyran dyads of different spacer lengths. Both dyads contain similar anchor groups, resulting in similar chiral compositions of the dispersions. Photo luminescence experiments proved, that after functionalization the tubes retained their pristine 1D quantum properties. However, even though the sample composition is only affected by the morphology of the anchor, the different distance between anchor and dipole switch alter the positions of the peaks. A slight red shift in the range of up to 7 meV in the $E_{11}$ and 14 meV in the $E_{22}$ direction between the samples was observed, even in the SP form.

The merocyanine absorption bands were found to be sensitive to the distance to the pyrene and red shift with decreasing separation. After functionalization, this effect is partially screened, again dependent on the distance to the nanotube. At close proximity to the nanotube surface, the MC form was found to be significantly stabilized. This in agreement with other works, documenting the inhibition of MC to SP back isomerizability upon adsorption to a gold (111) surface [84]. The disadvantage of this experiment is that the optical readout of the nanotubes' opto-electronic properties simultaneously induces switching, thus making it impossible to compare the "on" and "off" state. Regarding this, further experiments like for example electronic transport measurements are needed.

# 7 | Micelle Swelling

In the previous chapters, the focus was on molecular agents able to attach to carbon nanotubes by themselves. The molecules were attached either using anchoring moieties for $\pi$-$\pi$-stacking (pyrene-spiropyran molecules) or by forming micelles around the tubes (in the case of the amphiphilic molecules, azobenzenes, etc.). However, to verify the theoretical predictions made for molecular dipole switches in the immediate vicinity of carbon nanotubes, a method is needed that allows to force the molecular very close to the tube. Further, we found that the presence of an aromatic anchor group seems to dampen the interaction between tube and switch and, thus, a functionalization method not relying on an anchor group is favorable. The micelle swelling approach [85, 86], can fulfill both these requirements while at the same time benefiting from the excellent solubilization and individualization capabilities known from commercially available soaps like SDS, SDBS and CTAB.

## 7.1. Concept

As with other amphiphiles, the CNTs are suspended in micelles in water (see Fig. 7.1a). However, the functionality, in this case, is not part of the amphiphile. Molecular agents (aromatic molecules, molecular switches, etc.) are solubilized in organic solvents like THF or DCM. These solutions are then added to the nanotube suspensions while stirring (and, depending on the solvent, heating) is applied. The amphiphiles form micelles between the water and any hydrophobic additive. Therefore, the organic solvents and the solubilized molecules will penetrate the nanotube micelles (see Fig. 7.1b). Over time, the organic solvents then slowly evaporate leaving the molecular agents in the micelles, close to the nanotubes (see

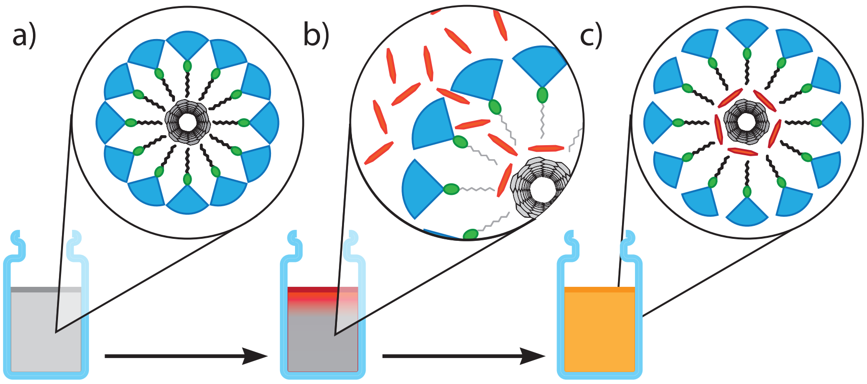

Figure 7.1. Schematic representation of the micelle swelling method: (a) CNTs are suspended in water using amphiphilic micelles. (b) After the addition of a solution of molecular agents in an organic solvent, the molecules (and organic solvent) begin penetrating the micelles. (c) Then, after some time, stirring and possibly heating, the organic solvent has evaporated and the molecules are now integrated in the micelles.

Fig. 7.1c).

Parameters for this technique include the amount of organic solvent added to the nanotube suspension. A too large quantity can change the environment so drastically, that the micelles actually break up instead of just bloating, leading to precipitation of the nanotubes. Another important parameter is the concentration of the molecules, as a too high concentration can lead to the nanotubes being pushed out of an overfilled micelle, while a too low concentration will not yield an observable effect on the tubes, at all.

## 7.2. Sample Preparation

For the micelle swelling approach, CNTs were dispersed in water using various soaps like SDS, CTAB (cetrimonium bromide) and SC (sodium cholate). Among the organic solvents we used were THF, Methanol (MeOH) and dichloromethane (DCM). Different starting concentration of SP, as well as volume ratios between water and the added organic solvents were investigated to find optimal parameters for the experiments. It is important, to use organic solvents with a boiling point below 100° C in order to allow them to evaporate without drying up the samples. We found that the best samples were obtained using THF, while DCM and MeOH still yield good results. Further, it was found that the water/THF volume ratio has to be kept relatively large (≈20) in order not to destroy the micellar structures and induce precipitation. The same was found for too high concentrations of SP/MC. The last important parameter was the irradiation and stirring time. While an extended stirring time is needed in order to let the THF evaporate, too long UV irradiation, as well as a too close distance to the source (too high intensity) could lead to photobleaching. Thus, UV irradiation should only be applied for a few hours and then switched off, while the stirring continues. Evaporation could in principle be accelerated by heating, however, it might lead to back isomerization of the MC to the closed ring form.

The samples used in this chapter were prepared as follows:

CoMoCAT nanotubes were dispersed in water at a concentration of 0.1 g/L with 1 wt% of SDS. The samples were sonicated for one hour at ≈20 W, followed by centrifugation for one hour at 27° C and 31 000 g. To 3 mL of nanotube suspension, 150 $\mu$L of THF containing 0, 50, 100 and 150 $\mu$g of spiropyran molecules were added while stirring over an extended time of 48 hours. After the swelling procedure, the samples were centrifuged again for 10 minutes to precipitate any bundles that might have formed during the swelling process, as well as nanotubes that are no longer encapsulated. During the stirring process, half of the samples were covered in aluminum foil to prevent light exposure, while the other samples where UV irradiated using a 366 nm source. It is important to note that in the case of the UV irradiated samples, the SP in THF solution was pre irradiated before adding it to the tube suspension. This way, half of the samples were functionalized with spiropyran, while the other half of the samples were functionalized with merocyanine.

In the following chapter, the SDS suspended nanotubes that underwent the swelling procedure in darkness with just THF without SP/MC will be referred to as the **pure sample**, while samples containing a SP concentration of X $\mu$Mol/L will be named **darkX** or **uvX** depending on whether they were prepared in darkness or under illumination. Further, samples produced in darkness will be referred to as "dark samples"), while samples prepared under UV irradiation will be referred to as "UV samples". Also, in the case of the dark samples, the added switch molecule

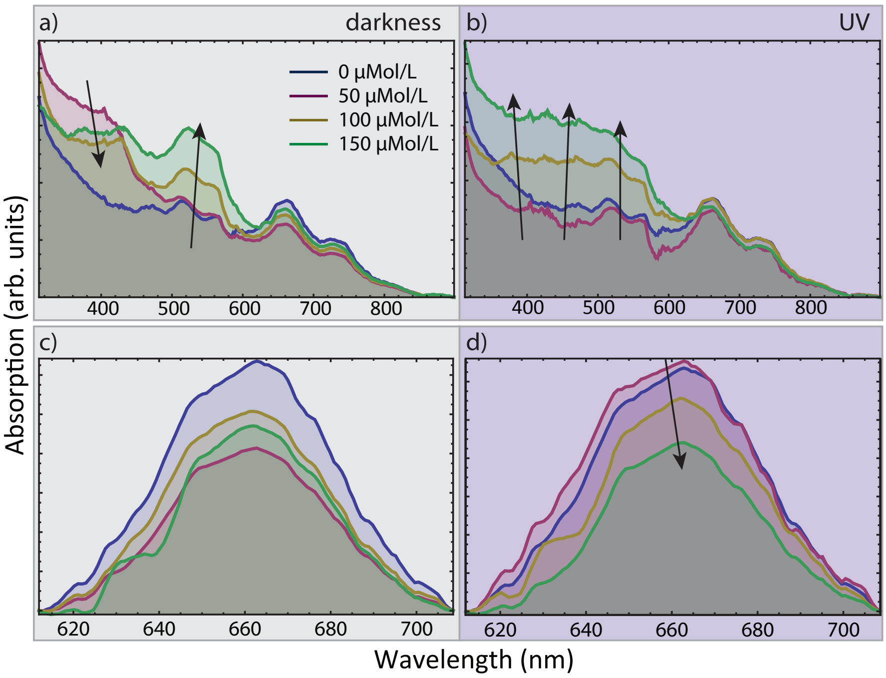

Figure 7.2. Absorption measurements of micelle swelling samples made with SDS and THF. (a), (b) Spectra of samples made in darkness and under UV irradiation, respectively. As can be seen, with increasing SP/MC concentration, the typical merocyanine peaks around 550 nm arises similarly in all samples. The 390 nm transition, however, shows opposite behavior the dark and UV samples. While in the dark samples the absorption decreases with increased switch concentration, in the UV samples the peak rises. Further, the UV samples exhibit a third contribution at 450 nm, blending together the 390 nm and 550 nm peaks. This band is usually contributed to stacked merocyanine. (c) and (d) Absorption at 650 nm ((7,5) and (7,6) tube) after linear background subtraction for dark and UV samples, respectively.

will be referred to as spiropyran (SP), while in the case of the UV samples it will be called merocyanine (MC) as these are the respective configurations, the molecule was in at the moment of the addition. It has to be noted that UV irradiation of the samples after the preparation procedure does not induce further switching.

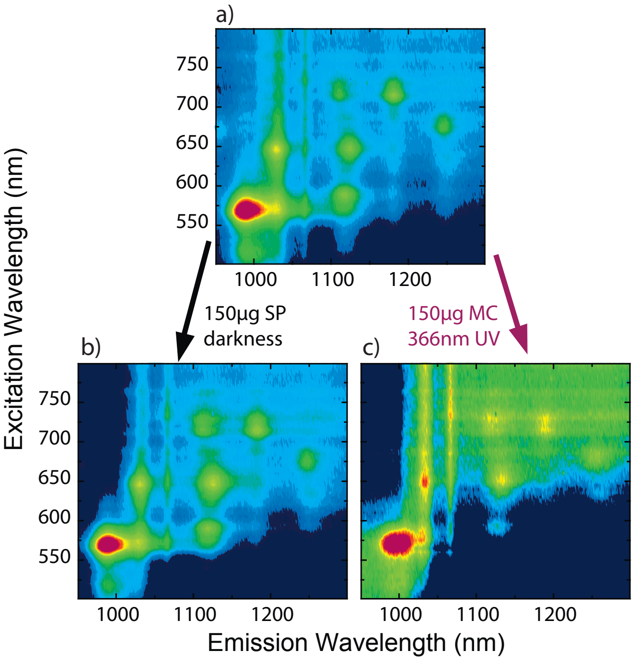

Figure 7.3. PLE maps of CoMoCAT tubes in water suspended with SDS (a), after the addition of 150 $\mu$L of SP in darkness (b) and under UV irradiation with 366 nm (c). As can be seen, spectra (a) and (b) look very similar. However, in the UV irradiated sample, the intensity is much weaker, leading to noise and background being more pronounced.

## 7.3. Results

The starting material for these experiments are SDS suspended CoMoCAT tubes in water. SDS has been widely used to encapsulate and isolate carbon nanotubes in water and is known to yield samples of large tube density and strong luminescence. As can be seen in the PLE map of the pure sample (Fig. 7.3a), it contains a wide range of different nanotube peaks. Thus, the influence of the spiropyran addition to the pure sample can be investigated on several different chiralities simultaneously. Absorption measurements of the micelle swelling compounds exhibit the features known for case of free MC in THF (see Fig. 7.2a, b). The characteristic merocyanine bands can be observed at 390 nm and 550 nm in the dark as well as the UV sample. In the UV samples, an additional peak at 400 nm can be observed. In other experiments, this peak has been attributed to stacked merocyanine [19]. Note that here, strong MC absorption features are observed even in the samples prepared in

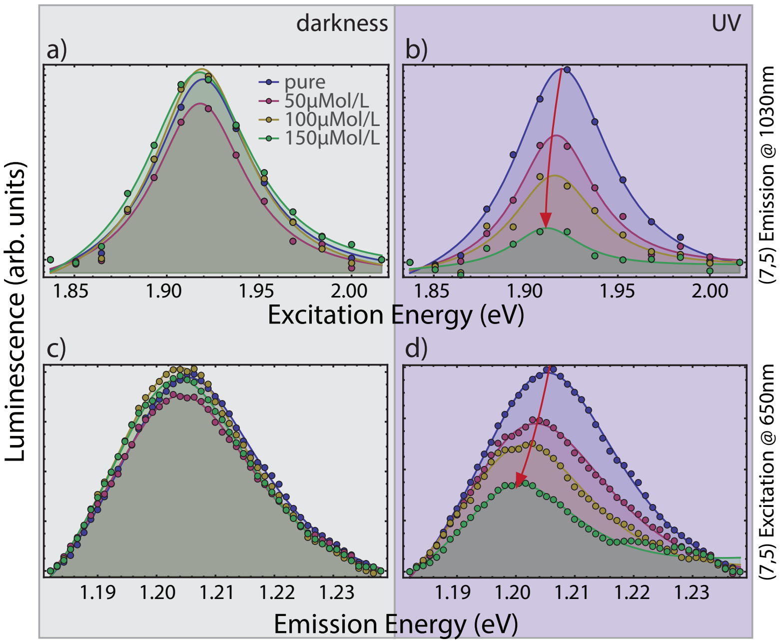

Figure 7.4. Photo luminescence spectra of the (7,5) tube in the micelle swelling samples. (a,b) PLE spectra at fixed 1030 nm (1.204 eV) emission wavelength of the samples prepared in darkness (a) and under UV illumination (c). While the samples prepared in darkness exhibit very similar intensities, as well as peak positions, the UV illuminated samples show a striking red shift, as well as decreasing luminescence intensity with increased spiropyran concentration. (b,d) PL spectra at fixed 650 nm (1.908 eV) excitation wavelength of dark (b) and UV irradiated samples (d). Again, the dark samples show very similar spectra, while the UV samples exhibit strong changes in the peak position and intensity when increasing the spiropyran concentration.

darkness, supposedly mainly containing the ring closed SP form of the switch.

As the SP/MC molecules are brought into a highly complex environment consisting - at the time of preparation - of carbon nanotubes, water and THF, stirring and (in the case of the UV samples) a light field, it is hard to predict the molecules' behavior. An explanation for the unexpected absorption behavior, however, must take this complex environment into account makeing a numerical interpretation highly cost intensive. Water is a polar solvent, further, the SP/MC molecules are trapped at the tubes-SDS interface. Thus, even in darkness, a large amount spiropyran might be converted into merocyanine during the preparation process. The reason why dark and UV samples still exhibit different absorption characteristics might then

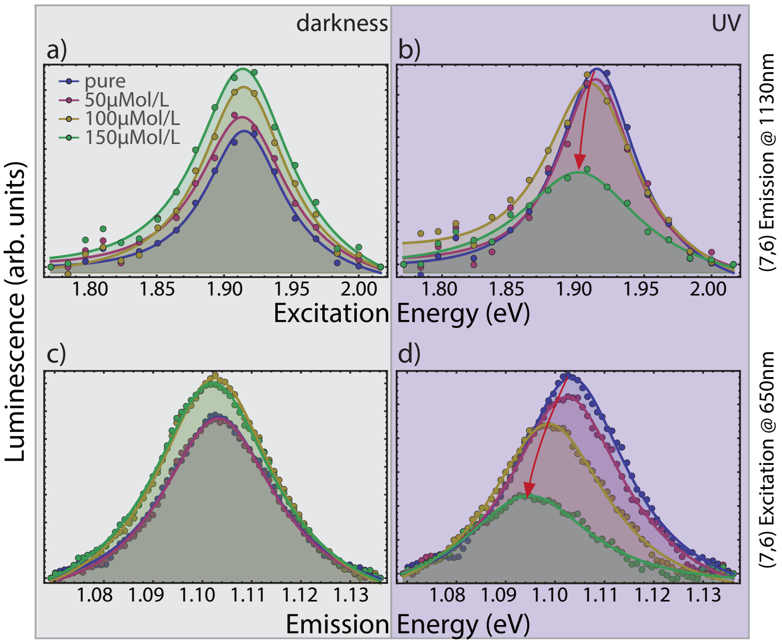

Figure 7.5. Photo luminescence spectra of the (7,6) tube in the micelle swelling samples. (a,b) PLE spectra at fixed 1130 nm (1.097 eV) emission wavelength of the samples prepared in darkness (a) and under UV illumination (c). While the samples prepared in darkness exhibit very similar intensities, as well as peak positions, the UV illuminated samples show a striking red shift, as well as decreasing luminescence intensity with increased spiropyran concentration. (b,d) PL spectra at fixed 650 nm (1.908 eV) excitation wavelength of dark (b) and UV irradiated samples (d). Again, the dark samples show very similar spectra, while the UV samples exhibit strong changes in the peak position and intensity when increasing the spiropyran concentration.

be explained by the starting conditions leading to different molecular assemblies within the micelles. As the UV samples were made with the switches predominantly being in the MC form at the beginning, this could subsequently result in increased MC stacking for the UV samples compared to the dark compounds. Stacked merocyanine, depending on the respective orientations will most likely interact differently than pure merocyanine, thus in principle different MC compounds are present. It is also possible that within the micellar structure, an intermediate state is somehow stabilized leading to different tube-switch interactions. However, this is only speculation and further experimental and theoretical investigations are needed to tackle this issue.

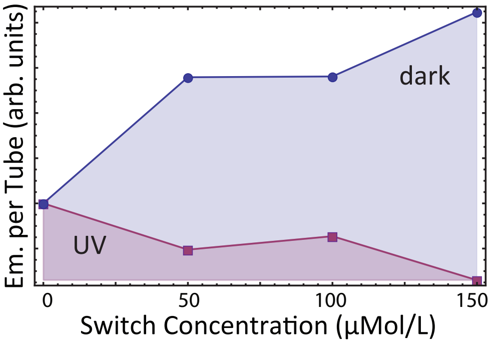

Figure 7.6. Average luminescence per tube upon excitation at 650 nm calculated by the areas of the luminescence and absorption peaks after linear background removal. Interestingly, while in the case of the UV samples, the average luminescence decreases, in the dark samples an increase is observed.

After the micelle swelling procedure, it can immediately be observed that the PL spectra drastically change, depending on whether they were prepared under UV irradiation or in darkness. Comparing the PLE map of the samples containing the highest SP concentrations (150 $\mu$Mol/L), **dark150** and **uv150** in Fig. 7.3b and c, respectively, it can be seen, the **dark150** sample looks very similar to the pure sample, while the **uv150** sample exhibits large differences. As can be seen from the PLE cross sections of the (7,5) and (7,6) tubes (see for example Fig. 7.4d and 7.5d), this is due to a strong, concentration dependent, decrease in luminescence intensity.

Figures 7.4a-d show the PLE spectra for different SP concentrations at fixed emission wavelength of 1030 nm (≈1.2 eV) and excitation wavelength of 650 nm (≈1.9 eV), respectively. Comparing the luminescence of the dark samples, to the pure compound, the spectra corresponding to the dark samples on first glance exhibit only little effect of the SP addition (see Fig. 7.4a, c). However, in the UV samples this is no longer true (see Fig. 7.4b, d). The most striking effect is the strong decrease in luminescence intensity with increasing MC concentration. This can be due to two reasons. First of all, the addition of the strong MC dipoles could lead to a destabilization of the micelles and a loss of tubes or for example re-bundling. Secondly, the planar MC compounds attached to the tube surface might in fact quench the tubes luminescence.

The first case could in principle be confirmed by comparing the nanotube absorption

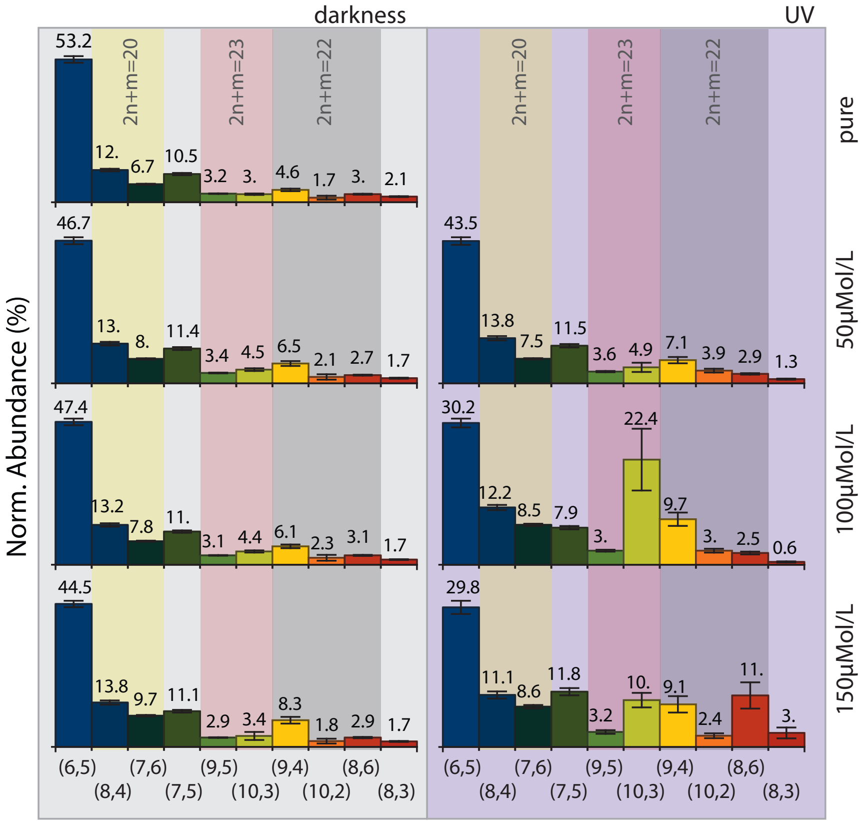

Figure 7.7. Chiral compositions of micelle swelling samples using SDS suspended tubes and spiropyran in THF. The tube abundances were taken from the samples' PLE maps. As can be seen, while the samples prepared in darkness all show very similar compositions, independent of the SP concentration, this is not the case for the UV irradiated samples. With increasing MC concentration, sample composition drastically changes, leading, for example, to a relative decrease of the (6,5) tube contribution. To understand whether this effect depends on the laola families, tubes belonging to the same 2n+m laola are marked. It can be seen that for example the **22** tubes react differently to the merocyanine coverage, as the (9,4) and (8,6) tubes contributions increase while the (10,2) tube is almost not affected at all.

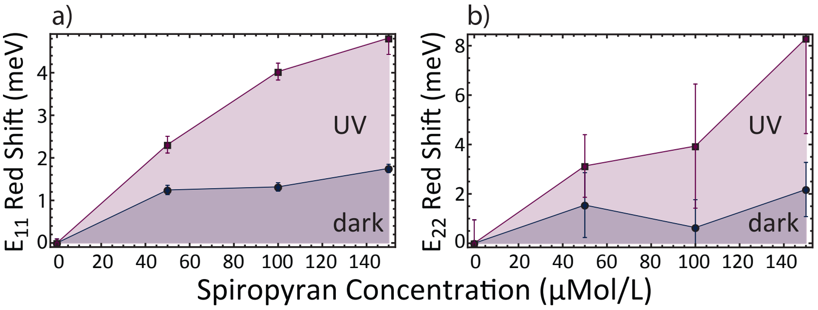

Figure 7.8. Changes of the (7,5) tubes $E_{11}$ and $E_{22}$ transition energies for samples prepared both, in darkness and under UV illumination, with increasing spiropyran concentration. (a) Red shift of the (7,5) peak emission energy ($E_{11}$ transition). For spiropyran functionalized samples (prepared in darkness), a shift of ≈1.5 meV can be found for a spiropyran concentration of 150 $\mu$Mol/L, and ≈5 meV can be found for a merocyanine concentration of 150 $\mu$Mol/L. (b) Red shift of the (7,5) peak excitation energy ($E_{22}$ transition). Here, the spiropyran functionalized tubes show a similar red shift as before (≈2 meV, 150 $\mu$Mol/L), while the merocyanine covered tubes red shift is about 1.6 times larger then in the $E_{11}$ direction (≈8 meV, 150 $\mu$Mol/L).

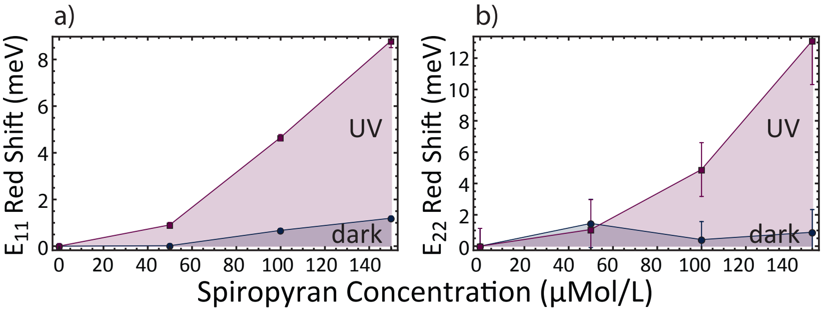

Figure 7.9. Changes of the (7,6) tubes $E_{11}$ and $E_{22}$ transition energies for samples prepared both, in darkness and under UV illumination, with increasing spiropyran concentration. (a) Red shift of the (7,6) peak emission energy ($E_{11}$ transition). For spiropyran functionalized samples (prepared in darkness), a shift of ≈1.5 meV can be found for a spiropyran concentration of 150 $\mu$Mol/L, and ≈9 meV can be found for a merocyanine concentration of 150 $\mu$Mol/L. (b) Red shift of the (7,6) peak excitation energy ($E_{22}$ transition). Here, the spiropyran functionalized tubes show a similar red shift as before (≈1.5 meV, 150 $\mu$Mol/L), while the merocyanine covered tubes red shift is about 1.5 times larger then in the $E_{11}$ direction (≈13 meV, 150 $\mu$Mol/L).

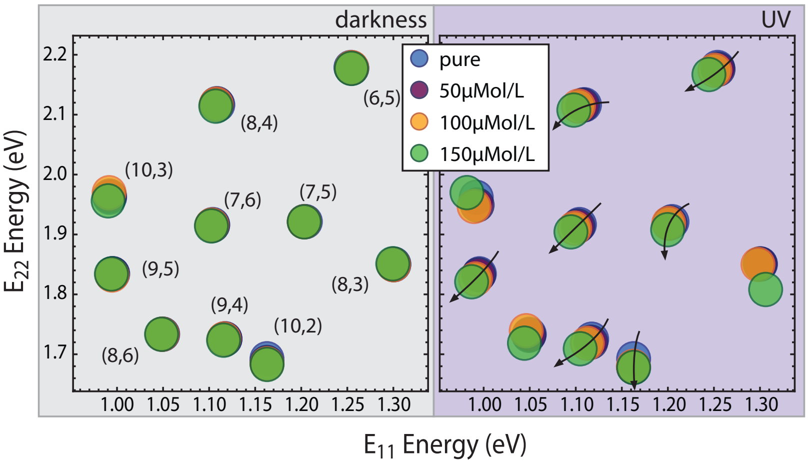

Figure 7.10. Pseudo PLE maps of the micelle swelling samples prepared in darkness (left) and under UV illumination (right). As can be seen, even with increasing spiropyran concentration, the shifts in the transition energies of the darkness samples are hardly observable. The UV samples, however exhibit strongly noticeable changes in the transition energies. Moreover, it can be seen that these shifts are not uniformly. When visualizing the peak shifts as curves, some are found to be concave, while others are convex, meaning that different chiralities interact with the switches in a different manner.

peaks, while the second case is harder to tackle as, if the tubes' luminescence is quenched by the MC, the question arises what the exact mechanisms are. Nanotubes mainly luminescence in the infrared, so no spectral overlap between the tubes' and MC's ground states exist. Therefore, effects like Förster transfer can be ruled out. This is supported by the fact that exciting the molecule does not lead to nanotube luminescence. Thus, the opening of non radiative de-excitation channels within the tube-switch complexes might be an explanation for the diminishing luminescence. The idea that luminescence is quenched is, however, supported by Fig. 7.6, depicting the average luminescence per tube. While the average luminescence actually rises after SP addition (dark samples), it is quenched upon MC functionalization (UV samples). As seen in Fig. 7.2d and e, the 650 nm absorption peak ((7,5) and (7,6) tubes) does not change significantly with the switch molecule concentration, thus excluding loss of material as a reason.

Figure 7.5 shows emission spectra for the (7,6) tube. Here, the dark samples actually exhibit slightly increased luminescence with increasing SP concentration.

In contrast, in the case of the UV samples, a huge influence of the MC concentration on the spectra can be observed. Again the intensity decreases, albeit not as significantly as it did for the (7,5) tube.
From the PLE maps, chiral compositions of the samples can be extracted, of course only taking into account semi conducting tubes - as in metallic tubes, luminescence is quenched. Figure 7.7 shows the sample compositions for the pure sample (0 $\mu$Mol/L), as well as SP/MC concentrations of 50, 100 and 150 $\mu$Mol/L. As expected, between the pure sample and the different dark samples, the chiral composition hardly changes. The strongest change can be seen in the relative abundance of the (9,4) and (7,6) tubes. The compositions of the UV samples on the other hand change much more drastically. The (8,6) and (10,3) chiralities for example show much larger contributions in the **uv150** compared to the pure sample, while the (6,5) chirality abundance goes down. Marked in the histograms are three laola families (tube with equal 2n+m value) to illustrate that tubes within one laola family are affected differently. In the 2n+m=22 family for example, the (9,4) and (8,6) tubes contributions increase while the (10,2) tube is almost not affected at all.
Apart from the reduced intensity, Figs. 7.4 and 7.5 also reveal a red shift in the transition energies, marked by red arrows. This shift is visualized in Fig. 7.8a and b for fixed excitation and emission, respectively, of the (7,5) tube. As can be seen, even the dark samples show a slight red shift (about 1.5 meV for $E_{11}$ and 2 meV for $E_{22}$ in the case of the **dark150** sample). In the case of the UV samples, however, the transition energies are affected much stronger, leading to shifts of about 5 meV for $E_{11}$ and 8 meV for $E_{22}$ in the case of the **uv150** sample. Similarly, Fig. 7.9 illustrates the change in the transition energies for the (7,6) tube. Again, in the case of the UV samples, a comparatively large shift is found for the case of 150 $\mu$Mol/L SP (9 meV and 13 meV for the $E_{11}$ and $E_{22}$, respectively). The dark samples, again, only exhibit a small red shift by about 2 meV.
What is very interesting is that apart from 7.4a, the changes in the transition energy do not seem to be going into saturation, so in principle even higher SP/MC concentrations could be achieved and should be investigated in the future. The overall shifts in the range of $\approx$10 meV are in good agreement with theoretical calculations by [22, 26] who predicted absorption shifts of up to 30 meV in the case

of optimally aligned dipoles located at the van-der-Waals distance to a (10,10) nanotube.

The pseudo PLE map (Fig. 7.10) shows the transition energies for the dark (left) and UV samples (right). As already seen for the case of the (7,5) and (7,6) tubes, hardly any peak shifts can be observed for the dark samples, while the UV samples exhibit diverse shifts for different nanotube chiralities as illustrated by the bent arrows.

## 7.4. Summary

In this chapter, the adsorption of spiropyran onto suspended carbon nanotubes was achieved using micelle swelling. Absorption measurements confirmed the presence of the switch molecules, as well as carbon nanotubes inside the samples, however, after functionalization the compounds were unable to undergo further isomerization. Using irradiation in the preparation process, merocyanine functionalized samples were produced. PLE experiments were conducted to compare SP and MC functionalized nanotubes. It was found that, SP functionalization only yields little change in the PLE signal of carbon nanotubes, while MC functionalization strongly altered the luminescence, depending on the MC concentration. Observed peak shifts of up to ≈13meV were in good agreement with theoretical calculations. MC functionalization was found to reduce the average luminescence per tube. This might be caused by the planar, de-localized $\pi$ orbital of MC interacting with the nanotubes, thus quenching luminescence. It would also explain the 450 nm absorption band associated with stacked MC. SP functionalization lead to an enhancement. This might be due to improved individualization through the SP molecules inside the micelles. As SP consists of two perpendicular parts, it is not expected to adsorb as strongly as MC. However, even the SP functionalized samples exhibit a strong MC band at 550 nm. The characteristic absorption feature of stacked MC is not present in the SP functionalized samples. To understand this, further investigations are necessary.

# Conclusion

In this work, we investigated switch functionalization of carbon nanotubes. Using different molecular designs, we determined optimal parameters for building up molecular switch compounds able to efficiently disperse and individualize carbon nanotubes in water. Investigating alkyl chains of different lengths as anchor groups. It was found that, while the longest $C_{22}$ chains resulted in the strongest nanotube luminescence, as well as highest tube abundance, a combination of a $C_{16}$ alkyl chain and G2 polyglycerol dendrons led to remarkably higher average luminescence per tube (i.e. high ratio of individualized tubes to nanotube bundles within the samples). However, comparing different water soluble dendron generations, it was found that the medium G2 dendron was much more effective in dispersing individualized CNTs than the smaller G1 or the larger G3 dendron. It was further found that, the influence of the linker between chain and dendron must not be underestimated. Exchanging the linker group was shown to strongly influence the chiral composition of the samples, as well as the solvatochromic shifts of the nanotube transition energies (i.e. interaction strength). Using these results allows for designing highly efficient nanotube surfactants for future applications.

A similarly derived azobenzene compound, consisting of a $C_{11}$ alkyl chain and G3 dendrons was used to achieve reversible precipitation of carbon nanotubes in water. The $C_{11}$-azo-G2 structure was chosen for its high photo stationary state with up to 70% conversion rate. It was shown that the alkAZO compound was very efficient at dispersing individualized CNTs, as confirmed by PLE measurements. Over several switching cycles, consisting of UV irradiation, followed by visible irradiation and sonication, we were able to reversibly induce the formation of nanotube bundles. This was measured by monitoring the sample absorption and led to a red shift of the absorption bands in the order of a few meV. These results open prospects of further research. Carbon nanotubes functionalized with alkAZO could incorporated optical sensors, detecting light of a certain wavelength through bundle formation. Further, light induced spatial selective deposition of carbon nanotubes could be achieved using theses compounds. With patterned irradiation of a surface would lead to nanotube precipitation only at illuminated areas, while dark areas of the substrate are unaffected.

Pyrene-spiropyran derivatives with different spacer lengths were used to non covalently disperse CNTs in THF while retaining the tubes' pristine 1D properties, proven by PLE measurements. As both compounds consisted of the same anchor groups, similar chiral depositions were observed. However, the different tube-switch distances in both compounds was found to induce a red shift in the range of up to 14 meV in the $E_{22}$ transitions between the two samples. even in the SP form. The MC absorption bands was found to be sensitive to the presence of both the pyrene and the nanotubes. While closer proximity to the pyrene anchor leads to a considerable red shift, this effect was found to be partially reversed after tube functionalization. Further, at close distances, the MC form was found to be stabilized in agreement with similar reports on MC adsorbed on gold (111) [84]. However, as the switch is sensitive to light irradiation, PLE measurements investigating the influence of the switch state on the optical properties could not be conducted. The influence of the switch state on the electronic properties could be investigated using transport measurements, similar to the works of other groups [18, 31]. As the tubes are functionalized in solution, they can be readily drop cast onto a given substrate, contacted and measured. Compared to other examples in literature, this is a very convenient way, as it involves only one deposition step for both, switch and nanotube, without the risk of washing away the tubes when trying to functionalize them.

To confirm the different influence of SP and MC on the nanotubes as theoretically predicted, nanotubes were solubilized in water using SDS. SP/MC was then adsorbed onto the tube surface, using the micelle swelling technique. In good agreement with theory [22], peak shifts of up to 13 meV between SP and MC functionalized samples were found. This shift was shown to depend on the number of switches inserted into the micelles and is, thus, tunable in a continuous fashion. Further, the average luminescence per tube in the MC functionalized samples was significantly quenched, while in the SP functionalized it actually increased. A possible explanation for this is the planar geometry of the MC molecule giving rise to a large de-localized $\pi$ orbital able to interact with the nanotube $\pi$ orbitals. Upon adsorption SP and MC molecules are unable to undergo isomerization. However, the characteristic MC absorption bands can be observed even in the SP samples, while the MC compounds exhibit an additional peak attributed to stacked MC (either MC-MC or MC-tube stacked). To understand the exact behavior of both, SP and MC after infiltrating the micelles, further research is needed.

In this thesis, we were able to functionalize CNTs with different optical molecular switches. It was demonstrated, that the nanotubes' optoelectronic properties are influenced by distance between the tube and the switching moiety, as well as the switching state. It was shown that the magnitude of the shift of the nanotubes' electronic transitions depends on the MC coverage. Thus, non covalently attached switches could in principle be used to continuously shift nanotube luminescence, depending on the irradiation time. However, this effect cannot be investigated using PLE, due to the induced back isomerization. A possible way of circumventing this issue would be using molecular switches that either require different energies to induce the back isomerization of cannot optically be switched back at all.

# Bibliography

[1] S. Iijima, "Helical microtubules of graphitic carbon," *Nature*, vol. 354, no. 6348, pp. 56–58, 1991.

[2] S. Reich, C. Thomsen, and J. Maultzsch, *Carbon Nanotubes - Basic Concepts and Physical Properties.* Wiley-VCH, 2004.

[3] R. Saito, G. Dresselhaus, and M. S. Dresselhaus, *Physical Properties of Carbon Nanotubes.* World Scientific Publishing Company, 1998.

[4] A. Jorio, G. Dresselhaus, and M. Dresselhaus, *Carbon Nanotubes.* Axel Springer Verlag, 2008.

[5] A. Hirsch and O. Vostrowsky, "Functionalization of carbon nanotubes," *Functional Molecular Nanostructures*, vol. 245, pp. 193–237, 2005.

[6] K. Balasubramanian, M. Burghard, K. Kern, M. Scolari, and A. Mews, "Photocurrent imaging of charge transport barriers in carbon nanotube devices," *Nano Letters*, vol. 5, no. 3, pp. 507–510, 2005.

[7] C. Gao, Z. Guo, J.-H. Liu, and X.-J. Huang, "The new age of carbon nanotubes: An updated review of functionalized carbon nanotubes in electrochemical sensors," *Nanoscale*, vol. 4, pp. 1948–1963, 2012.

[8] X. Wang, Q. Li, J. Xie, Z. Jin, J. Wang, Y. Li, K. Jiang, and S. Fan, "Fabrication of ultralong and electrically uniform single-walled carbon nanotubes on clean substrates," *Nano Letters*, vol. 9, no. 9, pp. 3137–3141, 2009. PMID: 19650638.

[9] J. D. W. Madden, "Materials science: Stiffer than steel," *Science*, vol. 323, no. 5921, pp. 1571–1572, 2009.

[10] O. Breuer and U. Sundararaj, “Big returns from small fibers: A review of polymer/carbon nanotube composites,” *Polymer Composites*, vol. 25, no. 6, pp. 630–645, 2004.

[11] V. Datsyuk, M. Lisunova, M. Kasimir, S. Trotsenko, K. Gharagozloo-Hubmann, I. Firkowska, and S. Reich, “Thermal transport of oil and polymer composites filled with carbon nanotubes,” *Applied Physics A: Materials Science & Processing*, vol. 105, no. 4, pp. 781–788, 2011.

[12] V. Datsyuk, S. Trotsenko, and S. Reich, “Carbon-nanotube-polymer nanofibers with high thermal conductivity,” *Carbon*, vol. 52, pp. 605–608, 2013.

[13] S. M. Bachilo, M. S. Strano, C. Kittrell, R. H. Hauge, R. E. Smalley, and R. B. Weisman, “Structure-assigned optical spectra of single-walled carbon nanotubes,” *Science*, vol. 298, no. 5602, pp. 2361–2366, 2002.

[14] J. Chen, V. Perebeinos, M. Freitag, J. Tsang, Q. Fu, J. Liu, and P. Avouris, “Bright infrared emission from electrically induced excitons in carbon nanotubes,” *Science*, vol. 310, no. 5751, pp. 1171–1174, 2005.

[15] R. J. Chen, S. Bangsaruntip, K. A. Drouvalakis, N. W. S. Kam, M. Shim, Y. M. Li, W. Kim, P. J. Utz, and H. J. Dai, “Noncovalent functionalization of carbon nanotubes for highly specific electronic biosensors,” *Proceedings Of The National Academy Of Sciences Of The United States Of America*, vol. 100, pp. 4984–4989, Apr. 2003.

[16] T. Someya, J. Small, P. Kim, C. Nuckolls, and J. Yardley, “Alcohol vapor sensors based on single-walled carbon nanotube field effect transistors,” *Nano Letters*, vol. 3, no. 7, pp. 877–881, 2003.

[17] Y. Atassi, J. Chauvin, J. A. Delaire, J. F. Delouis, I. Fanton-Maltey, and K. Nakatani, “Photoinduced manipulations of photochromes in polymers: Anisotropy, modulation of the nlo properties and creation of surface gratings,” *Pure And Applied Chemistry*, vol. 70, no. 11, pp. 2157–2166, 1998.

[18] X. F. Guo, L. M. Huang, S. O’Brien, P. Kim, and C. Nuckolls, “Directing and sensing changes in molecular conformation on individual carbon nanotube

field effect transistors," *J. Am. Chem. Soc.*, vol. 127, no. 43, pp. 15045–15047, 2005.

[19] R. Khairutdinov, M. Itkis, and R. Haddon, "Light modulation of electronic transitions in semiconducting single wall carbon nanotubes," *Nano Letters*, vol. 4, no. 8, pp. 1529–1533, 2004.

[20] E. Del Canto, K. Flavin, M. Natali, T. Perova, and S. Giordani, "Functionalization of single-walled carbon nanotubes with optically switchable spiropyrans," *Carbon*, vol. 48, no. 10, pp. 2815–2824, 2010.

[21] J. W. Mintmire and C. T. White, "Universal density of states for carbon nanotubes," *Phys. Rev. Lett.*, vol. 81, no. 12, pp. 2506–2509, 1998.

[22] E. Malic, M. Hirtschulz, J. Maultzsch, S. Reich, and A. Knorr, "Environmental influence on linear optical spectra and relaxation dynamics in carbon nanotubes," *Phys. Status Solidi B*, vol. 246, pp. 2592–2597, Decembe 2009.

[23] M. S. Dresselhaus, G. Dresselhaus, R. Saito, and A. Jorio, "Exciton photophysics of carbon nanotubes," *Annu. Rev. Phys. Chem.*, vol. 58, pp. 719–747, 2007.

[24] Y. Miyauchi, R. Saito, K. Sato, Y. Ohno, S. Iwasaki, T. Mizutani, J. Jiang, and S. Maruyama, "Dependence of exciton transition energy of single-walled carbon nanotubes on surrounding dielectric materials," *Chem. Phys. Lett.*, vol. 442, no. 4-6, pp. 394–399, 2007.

[25] E. Malic, C. Weber, M. Richter, V. Atalla, T. Klamroth, P. Saalfrank, S. Reich, and A. Knorr, "Microscopic model of the optical absorption of carbon nanotubes functionalized with molecular spiropyran photoswitches," *Phys. Rev. Lett.*, vol. 106, MAR 1 2011.

[26] E. Malic, A. Setaro, P. Bluemmel, C. F. Sanz-Navarro, P. Ordejon, S. Reich, and A. Knorr, "Carbon nanotubes as substrates for molecular spiropyran-based switches," *J. Phys: Condens. Matter*, vol. 24, no. 39, p. 394006, 2012.

[27] S. Banerjee, T. Hemraj-Benny, and S. S. Wong, "Covalent surface chemistry of single-walled carbon nanotubes," *Advanced Materials*, vol. 17, no. 1, pp. 17–29, 2005.

[28] M. J. O'Connell, S. M. Bachilo, C. B. Huffman, V. C. Moore, M. S. Strano, E. H. Haroz, K. L. Rialon, P. J. Boul, W. H. Noon, C. Kittrell, J. P. Ma, R. H. Hauge, R. B. Weisman, and R. E. Smalley, "Band gap fluorescence from individual single-walled carbon nanotubes," *Science*, vol. 297, no. 5581, pp. 593–596, 2002.

[29] Y. Feng, X. Zhang, X. Ding, and W. Feng, "A light-driven reversible conductance switch based on a few-walled carbon nanotube/azobenzene hybrid linked by a flexible spacer," *Carbon*, vol. 48, no. 11, pp. 3091–3096, 2010.

[30] P. Imin, M. Imit, and A. Adronov, "Supramolecular Functionalization of Single-Walled Carbon Nanotubes (SWNTs) with a Photoisomerizable Conjugated Polymer," *Macromolecules*, vol. 45, no. 12, pp. 5045–5050, 2012.

[31] X. J. Zhou, T. Zifer, B. M. Wong, K. L. Krafcik, F. Leonard, and A. L. Vance, "Color detection using chromophore-nanotube hybrid devices," *Nano Letters*, vol. 9, no. 3, pp. 1028–1033, 2009.

[32] F. Ernst, T. Heek, A. Setaro, R. Haag, and S. Reich, "Energy Transfer in Nanotube-Perylene Complexes," *Adv. Funct. Materials*, vol. 22, no. 18, pp. 3921–3926, 2012.

[33] F. Ernst, T. Heek, A. Setaro, R. Haag, and S. Reich, "Functional Surfactants for Carbon Nanotubes: Effects of Design," *J. Phys. Chem. C*, vol. 117, no. 2, pp. 1157–1162, 2013.

[34] T. Y. Astakhova, G. A. Vinogradov, O. D. Gurin, and M. Menon, "Effect of local strain on the reactivity of carbon nanotubes," *Russian Chemical Bulletin*, vol. 51, no. 5, pp. 764–769, 2002.

[35] S. Niyogi, M. Hamon, H. Hu, B. Zhao, P. Bhowmik, R. Sen, M. Itkis, and R. Haddon, "Chemistry of single-walled carbon nanotubes," *Acc. Chem. Res.*, vol. 35, no. 12, pp. 1105–1113, 2002.

[36] A. G. Rinzler, J. Liu, H. Dai, P. Nikolaev, C. B. Huffman, F. J. Rodriguez-Macias, P. J. Boul, A. H. Lu, D. Heymann, D. T. Colbert, R. S. Lee, J. E. Fischer, A. M. Rao, P. C. Eklund, and R. E. Smalley, "Large-scale purification of single-wall carbon nanotubes: process, product, and characterization," *Applied Physics A*, vol. 67, no. 1, pp. 29–37, 1998.

[37] E. T. Mickelson, C. B. Huffman, A. G. Rinzler, R. E. Smalley, R. H. Hauge, and J. L. Margrave, "Fluorination of single-wall carbon nanotubes," *Chem. Phys. Lett.*, vol. 296, no. 1-2, pp. 188 – 194, 1998.

[38] M. Holzinger, A. Hirsch, P. Bernier, G. Duesberg, and M. Burghard, "A new purification method for single-wall carbon nanotubes (SWNTs)," *Applied Physics A*, vol. 70, no. 5, pp. 599–602, 2000.

[39] M. Holzinger, O. Vostrowsky, A. Hirsch, F. Hennrich, M. Kappes, R. Weiss, and F. Jellen, "Sidewall functionalization of carbon nanotubes," *Angew. Chem. Int. Ed.*, vol. 40, no. 21, pp. 4002–+, 2001.

[40] C. Richard, F. Balavoine, P. Schultz, T. W. Ebbesen, and C. Mioskowski, "Supramolecular self-assembly of lipid derivatives on carbon nanotubes," *Science*, vol. 300, no. 5620, pp. 775–778, 2003.

[41] A. Setaro, C. S. Popeney, B. Trappmann, V. Datsyuk, R. Haag, and S. Reich, "Polyglycerol-derived amphiphiles for single walled carbon nanotube suspension," *Chem. Phys. Lett.*, vol. 493, no. 1-3, pp. 147–150, 2010.

[42] C. S. Popeney, A. Setaro, R.-C. Mutihac, P. Bluemmel, B. Trappmann, J. Vonneman, S. Reich, and R. Haag, "Polyglycerol-Derived Amphiphiles for the Solubilization of Single-Walled Carbon Nanotubes in Water: A Structure-Property Study," *ChemPhysChem*, vol. 13, no. 1, pp. 203–211, 2012.

[43] P. Bluemmel, A. Setaro, C. S. Popeney, B. Trappmann, R. Haag, and S. Reich, "Amphiphile replacement on carbon nanotube surfaces: Effect of aromatic groups on the interaction strength," *Phys. Status Solidi B*, vol. 248, no. 11, pp. 2532–2535, 2011.

[44] A. Setaro, C. S. Popeney, B. Trappmann, R. Haag, and S. Reich, "Interaction between single-walled carbon nanotubes and alkyl-polyglycerol derivatives," *Phys. Status Solidi B*, vol. 247, no. 11-12, pp. 2758–2761, 2010.

[45] R. J. Chen, Y. G. Zhang, D. W. Wang, and H. J. Dai, "Noncovalent sidewall functionalization of single-walled carbon nanotubes for protein immobilization," *J. Am. Chem. Soc.*, vol. 123, no. 16, pp. 3838–3839, 2001.

[46] N. Nakashima, Y. Tomonari, and H. Murakami, "Water-soluble single-walled carbon nanotubes via noncovalent sidewall-functionalization with a pyrene-carrying ammonium ion," *Chemistry Letters*, vol. 31, no. 6, pp. 638–639, 2002.

[47] C. H. Xue, R. J. Zhou, M. M. Shi, Y. Gao, G. Wu, X. B. Zhang, H. Z. Chen, and M. Wang, "The preparation of highly water-soluble multi-walled carbon nanotubes by irreversible noncovalent functionalization with a pyrene-carrying polymer," *Nanotechnology*, vol. 19, no. 21, p. 215604, 2008.

[48] T. Simmons, J. Bult, D. Hashim, R. Linhardt, and P. Ajayan, "Noncovalent functionalization as an alternative to oxidative acid treatment of single wall carbon nanotubes with applications for polymer composites," *ACS Nano*, 2009.

[49] C. Backes, C. D. Schmidt, F. Hauke, C. Bottcher, and A. Hirsch, "High population of individualized swcnts through the adsorption of water-soluble perylenes," *J. Am. Chem. Soc.*, vol. 131, no. 6, pp. 2172–2184, 2009.

[50] D. S. Hecht, R. J. A. Ramirez, M. Briman, E. Artukovic, K. S. Chichak, J. F. Stoddart, and G. Gruner, "Bioinspired detection of light using a porphyrin-sensitized single-wall nanotube field effect transistor," *Nano Letters*, vol. 6, no. 9, pp. 2031–2036, 2006.

[51] R. Marquis, C. Greco, I. Sadokierska, S. Lebedkin, M. M. Kappes, T. Michel, L. Alvarez, J. L. Sauvajol, S. Meunier, and C. Mioskowski, "Supramolecular discrimination of carbon nanotubes according to their helicity," *Nano Letters*, vol. 8, no. 7, pp. 1830–1835, 2008.

[52] D. Tasis, N. Tagmatarchis, A. Bianco, and M. Prato, “Chemistry of carbon nanotubes,” *Chemical Reviews*, vol. 106, no. 3, pp. 1105–1136, 2006.

[53] M. O’Connell, P. Boul, L. Ericson, C. Huffman, Y. Wang, E. Haroz, C. Kuper, J. Tour, K. Ausman, and R. Smalley, “Reversible water-solubilization of single-walled carbon nanotubes by polymer wrapping,” *Chemical Physics Letters*, vol. 342, no. 3-4, pp. 265–271, 2001.

[54] J. Sung, H. Kim, H. Jin, H. Choi, and I. Chin, “Nanofibrous membranes prepared by multiwalled carbon nanotube/poly(methyl methacrylate) composites,” *Macromolecules*, vol. 37, no. 26, pp. 9899–9902, 2004.

[55] M. Zheng, A. Jagota, E. Semke, B. Diner, R. Mclean, S. Lustig, R. Richardson, and N. Tassi, “DNA-assisted dispersion and separation of carbon nanotubes,” *Nature Materials*, vol. 2, no. 5, pp. 338–342, 2003.

[56] M. Zheng and E. D. Semke, “Enrichment of single chirality carbon nanotubes,” *Journal of the American Chem*, vol. 129, no. 19, pp. 6084+, 2007.

[57] B. Smith, M. Monthioux, and D. Luzzi, “Encapsulated c60 in carbon nanotubes,” *Nature*, vol. 396, no. 6709, pp. 323–324, 1998.

[58] O. Vostrowsky and A. Hirsch, “Molecular peapods as supramolecular carbon allotropes,” *Angew. Chem. Int. Ed.*, vol. 43, no. 18, pp. 2326–2329, 2004.

[59] P. Suppan, “Solvatochromic shifts - the influence of the medium on the energy of electronic states,” *Journal of Photochemistry and Photobiology, A: Chemistry*, vol. 50, no. 3, pp. 293–330, 1990.

[60] J. H. Choi and M. S. Strano, “Solvatochromism in single-walled carbon nanotubes,” *Applied Physics Letters*, vol. 90, no. 22, 2007.

[61] Brochure, *Why Limit Yourself? - LAMBDA UV/Vis and UV/Vis/NIR Spectrophotometers.* PerkinElmer, 2007.

[62] Manual, *Technical Specifications for the LAMBDA 1050 UV/Vis/NIR and LAMBDA 950 UV/Vis/NIR Spectrophotometers.* PerkinElmer, 2007.

[63] P. Specifications, *Thermo Scientific Evolution Array.* Termo Fisher Scientific Inc. All right, 2010.

[64] O. Manual, *Fluorolog-3 Spectrofluometer - Part number 81014.* Horiba Jobin Yvon, 3.1 ed., March 2006.

[65] S. Y. Ju, J. Doll, I. Sharma, and F. Papadimitrakopoulos, "Selection of carbon nanotubes with specific chiralities using helical assemblies of flavin mononucleotide," *Nature Nanotechnology*, vol. 3, no. 6, pp. 356–362, 2008.

[66] B. Trappmann, K. Ludwig, M. R. Radowski, A. Shukla, A. Mohr, H. Rehage, C. Boettcher, and R. Haag, "A New Family of Nonionic Dendritic Amphiphiles Displaying Unexpected Packing Parameters in Micellar Assemblies," *J. Am. Chem. Soc.*, vol. 132, no. 32, pp. 11119–11124, 2010.

[67] P. Bluemmel, "Solubilization and individualization of carbon nanotubes by noncovalent functionalization with switchable molecules pascal," Master's thesis, Freie Universität Berlin, 2010.

[68] P. Bluemmel, A. Setaro, C. S. Popeney, R. Haag, and S. Reich, "Dispersion of carbon nanotubes using an azobenzene derivative," *Physica Status Solidi B: Basic Solid State Physics*, vol. 247, no. 11-12, pp. 2891–2894, 2010.

[69] C. Koerdel, A. Setaro, P. Bluemmel, C. S. Popeney, S. Reich, and R. Haag, "Controlled reversible debundling of single-walled carbon nanotubes by photo-switchable dendritic surfactants," *Nanoscale*, vol. 4, no. 10, pp. 3029–3031, 2012.

[70] T. Nägele, R. Hoche, W. Zinth, and J. Wachtveitl, "Femtosecond photoisomerization of cis-azobenzene," *Chem. Phys. Lett.*, vol. 272, no. 5-6, pp. 489 – 495, 1997.

[71] H. Rau, *Photochromism. Molecules and Systems - Chapter 4, Azo Compounds.* Elsevier Sci Ltd, 2003.

[72] C. M. Stuart, R. R. Frontiera, and R. A. Mathies, "Excited-state structure and dynamics of cis- and trans-azobenzene from resonance raman intensity analysis," *J. Phys. Chem. A*, vol. 111, no. 48, pp. 12072–12080, 2007.

[73] M. M. J. Tecklenburg, D. J. Kosnak, A. Bhatnagar, and D. K. Mohanty, "Vibrational characterization of azobenzenes, azoxybenzenes and azoaromatic and azoxyaromatic polyethers," *Journal Of Raman Spectroscopy*, vol. 28, no. 10, pp. 755–763, 1997.

[74] J. M. Simmons, I. In, V. E. Campbell, T. J. Mark, F. Leonard, P. Gopalan, and M. A. Eriksson, "Optically modulated conduction in chromophore-functionalized single-wall carbon nanotubes," *Phys. Rev. Lett.*, vol. 98, no. 8, p. 086802, 2007.

[75] A. M. Kolpak and J. C. Grossman, "Azobenzene-Functionalized Carbon Nanotubes As High-Energy Density Solar Thermal Fuels," *Nano Letters*, vol. 11, no. 8, pp. 3156–3162, 2011.

[76] J. Dokic, M. Gothe, J. Wirth, M. V. Peters, J. Schwarz, S. Hecht, and P. Saalfrank, "Quantum Chemical Investigation of Thermal Cis-to-Trans Isomerization of Azobenzene Derivatives: Substituent Effects, Solvent Effects, and Comparison to Experimental Data," *Journal of Physical Chemistry A*, vol. 113, no. 24, pp. 6763–6773, 2009.

[77] C. Koerdel, C. S. Popeney, and R. Haag, "Photoresponsive amphiphiles based on azobenzene-dendritic glycerol conjugates show switchable transport behavior," *Chemical Communications*, vol. 47, no. 23, pp. 6584–6586, 2011.

[78] A. Setaro, P. Bluemmel, C. Maity, S. Hecht, and S. Reich, "Non-Covalent Functionalization of Individual Nanotubes with Spiropyran-Based Molecular Switches," *Adv. Funct. Materials*, vol. 22, no. 11, pp. 2425–2431, 2012.

[79] P. Bluemmel, A. Setaro, C. Maity, S. Hecht, and S. Reich, "Tuning the interaction between carbon nanotubes and dipole switches: the influence of the change of the nanotube-spiropyran distance," *J. Phys: Condens. Matter*, vol. 24, no. 39, p. 394005, 2012.

[80] P. Bluemmel, A. Setaro, C. Maity, S. Hecht, and S. Reich, "Designing a spiropyran-based molecular switch for carbon nanotube functionalization: Influence of anchor groups and tube-switch separation," *Physica Status Solidi B: Basic Solid State Physics*, vol. 249, no. 12, pp. 2479–2482, 2012.

[81] R. Guglielmetti, *Photochromism Molecules and Systems - Chapter 8, 4n+2 Systems: Spiropyrans.* Elsevier Sci Ltd, 2003.

[82] E. Del Canto, M. Natali, D. Movia, and S. Giordani, “Photo-controlled release of zinc metal ions by spiropyran receptors anchored to single-walled carbon nanotubes,” *Phys. Chem. Chem. Phys.*, vol. 14, no. 17, pp. 6034–6043, 2012.

[83] Y. Song, C. Xu, W. Wei, J. Ren, and X. Qu, “Light regulation of peroxidase activity by spiropyran functionalized carbon nanotubes used for label-free colorimetric detection of lysozyme,” *Chemical Communications*, vol. 47, no. 32, pp. 9083–9085, 2011.

[84] C. Bronner, G. Schulze, K. J. Franke, J. I. Pascual, and P. Tegeder, “Switching ability of nitro-spiropyran on Au(111): electronic structure changes as a sensitive probe during a ring-opening reaction,” *Journal of Physics: Condensed Matter*, vol. 23, no. 48, 2011.

[85] R. K. Wang, W.-C. Chen, D. K. Campos, and K. J. Ziegler, “Swelling the Micelle Core Surrounding Single-Walled Carbon Nanotubes with Water-immiscible Organic Solvents,” *Journal of the American Chemical Society*, vol. 130, no. 48, pp. 16330–16337, 2008.

[86] C. Roquelet, J.-S. Lauret, V. Alain-Rizzo, C. Voisin, R. Fleurier, M. Delarue, D. Garrot, A. Loiseau, P. Roussignol, J. A. Delaire, and E. Deleporte, “Pi-Stacking Functionalization of Carbon Nanotubes through Micelle Swelling,” *ChemP*, vol. 11, no. 8, pp. 1667–1672, 2010.

# Acknowledgements

I thank Prof. Dr. Stephanie Reich for the opportunity to write this dissertation, but especially for allowing me to pursue my own ideas, yet still pointing me in the right direction, whenever it was necessary. Stephanie gave me the opportunity to share in the knowledge - among her own - of many colleagues by arranging collaborations and encouraging me to attend various conferences and winter schools during my time in her group.

I thank Dr. Antonio Setaro, who not only taught me how to work as an experimental physicist, but how to analyze, understand and publish the results. Antonio always took the time to give me advice when experiments failed or seemed like a dead end and most importantly, he reintroduced me to Mathematica, which i extensively used to write this thesis.

Thank you to the Rainer Haag and his group (especially Christian Kördel and Chris Popeney) for designing and synthesizing the amphiphiles and azobenzene molecules, as well as for many interesting and enjoyable discussions. And cookies!

I would like to thank the group of Stefan Hecht and especially Chandan Maity for synthesizing the spiropyran derivatives and for many engaging project meetings.

I wish to thank my group, for providing support in scientific questions, for sharing knowledge and helping with stubborn instruments. But also for not only being colleagues. For many engaging conversations over lunch, beer, barbeque or glühwein. For evenings at the movies and breaks at youtube and for lunch on the sun deck.

Lastly I want to thank my Family - my parents, my sister and my girlfriend.

# A

# Appendix A

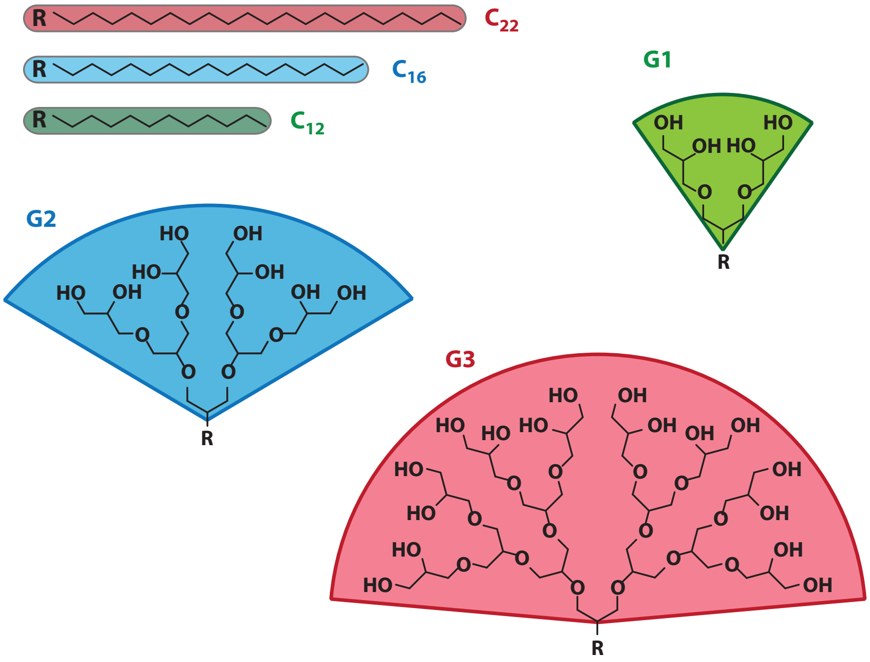

Figure A.1. Detailled structures of the alkyl chains and dendrons used in this work. Alkyl chains differ by chain length (12, 16 and 22 carbon atoms), while dendrons differ in generation. A generation two dendron (G2, blue), therefor, consists of two dendrons of generation one (G1, green), while a generation three dendron (G3, red) is made up of two G2 or four G1 dendrons.

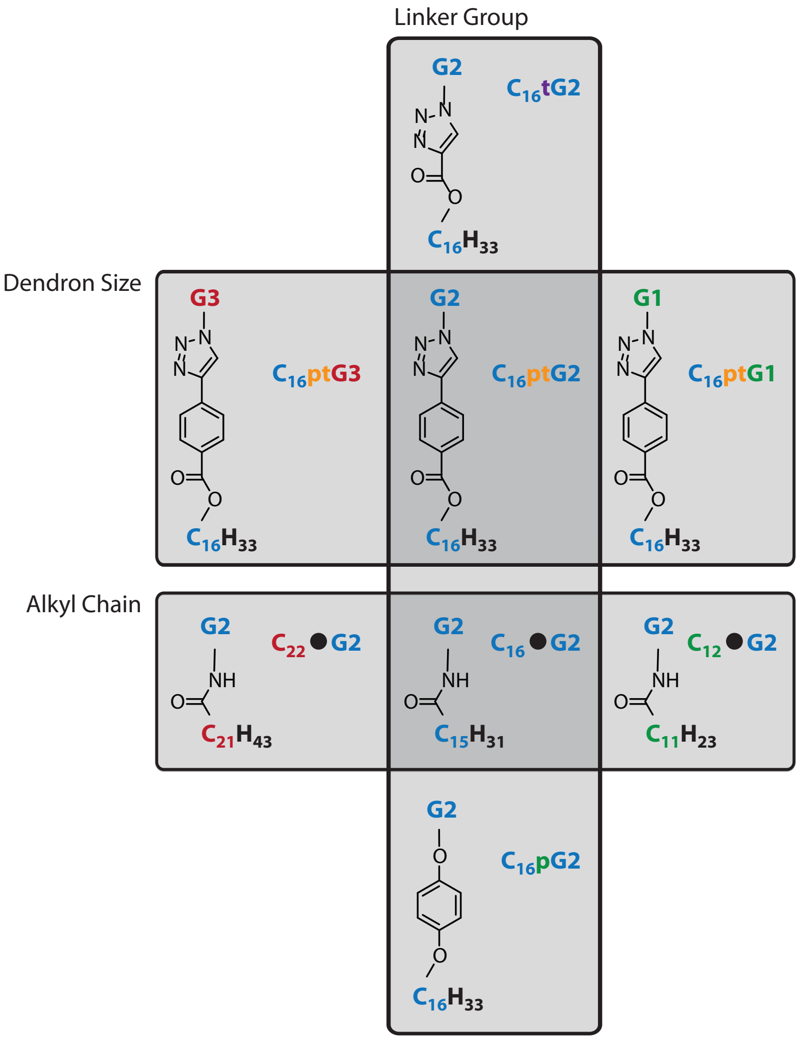

Figure A.2. Detailled structures of the amphiphilic molecules 4. As can be seen, the molecules within the different groups ("Linker Group", "Dendron Size" and "Alkyl Chain" only differ by the titular attribute. The amphiphile in the "Dendron Size" group for example all consist of a $C_{16}$ chain connected to a linker made of a phenyl group and a triazol pentagon connected to dendrons of different generations.

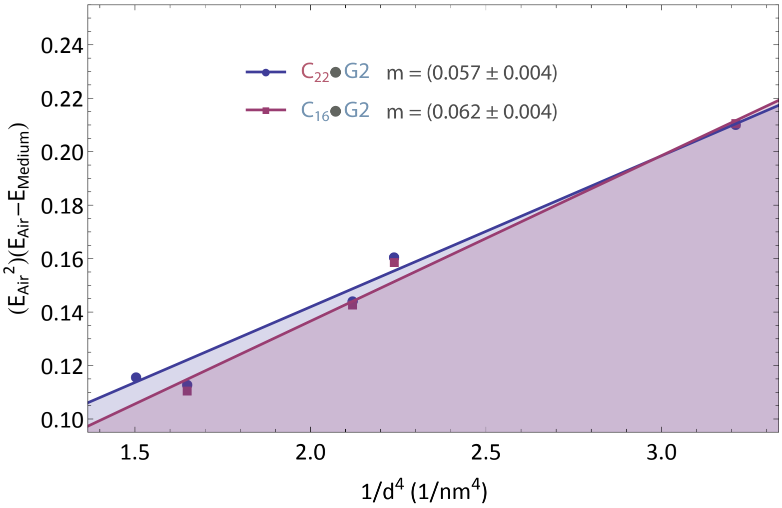

Figure A.3. Solvatochromic shifts of the carbon nanotubes solubilized using $\mathbf{C_{22}}$●**G2** and $\mathbf{C_{16}}$●**G2**, respectively, calculated from the $E_{11}$ energies. Even though the longest chain resulted in strongest luminescence, as well as absorbance, the medium chain sample seems to exhibit stronger interaction with carbon nanotubes. However, it has to be noted that due to the absence of the (9,4)-tube in the $\mathbf{C_{16}}$●**G2** sample, as well as the small overall PLE shifts between the two samples, the actual solvatochromic shift of the $\mathbf{C_{16}}$●**G2** sample is probably found at the lower boundary of the error interval.

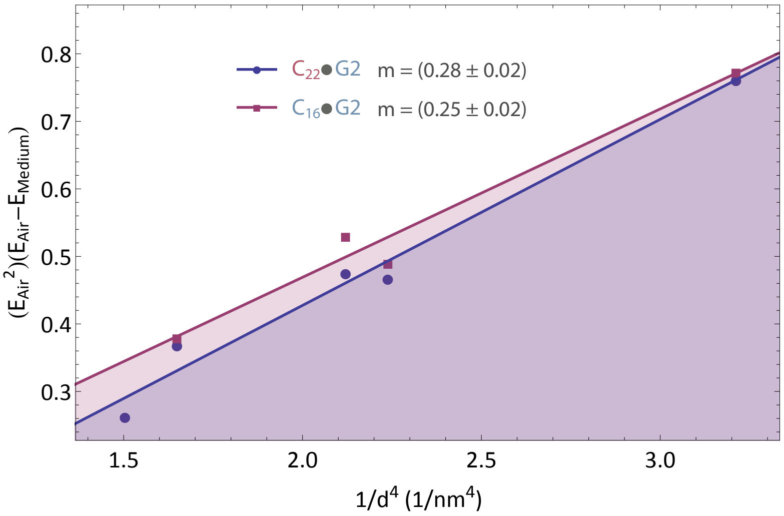

Figure A.4. Solvatochromic shifts of the carbon nanotubes solubilized using **C$_{22}$●G2** and **C$_{16}$●G2**, respectively, calculated from the $E_{22}$ energies. Again **C$_{16}$●G2** exhibits a larger solvatochromic shift that **C$_{22}$●G2**, and again due to the absence of the (9,4)-tube in the **C$_{16}$●G2** sample, the actual value is probably closer to the lower boundary of the error interval, making for a smaller difference. However, although the $E_{22}$ transitions show bigger discrepancies between the two samples, than the $E_{11}$ transistions did.

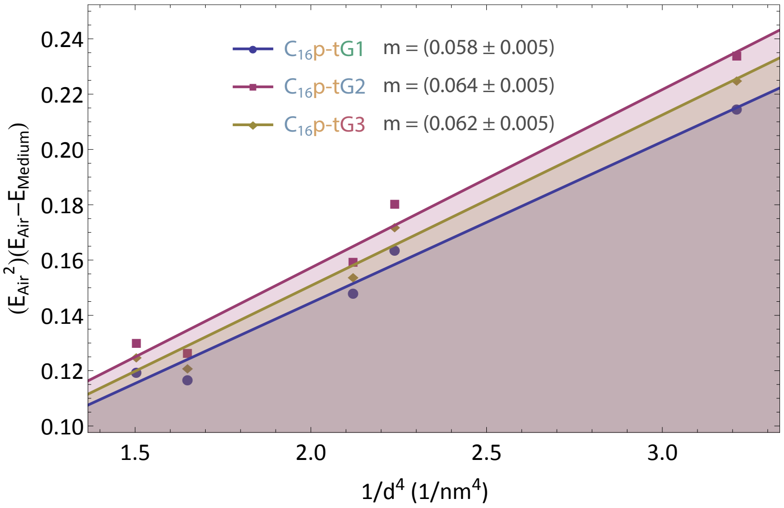

Figure A.5. Solvatochromic shifts of the carbon nanotube samples suspended using molecules with different dendron generations, obtained from $E_{11}$ transitions. The slopes indicate strongest amphiphile-tube interaction for the generation two dendron.

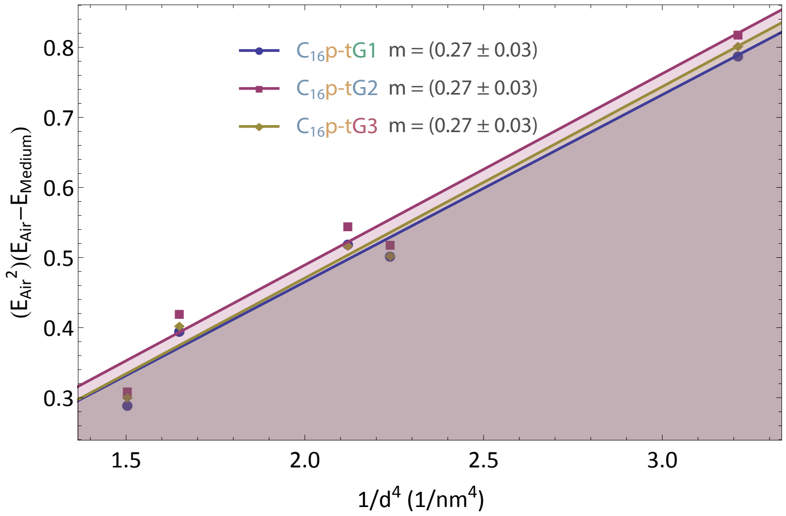

Figure A.6. Solvatochromic shifts of the carbon nanotube samples suspended using molecules with different dendron generations, obtained from $E_{22}$ transitions. In this picture, all slopes are identical, thus, not allowing to draw any conclusions concerning interaction strength.

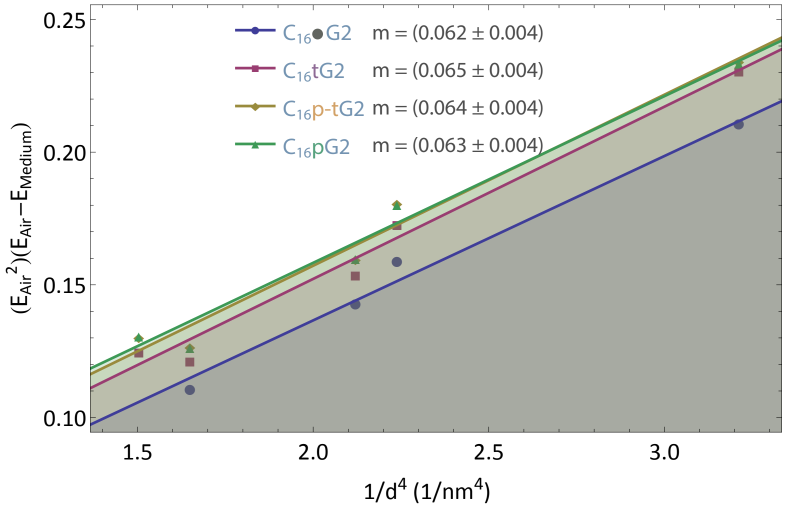

Figure A.7. Solvatochromic shifts obtained from $E_{11}$ energies for samples made with amphiphiles containing different linker moieties. The largest slope is found in the trialzol pentagon sample, followed by the combination of a phenyl ring and a triazol pentagon, a single phenyl ring and finally a simple nitrogen.

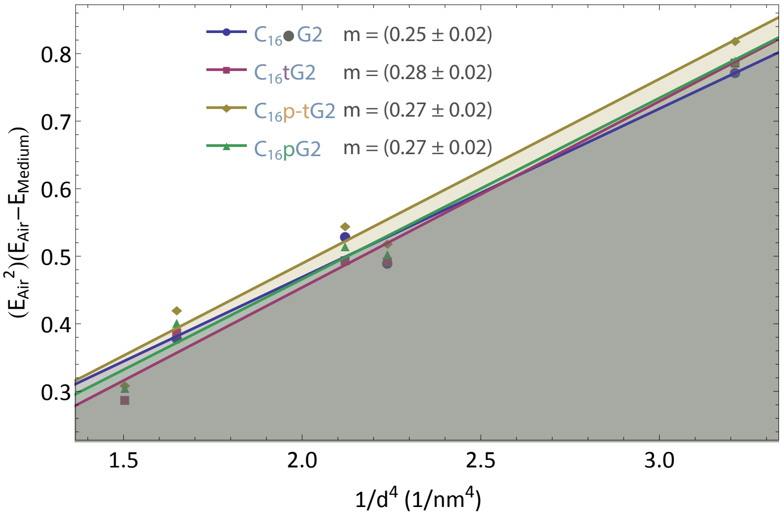

Figure A.8. Solvatochromic shifts obtained from $E_{22}$ energies for samples made with amphiphiles containing different linker moieties. The largest slope is found in the trialzol pentagon sample, followed by the combination of a phenyl ring and a triazol pentagon, as well as the sample with a single phenyl ring and finally a simple nitrogen.